

p-ISSN 1811-1165
e-ISSN 2413-2179

VOLUME 15, No. 1(29), 2018

EURASIAN
PHYSICAL
TECHNICAL

JOURNAL

KARAGANDA STATE UNIVERSITY NAMED AFTER E.A. BUKETOV

KARAGANDA, THE REPUBLIC OF KAZAKHSTAN

EURASIAN PHYSICAL TECHNICAL JOURNAL

Journal Founder:

**KARAGANDA STATE UNIVERSITY
NAMED AFTER E.A. BUKETOV**

**Е.А.БӨКЕТОВ АТЫНДАҒЫ ҚАРАҒАНДЫ
МЕМЛЕКЕТТІК УНИВЕРСИТЕТІ**

**КАРАГАНДИНСКИЙ ГОСУДАРСТВЕННЫЙ
УНИВЕРСИТЕТ ИМ. Е.А.БУКЕТОВА**

Contact information:

Editorial board of EPHTJ (Build. 2, room 221)
Karaganda State University
named after E.A. Buketov
Universitetskaya Str.28, Karaganda,
Kazakhstan, 100028
Subscription index: 75240
Tel: +7(7212)77-04-03
Fax: +7(7212)77-03-84
E-mail: ephtj@mail.ru

Signed to print on **22.06.2018**.
Format 60x84 1/8. Offset paper.
Volume 14.62 p.sh. Circulation 300 copies.
Agreed price. Order No. 78.

Басуға **22.06.2018** ж. қол қойылды.
Пішімі 60×84 1/8. Офсеттік қағазы.
Көлемі 14.62 ес.-б.т. Таралымы 300 дана.
Бағасы келісім бойынша. Тапсырыс № 78.

Подписано к печати **22.06.2018**.
Формат 60 × 84 1/8. Офсетная бумага.
Объем 14.62 печ.л. Тираж 300 экз.
Цена договорная. Заказ № 78.

Printed in the Publishing House
of the KarSU named after academician E.A.Buketov

академик Е.А. Бөкетов атындағы ҚарМУ
баспасының баспаханасында басылып шықты

Отпечатано в Издательстве
КарГУ имени академика Е.А.Букетова

p - ISSN 1811-1165
e - ISSN 2413-2179

Volume 15, No. 1(29), 2018

1st issue – March, 2004

PROJECT MANAGER, RECTOR

Kubeev E.K., Karaganda State University named after E.A.Buketov,
Karaganda, Kazakhstan

Chief EDITOR

Sakipova S.E., Karaganda State University named after E.A.Buketov,
Karaganda, Kazakhstan

EDITORIAL BOARD

Aringazin A.K., Institute for Basic Research, L.N. Gumilev Eurasian
National University, Astana, Kazakhstan

Dueck J., Erlangen-Nuernberg University, Erlangen, Germany

Dzhumanov S., National University of Uzbekistan named after
M. Ulugbek, Tashkent, Uzbekistan

Epik E.Ya., Institute of Engineering Thermophysics, National Sciences
Academy of Ukraine, Kiev, Ukraine

Ibrayev N.Kh., Institute of Molecular Nanophotonics, Karaganda State
University named after E.A.Buketov, Karaganda, Kazakhstan

Jakovics A., Faculty of Physics and Mathematics, University of Latvia,
Riga, Latvia

Kidibaev M.M., Issyk-kul State University named after K.Tynystanov,
Karakol, Kyrgyzstan

Kumekov S.E., Kazakh State National Technical University named
after K.Satbaev, Almaty, Kazakhstan

Kuritnyk I.P., Department of Electronics and Automation,
High school in Oswiecim, Poland

Miau J.J., Department of Aeronautics and Astronautics, National
Cheng Kung University, Tainan, Taiwan

Pedrini C., University Claude Bernard Lyon I, France

Potapov A.A., V.A.Kotelnikov Institute of Radio Engineering and
Electronics of RAS, Moscow, Russia

Pribaturin N.A., Institute of Thermal Physics, SB RAS, Novosibirsk,
Russia

Rahimov F.K., Tajik State National University, Dushanbe, Tajikistan

Sakovich G.V., Institute of Chemical Problems and Power
Technologies, Byisk, Russia

Saulebekov A.O Kazakhstan Branch of Lomonosov Moscow State
University, Astana, Kazakhstan

Shrager E.R., National Research Tomsk State University, Tomsk,
Russia

Stoev M., South-West University «Neofit Rilski», Blagoevgrad,
Bulgaria

Zhanabaev Z.Zh., Al-Farabi Kazakh National State University, Almaty,
Kazakhstan

CONSULTANT OF TRANSLATION

Yakhina S.B., Karaganda State University named after E.A. Buketov,
Karaganda, Kazakhstan

TECHNICAL EDITORS

Akhmerova K.E., Kambarova Zh.T. Karaganda State University
named after E.A.Buketov, Karaganda, Kazakhstan

© Karaganda State University, 2018

© Қарағанды мемлекеттік университеті, 2018

Registered by the Ministry of Culture, Information and Public Adjustment of the Republic of Kazakhstan.
Қазақстан Республикасы мәдениет, ақпарат және қоғамдық келісім министрлігімен тіркелді
Registration Certificate No. 4382-Zh, November 7, 2003.

CONTENTS

| | |
|--|----|
| PREFACE | 4 |
| NONLINEAR PHYSICS. | |
| MODELING OF THE NONLINEAR PHYSICAL AND TECHNICAL PROCESSES. | |
| Zhumaev M.R., Sharipov M.Z., Mirzhonova N.N. | |
| THE AVERAGED LAGRANGIAN OF SOLITONS OF BOSE-EINSTEIN CONDENSATION | 6 |
| Guchenko S.A., Zavatskaya O.N., Yurov V.M., Kasymov S.S., Laurinas V.Ch. | |
| FRACTAL STRUCTURE OF MULTI-ELEMENT COATINGS..... | 10 |
| Baktybekov K.S. | |
| NONLINEAR RADIATION PROCESSES IN SOLIDS..... | 17 |
| Ashurov A. E. | |
| SPACECRAFT DISPOSAL IN QUASI-GEOSTATIONARY ORBIT..... | 22 |
| MATERIAL SCIENCE. TECHNOLOGIES FOR CREATING NEW MATERIALS. | |
| Kupchishin A.I., Tlebaev K.B. | |
| X-RAY STRUCTURAL STUDIES OF POLYETHETRAFLUOROETHYLEN..... | 29 |
| Zhanabaev Z.Zh., Grevtseva T.Yu., Ikramova S.B., Filippov N.V. | |
| ELECTRICAL PROPERTIES OF QUANTUM NANOWIRES. | 34 |
| Agelmenev M.E., Bratukhin S.M., Polikarpov V.V. | |
| THE INFLUENCE OF VARIOUS EFFECTS ON THE ORDERING OF LIQUID CRYSTALS LOCATED ON NANORIBBON GRAPHENE | 40 |
| Guchenko S.A., Zavatskaya O.N., Yurov V.M., Kasymov S.S., Laurinas V.Ch. | |
| SURFACE ENERGY AND THE TOLMAN CONSTANT OF HALOGENIDE OF ALKALI METALS..... | 48 |
| Kambarova ZH.T., Saulebekov A.O. | |
| DEVELOPMENT OF MIRROR ENERGY ANALYZER BASED ON ELECTROSTATIC QUADRUPOLE-CYLINDRICAL FIELD..... | 55 |
| Serikov T.M., Ibrayev N.Kh., Zeinidenov A.K. | |
| PHOTOCATALYTIC PROPERTIES OF TiO ₂ /Ag NANOSTRUCTURES..... | 61 |
| Astanov S.Kh., Kasimova G.K. | |
| THE NATURE OF ELECTRONIC SPECTRA OF SELF-COMBINED RIBOFLAVIN MOLECULES. | 66 |

ENGINEERING, DEVICES AND METHODS OF EXPERIMENT.
Amochaeva G.P., Seisenbaeva G.S., Musina G.I.

SAFETY ON A RAILWAY CROSSING BY MEANS OF SYSTEM OF VIDEO 73

Umirzakov A.G., Mereke A.L., Rakmetov B.A., Beisenov R.E., Muratov D.A.

 OBTAINING OF POROUS NICKEL ANODE BY HOT PRESSING AND ETCHING
 METHODS FOR SOLID-OXIDE FUEL CELL APPLICATION..... 78

ENERGETICS. THERMOPHYSICS. HYDRODYNAMICS.
Komilov O.S., Sharipov M.Z., Tilloev L.I., Majidov J.A.

AUTONOMOUS BIOGAS INSTALLATION WITH SOLAR HEATING SYSTEM..... 82

Issakhanov M.Zh., Sakipova Sh.E., Alibek N.B., Dyusenbaev T.S.

 DEVELOPMENT OF ENERGY-SAVING VENTILATION SYSTEM FOR
 AGRICULTURAL BUILDINGS..... 86

Kazakbay G.B., Turalina D.E.

 INVESTIGATION OF THE MAIN CHARACTERISTICS OF THE STRAIGHT FLOW
 HYDRO TURBINE 92

Ibraev E.K., Ibraeva O.T., Sakipov K.E.

UNBURNED WASTE COAL FLOTATION AGGLOMERATION..... 99

SUMMARIES..... 106
INFORMATION ABOUT AUTHORS..... 113
GUIDELINES FOR AUTHORS..... 115

Dear Authors and Readers!
Honourable colleagues!

We are proudly announce the celebration of the 25th anniversary of our capital Astana - the results of not only the political and economic development of our country, but also achievements in science and education. The life experience and the practice teaches that the exchange of information, the use of new information technologies and the evaluation of the obtained data play a crucial role in achieving significant scientific results. This is promoted by scientific publications and journals. The analysis of statistical data for the past year shows a significant increase in publishing activity of our scientists and physicists in various prestigious periodical scientific publications. In this regard, scientific conferences and training courses would be useful place for the international exchange of information.

This year our University conducts 2 conferences on the physical and technical directions.

1. On August 1-4, 2018, the E.A. Buketov Karaganda State University along with the Institute of Physical and Technical Problems and Materials Science named after Academician Zh. Zheenbaev of National Academy of Sciences of the Kyrgyz Republic, L.N. Gumilyov Eurasian National University and Physical and Technical Society of Kazakhstan will organize the XIVth International Scientific Conference "Solid State Physics, Functional Materials and New Technologies" (FTT-2018), dedicated to the 80th birthday of Professor T.A. Kuketayev. The scientific program of the conference includes the following sections regarding all areas of the fundamental and applied issues of condensed matter physics:

- 1) The point and extended defects in wide-systems: oxides, nitrides, ceramics, minerals, organic and photonic crystals; intrinsic and impurity luminescence of condensed media;
- 2) The electrical and optical properties, relaxation of media, phase transitions, ordering, surface phenomenon, impurities with shallow and deep levels, structural defects in semiconductors;
- 3) The phase and structural transformations in metals and alloys, a modification of physical and mechanical properties of metals and alloys;
- 4) Functional materials, nanotechnologies and nanomaterials;
- 5) High technology.

We hope that all interested scientists will be able to discuss vital topics of modern solid-state physics at the conference.

2. On 27-28 September, 2018 E.A. Buketov Karaganda State University invites all interested persons to participate in the Republican scientific and practical conference "Actual problems of heat power engineering and applied thermo-physics" dedicated to the 80th birthday of professor Zh.S. Akylbaev. During the conference the following sections are planned:

- 1) Professor Akylbaev Zhambyl Saulebekovich - scientist, teacher, public persona.
- 2) Innovative pedagogical technologies for the training of highly qualified specialists.
- 3) Modern physics issues/questions.
- 4) Discussion of applied thermophysics, heat power engineering and industrial ecology.

Professor Zh.S. Akylbaev for many years leded our University. He dedicatedly contributed to the development of new scientific and educational fields and specialties. With his personal involvement and under his direction, the Technical Thermophysics Department was established in 1980 and later named after Zh.S. Akylbayev.

Professor Zh.S. Akylbaev was one of the founders of our scientific publishing Eurasian Physics and Technology Journal which is developing since 2004.

3. In addition to above mentioned conferences the following important for the physical and technical community of scientists and young researchers event will be held in Moscow.

Department of Chemistry and Material Sciences of RAS, Institution of Russian Academy of Sciences A.A. Baikov Institute of Metallurgy and Material Sciences RAS, Council of Young Scientists of RAS invite you to take part in XIVth Russian annual conference for young scientists and post-graduate students "Physical Chemistry and Technology of Inorganic Materials". The conference is targeting young scientists and post-graduate students of academic institutes, state scientific centers and universities, enterprises interacting with metallurgy and material sciences, and senior students.

The conference will be held 16-19 October, 2018 in the Institution of Russian Academy of Sciences A.A. Baikov, the Institute of Metallurgy and Materials Sciences RAS in Moscow.

The conference aim is to support the creative activity of young scientists and post-graduate students of academic institutes, state scientific centers and universities. This conference will review and analyze the complex of problems on metallurgy and materials sciences including nanomaterials and nanotechnologies, advanced materials, resource-saving processes and technologies.

The Eurasian Physical Technical Journal offers to publish scientific articles of those who are interested in reaching out to the international audience.

We are looking forward to see you participating in the announced events and amongst the authors of our future publications.

Respectfully,
Chief Editor, Saule E. Sakipova
Karaganda, June, 2018

UDC 530.182+538.9

THE AVERAGED LAGRANGIAN OF SOLITONS OF BOSE-EINSTEIN CONDENSATION

Zhumaev M.R., Sharipov M.Z., Mirzhonova N.N.

Bukhara Engineering - Technologies Institute, 200100, Bukhara, Uzbekistan, mrjumaev2011@mail.ru

The effect of the fluctuation interaction of atoms forming a condensate on solitons of the Bose-Einstein condensation is considered. A short derivation of the Gross-Pitaevsky equation is given. The averaged Lagrangian of solitons of the Bose-Einstein condensation is determined. The obtained results give an opportunity to investigate the solitons dynamics under the action of various perturbations.

Keywords: Bose-Einstein condensate, Gross-Pitaevskii equation, averaged Lagrangian.

Introduction

Increased interest in studies of Bose - Einstein condensation is due to the fact that this phenomenon plays an important role in physical systems consisting of strongly interacting nanoparticles [1-2]. Probably, it also causes high-temperature superconductivity.

In this paper, a great deal of attention is paid to studying the influence of the fluctuation interaction of atoms forming the condensate. We present the short derivation of the Gross - Pitaevskii equation and find the averaged Lagrangian of solitons in the Bose - Einstein condensate.

1. Short derivation of the Gross - Pitaevskii equation

As is known, the quantum state of Bose - Einstein condensate atoms is described by one common wave function because all of them have the minimum possible energy. Therefore, in accordance with quantum mechanics, this wave function is described by the Schrodinger equation:

$$i\eta \frac{\partial \psi}{\partial t} = (\hat{T} + u(r,t) + V_{int})\psi \quad (1)$$

Here: $\psi(r,t)$ is the wave function of the system of particles under consideration, \hat{T} is the kinetic-energy operator, $u(r,t)$ is the external-field potential, and V_{int} is the interaction potential of atoms forming the condensate.

If one restricts oneself to the case where the external-field potential is isotropic and spherically symmetric (which is used in experiments for studying Bose - Einstein condensation to create the trap potential), it can be written in the form of the following spherical harmonic (or so-called parabolic) potential:

$$u(r) = \frac{k}{2} r^2 \quad (2)$$

where k is the force constant of the harmonic potential (or the effective elasticity coefficient).

In this case, it is convenient to use the spherical coordinate system, in which the operator of kinetic energy has the form:

$$\hat{T} = -\frac{\eta^2}{2m} \cdot \frac{1}{r^2} \cdot \frac{\partial}{\partial r} \left(r^2 \frac{\partial}{\partial r} \right) \quad (3)$$

Consequently, if the system of atoms is a collection of noninteracting particles, then, in accordance with Eq. (1), we obtain the usual linear Schrodinger equation describing the quantum state of so-called spherical harmonic oscillators.

Therefore, as was shown by Gross and Pitaevskii for the first time [2], to form the Bose - Einstein condensate, atoms must interact, and the interaction potential is defined by the following expression:

$$V_{\text{int}} = \frac{4\pi\eta^2 a_0}{m} |\psi|^2 \quad (4)$$

Here, a_0 is the force constant of the interaction of atoms (or a so-called scattering constant); it is negative for atoms attracting one another and positive for atoms repelling one another.

Thus, on the basis of the above preconditions, the equation describing the wave function of Bose—Einstein condensate atoms can be written in the following form:

$$i\eta \frac{\partial \psi}{\partial t} = -\frac{\eta^2}{2m} \frac{1}{r^2} \frac{\partial}{\partial r} \left(r^2 \frac{\partial \psi}{\partial r} \right) + \frac{1}{2} k r^2 \psi + \frac{4\pi\eta^2 a_0}{m} |\psi|^2 \psi \quad (5)$$

Then we reduce Eq. (5) to the so-called canonical form. To do this, we introduce the following notation:

$$r = A_0 \rho, \quad t = B_0 \tau, \quad \psi = c_0 f. \quad (6)$$

Here, A_0 , B_0 , and C_0 are the characteristic parameters of the system under consideration, which will be defined below. Then ρ , τ , and f denote the dimension- less coordinate, the time, and the wave function.

Taking relations (6) into account and substituting them into (5), we obtain

$$i \frac{\partial f}{\partial \tau} = -\frac{\eta}{2m} \cdot \frac{B_0}{A_0^2} \cdot \frac{1}{\rho^2} \cdot \frac{\partial}{\partial \rho} \left(\rho^2 \frac{\partial f}{\partial \rho} \right) + \frac{k}{2\eta} A_0^2 B_0 \rho^2 f + \frac{4\pi\eta a_0}{m} B_0 c_0^2 |f|^2 f \quad (7)$$

Then, rewriting the last equation in the form of the canonical Gross—Pitaevskii equation

$$i \frac{\partial f}{\partial \tau} + \frac{1}{\rho^2} \cdot \frac{\partial}{\partial \rho} \left(\rho^2 \frac{\partial f}{\partial \rho} \right) - \frac{1}{2} \rho^2 f - S |f|^2 f = 0 \quad (8)$$

we obtain the following conditions for determination of the characteristic parameters:

$$\frac{\eta}{2m} \cdot \frac{B_0}{A_0^2} = 1, \quad \frac{k}{\eta} \cdot A_0^2 B_0 = 1, \quad S = \frac{4\pi\eta a_0}{m} B_0 c_0^2. \quad (9)$$

Hence it follows that the characteristic distance A_0 , and the time B_0 are determined by the masses m and the force constant of k atoms forming the Bose condensate:

$$B_0 = \sqrt{\frac{2m}{k}}, \quad A_0 = \sqrt{\frac{\eta}{kB_0}}. \quad (10)$$

And finally, in accordance with the last condition (9), we find that

$$c_0^2 = \frac{mS}{4\pi\eta a_0 B_0^2}, \quad (11)$$

This formula expresses the density of Bose-condensate particles. Consequently, $c_0^2 A_0^3$ characterizes the number of atoms passed to the condensed state.

2. Averaged Lagrangian of solitons in the Bose - Einstein condensate

As is known, to obtain the equation of motion (irrespective of the fact whether this approximation is classical or quantum) of any physical system, it is necessary to determine its Lagrange function, or Lagrangian. Then, in accordance with the principle of least action (or the variational approach), the equations of motion for the system are described by the Euler - Lagrange equations. Therefore, the aim is to find the Lagrangian for solitons in the Bose - Einstein condensate.

Then we use the method of the averaged Lagrangian, which was proposed and developed in [4 - 6], taking into account that the Gross - Pitaevskii equation (8) includes the following “conservation laws”, or the integrals of motion:

$$I_1 = 4\pi \int_0^{\infty} \rho^2 |f|^2 d\rho \quad (12)$$

$$I_2 = 4\pi \int_0^{\infty} \rho^2 d\rho \left[\left| \frac{\partial f}{\partial \rho} \right|^2 + \frac{1}{4} \rho^2 |f|^2 + \frac{1}{2} S |f|^4 \right]. \quad (13)$$

Here, the first integral expresses the number of solitons in the Bose - Einstein condensate and the second, their energy. It follows from (12) and (13) that, if the solitons are not affected by an external force, then their number and energy are conserved.

When external fields (or perturbation, as they say) act on the collection of atoms forming the Bose condensate, the parameters of the solitons are changed. In particular, the wave function of solitons, which has the following form, can be altered:

$$f(\rho, \tau) = A(\tau) \exp \left[-\frac{\rho^2}{2a^2(\tau)} + \frac{i}{2} b(\tau) \rho^2 + i\varphi(\tau) \right]. \quad (14)$$

Here, $A(\tau), a(\tau), b(\tau)$ and $\varphi(\tau)$ expresses the respective amplitude, width, local frequency, and the phase of the wave function of solitons (or, simply speaking, the parameters of the soliton solution (14)).

It is natural that, under the action of rather strong perturbations, which are functions of coordinates and time, determination of the solution of the Gross - Pitaevskii equation becomes a problem. But from the physical point of view, the cases where external perturbation is weak are most important; i.e., the analysis of changes in steady-state and soliton solutions is important. It is this case where the method of the averaged Lagrangian is used; it assumes the adiabaticity of perturbations. This means that wave function (14) is conserved, but its parameters are slowly varying time functions.

Before finding the averaged Lagrangian of solitons in the Bose - Einstein condensate, we determine their number and energy using wave function (14) and calculating integrals (12) and (13). We obtain the following expressions for them:

$$I_1 = \pi \sqrt{\pi} A^2 a^3 \quad (15)$$

$$I_2 = \frac{\sqrt{\pi}}{4} A^2 a \left\{ \frac{3}{2} \left[a^4 \left(b^2 + \frac{1}{4} \right) + 1 \right] + \pi S A^4 a \right\} \quad (16)$$

Now we pass to determination of the averaged Lagrangian of solitons in the Bose - Einstein condensate:

$$\bar{L} = \int dV L \equiv 4\pi \int_0^{\infty} \rho^2 d\rho L \quad (17)$$

The Lagrange function L , from which the canonical Gross - Pitaevskii equation (8) is obtained, has the following form (it is not difficult to be convinced of it):

$$L = |f|^2 + \left| \frac{\partial f}{\partial \rho} \right|^2 + \frac{1}{4} \rho^2 |f|^2 + \frac{1}{2} S |f|^4 + \frac{i}{2} \left(f^* \frac{\partial f}{\partial \tau} - f \frac{\partial f^*}{\partial \tau} \right). \quad (18)$$

Taking the last term in expression (18) into account and integrating (17), we obtain the following general expression for the averaged Lagrangian of solitons in the Bose - Einstein condensate:

$$\bar{L} = \frac{\sqrt{\pi}}{4} A^2 \left\{ \frac{3}{2} \left[a^5 b^2 + a + \frac{a^5}{4} \right] + \pi S A^2 a^2 \right\} + 2\pi A^2 \left[\frac{db}{d\tau} \cdot \frac{3\sqrt{\pi}}{8} a^5 + 2 \frac{d\varphi}{d\tau} \cdot \frac{\sqrt{\pi}}{4} a^3 \right]. \quad (19)$$

Conclusion

Based on the above studies, we obtained the following results:

1. A brief derivation of the Gross-Pitaevskii equation describing the wave function of the atoms of the Bose-Einstein condensate is given.
2. The averaged Lagrangian of solitons of the Bose-Einstein condensation is found, on the basis of which it is possible to study the dynamics of solitons under the action of various perturbations.

Acknowledgments

This work was supported in part by a grant OT-A2-64 and ËΦ2-1, Uzbekistan.

REFERENCES

- 1 Lifshits E.M., Pitaevskii L.P. Course of Theoretical Physics. Vol. 9: *Statistical Physics, Part 2: Theory of Condensed State*. Moscow, Nauka, 1978, 314 p. [in Russian].
- 2 Pitaevskii L.P., Stringari S. *Bose-Einstein Condensation*. Clarendon Press, Oxford, 2003, 382 p.
- 3 Anderson D. *Variational approach to nonlinear pulse propagation in optical fibers*. *Phys. Rev.* 1983, A 27, pp. 3135-3145.
- 4 Malomed B.A. *Emission, quasi classical quantization and stochastic decay of sine Gordon solitons in external fields*. *Physica D*. 1987, V27, pp. 113-157.
- 5 Prez-Garcia V.M., Michinel H., Cirac J.I., et al. *Parametric resonance in Bose-Einstein condensates with periodic modulation of attractive interaction*. *Phys. Rev.* 1997, A 56, pp.1424-1429.

UDC 621.791.75

FRACTAL STRUCTURE OF MULTI-ELEMENT COATINGS

Guchenko S.A., Zavatskaya O.N., Yurov V.M., Kasymov S.S., Laurinas V.Ch.

Karaganda State University. E.A. Buketova, Karaganda, Republic of Kazakhstan, exciton@list.ru

The paper shows that the surface layer of a metal is a nanostructure. This surface layer possesses nonlinear properties that depend on its size and all physical properties. The phenomenon of electron emission from a metal under the action of an external electric field is considered. Taking into account the dimensional dependence of the conductivity of the surface layer leads to the Mandelbrot equation. This result shows that the surface layer has a fractal structure. The study of fluctuations of the contact potential difference on samples made of structural metal alloys is carried out. It has been experimentally established that the magnitude of the fluctuation of the contact potential difference at one point of the sample does not depend on the surface roughness. Several mechanisms that lead to fluctuations in the contact potential difference are considered. The first mechanism is associated with the thermal motion of the atoms inside the sample. The second mechanism is related to the processes occurring on the surface of the sample. The third mechanism is related to the processes in the measuring instrument.

Keywords: coating, microstructure, fractal, microhardness, friction, surface tension

Introduction

In the second half of the 20th century, a mathematical content was found in all existing and observed material objects, in their geometry, structure and behavior. Thus the idea of the fractal geometry of Nature of Benoit Mandelbrot [1] arose. Fractal changed the philosophy of measures. Fractal relationships between scales, fractal parameters and conventional quantitative parameters are used in many studies to describe the subtle world of fractals from nucleation to growth, from micro-macro and from local to global.

In [2, 3] a fractal analysis of the basic elements of the microstructure, such as the arrangement of atoms or molecules, dislocations, grains, surface particles, boundaries, etc., was carried out. Since microstructures are closely related to the properties of solids, a qualitative description of the images of microstructures may be insufficient and incapable of requirements for the development of materials. Therefore, quantitative measurements of the basic elements become more and more necessary. A new classification of basic elements in microstructures is introduced in terms of fractal dimension, as well as introduction to digital imaging, image processing and measurement of parameters.

In work [4] theoretical and practical aspects of the tribological process with the use of synergistic, fractal and multifractal methods, as well as fractal and multifractal models of self-similar tribosystems, developed on their basis are considered. They provide a comprehensive analysis of their effectiveness, and also consider the method of flicker-noise spectroscopy with detailed parametrization of friction of the surface roughness. All models, problems and solutions are taken and tested on the basis of real examples of the oil and gas industry.

The paper [5] is the first systematic exposition of the theory of local iterated functional systems, local fractal functions and fractal surfaces and their connections with wavelets. In [6], for example, in Chapter 4, two- and three-phase fractal methods are used to develop models of capillary pressure curves that characterize the distribution of porous media in pore sizes. The theory of percolation provides a theoretical basis for flow and transport modeling in disordered networks and systems. Therefore, following Chapter 4, in Chapter 5, the fractal basis of the theory of percolation

and its application in surface and subsurface hydrology is discussed. Chapter 6 shows that fault networks are modeled using fractal approaches. Chapter 7 presents various applications of fractals and multifractals for petrophysics and the corresponding field in petroleum engineering. In Chapter 8, we present the practical advantages of fractals and multifractals in geostatistics on a large scale, which are widely used in stochastic hydrology and hydrogeology. Multifractals are also widely used to model atmospheric characteristics, such as precipitation, temperature and the shape of clouds.

The analysis of time series over several decades was carried out in the fields of physics, hydrology, atmospheric research, civil engineering and water resources. Therefore, in Chapter 11 fractal, multifractal, and multifractal fluctuations are proposed, which can be used to study the temporal characteristics of a phenomenon, such as the discharge of a stream at a particular point in the river. Work [7] gives an idea of the advantages and limitations of using fractals in biomedical data. Also, the properties of biological data in relation to fractals and entropy are considered, as well as the connection with health and aging. The paper presents a detailed description of new methods of physiological signals and images based on fractal and chaotic theory. As follows from a brief and incomplete survey, fractals are used in materials science [2], tribology [4], hydrology [6], biology [7], etc.

In this paper, we consider the fractal structure and physical properties of the ion-plasma coating.

1. Experimental procedure

In this work we used multi element cathodes of Cr-Mn-Si-Cu-Fe-Al, Zn-Al, Mn-Fe-Cu-Al, obtained by induction melting, and Ti cathodes. Coatings were applied to steel samples by the ion-plasma method at the vacuum installation NNV-6.6I1. Electron microscopy was performed on a scanning electron microscope MIRA 3 from TESCAN. The investigations were carried out at an accelerating voltage of 20 kV and an operating distance of about 15 mm. For each sample, 4 images were taken from 4 surface points at different magnifications: 245 times, 1060 times, 4500 times and 14600 times. And also an energy-dispersive analysis was carried out at 4 points of the surface of each sample.

The optical microstructure was studied with the Epikvant metallographic microscope, and at the nanoscale with the NT-206 atomic force microscope. Investigation of microhardness of coatings was carried out on a microhardness meter HVS-1000A. Tribological studies were carried out on the installation described in [8]. The dependence of the microhardness of the deposited coating on its thickness is described by the formula [9]:

$$\mu = \mu_0 \cdot \left(1 - \frac{d}{h}\right), \quad (1)$$

where μ is the microhardness of the deposited coating; μ_0 is a massive sample; h is the thickness of the deposited coating.

The parameter d is related to the surface tension σ by the formula:

$$d = \frac{2\sigma v}{RT}, \quad (2)$$

where σ is the surface tension of a massive sample; v is the volume of one mole; R is the gas constant; T is the temperature.

In the coordinates $\mu \sim 1/h$ ($1/h$ - the inverse thickness of the deposited coating), a straight line is obtained, the tangent of the slope angle which determines d , and the surface tension of the deposited coating (σ) is calculated from formula (2).

Show that the structure under consideration is fractal, using the ratio of the perimeter and the area of the planar figures to the structures formed in the surface layer of the material. It is known [10] that for each family of flat geometric figures, the ratio of the perimeter L to the area remains constant and does not depend on the size of the figure:

$$\gamma = \frac{L}{S^{1/2}}. \quad (3)$$

However, if the structure is fractal, then, as shown in [10], it should be replaced by:

$$\gamma_D = \frac{L(\lambda)^{1/D}}{S(\lambda)^{1/2}}. \quad (4)$$

where D is the fractal Hausdorff dimension of the structure under consideration.

The ratio (4) does not depend on the size of the fractal structure, but depends on the choice of the standard of length ℓ , since the length of the self-similar boundary of the fractal $L(\ell)$ depends on the length of the standard with which it is measured and $L(\ell) \rightarrow \infty$ as $\ell \rightarrow 0$. The area of the fractal remains finite as $\ell \rightarrow 0$ and is defined as:

$$S(\lambda) = N\lambda^2, \quad (5)$$

where N is the number of cells of area ℓ^2 necessary to cover a flat fractal.

In general, fractal structures with self-similar boundaries satisfy the perimeter and area ratio [10]:

$$L(\lambda) = C\lambda^{1-D}[S(\lambda)]^{D/2}, \quad (6)$$

where C is the coefficient of proportionality.

The relation (6) is satisfied for any standard of length ℓ sufficiently small to measure the smallest of the fractal sets. The fractal dimensions were calculated from the AFM images at the height of the median plane.

2. Results of the experiment and their discussion

Figure 1 shows, by way of example, an electron microscopic image of the Cr-Mn-Si-Cu-Fe-Al + Ti coating in argon and nitrogen. Titanium grains with a size of 1 to 10 μm in diameter are clearly visible. Materials with such a grain size are usually called large-crystal. In a nitrogen environment, the structure of the coating changes sharply (Figure 1 a), due to the formation of titanium nitride. In this case, the average grain size is 100-150 nm. Such coatings are called submicrocrystalline.

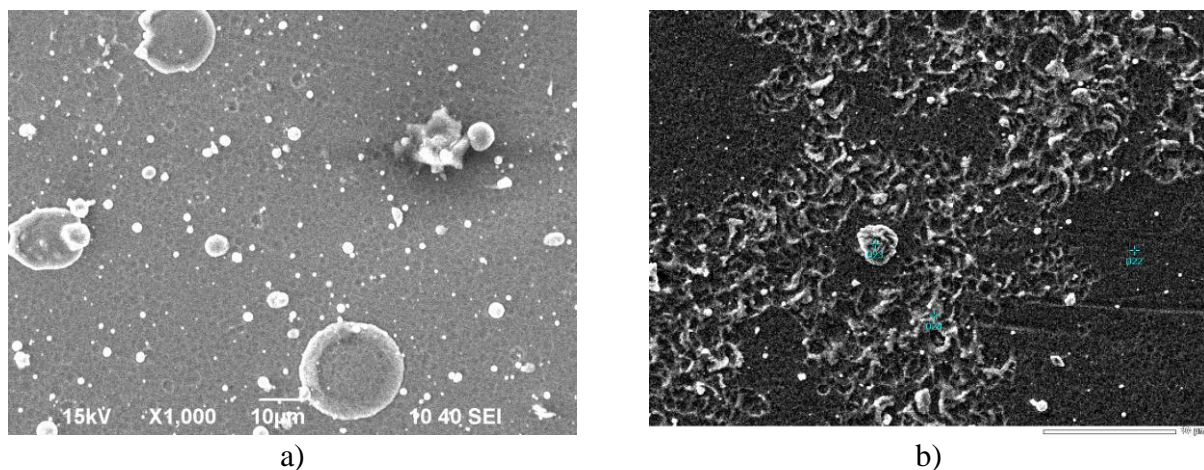


Fig.1. Electron microscopic image of the Cr-Mn-Si-Cu-Fe-Al coating in argon (a) and nitrogen (b).

The results of the quantitative XPS - analysis of the Cr-Mn-Si-Cu-Fe-Al + Ti coating in a nitrogen medium showed that the chromium, titanium and nitrogen content are close to each other. This suggests that, in addition to the formation of titanium nitride, the process of formation and chromium nitride occurs. From Fig. 1 that the microcrystallites of titanium and chromium nitrides have a predominant orientation (presumably in the (200) direction), which is also different from the

spherical symmetry of microcrystallites of pure titanium. Figures 2-7 show the AFM images and fractal structures of the metal composite films studied on steel X12.

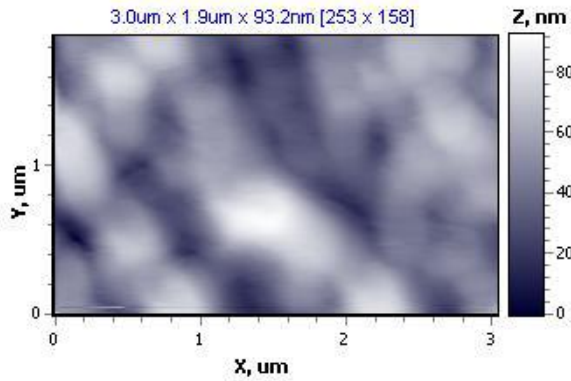


Fig.2. AFM image of the coating Cr-Mn-Si-Cu-Fe-Al+Ti

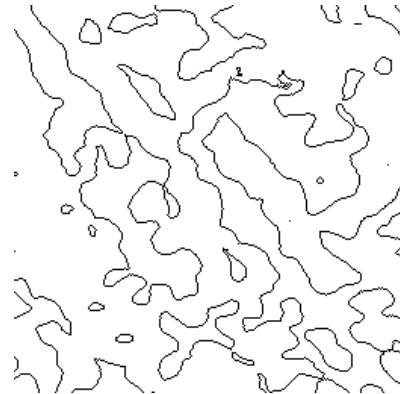


Fig.3. Fractal structure of the Cr-Mn-Si-Cu-Fe-Al+Ti coating

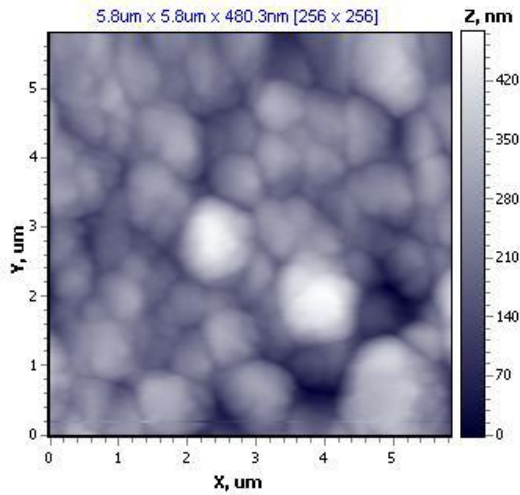


Fig.4. AFM image of the coating Zn-Al

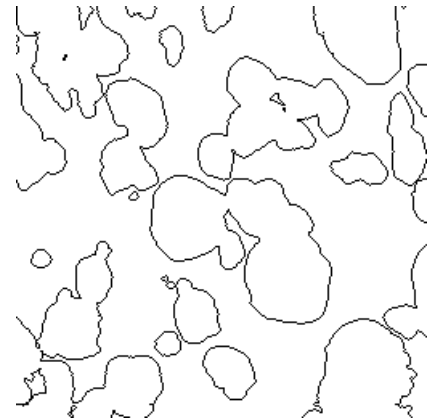


Fig.5. Fractal structure of the Zn-Al coating

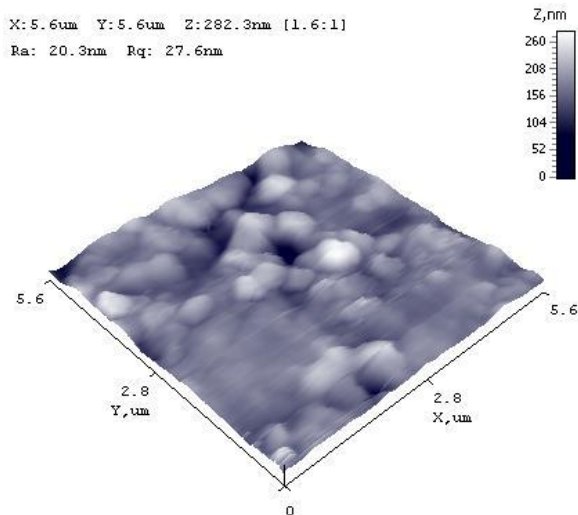


Fig.6. AFM image of the coating Mn-Fe-Cu-Al



Fig.7. Fractal structure of the Mn-Fe-Cu-Al coating

Table 1 - Roughness parameters and statistical characteristics of coatings

| Electrode | Roughness R_a , nm | Dispersion R_q | Asymmetry R_{sk} | Excess R_{ku} | Fractal dimension of structure D_s |
|----------------------|-------------------------|---------------------|-----------------------|--------------------|--|
| Cr-Mn-Si-Cu-Fe-Al+Ti | 78.0 | 99.7 | 0.44 | 3.46 | 1.89 |
| Mn-Fe-Cu-Al | 29.89 | 41.42 | 0.15 | 8.97 | 1.81 |
| Zn-Al | 13.34 | 18.23 | 0.17 | 7.35 | 1.79 |

In [11], within the thermodynamic approach for the coefficient of dry friction, we obtained the following formula:

$$k_t = C \cdot T \cdot \frac{A}{\mu} \cdot \bar{N}, \quad (7)$$

where A is the work (energy) of destruction, T is the temperature, μ is the chemical potential of the metal, \bar{N} is the average number of elementary carriers of destruction (proportional to the number of contacts), C is a constant.

From the formula (7) obtained by us, it follows that the coefficient of dry friction depends linearly on the work of failure of the contacts (roughnesses). Work A (J), spent on the destruction of contacts is proportional to the newly formed surface of the particles of the destroyed product:

$$A = \alpha \Delta S = K_R d^{D_s}, \quad (8)$$

where α is the time resistance to compression (Nm / m^2), ΔS is the area of the newly formed surface (m^2), K_R is the proportionality factor (Nm / m^2), d is the characteristic contact size (m), D_s is the fractal dimension.

Equation (7) can be rewritten as:

$$k_t = C \cdot K_R \cdot T \cdot \frac{d^{D_s}}{\mu} \cdot \bar{N}. \quad (9)$$

Taking the microhardness μ as the response function [11], we obtain

$$\mu = F \cdot \frac{d^{D_s}}{\mu} \cdot \bar{N}. \quad (10)$$

$F = \text{const.}$

Table 2 shows the fractal dimension of the coating and some surface properties. With a decrease in the fractal dimension, the surface tension, microhardness, and friction coefficient decrease. This agrees with formulas (9) - (10).

Table 2 - Fractal dimension and parameters of the coating

| Electrode | Surface tension (J / m^2) | Microhardness HRC | Coefficient friction | Fractal dimension D_s |
|----------------------|--|----------------------|-------------------------|----------------------------|
| Cr-Mn-Si-Cu-Fe-Al+Ti | 0.632 | 562.3 | 0.58 | 1.89 |
| Mn-Fe-Cu-Al+Ti | 0.342 | 420.4 | 0.46 | 1.81 |
| Zn-Al+Ti | 0.238 | 268.8 | 0.29 | 1.79 |

Fractal dimension is a necessary condition for the manifestation of self-organization [12]. Figure 8, for example, shows a 3D image of Cr-Mn-Si-Cu-Fe-Al+Ti and Mn-Fe-Cu-Al+Ti coatings.

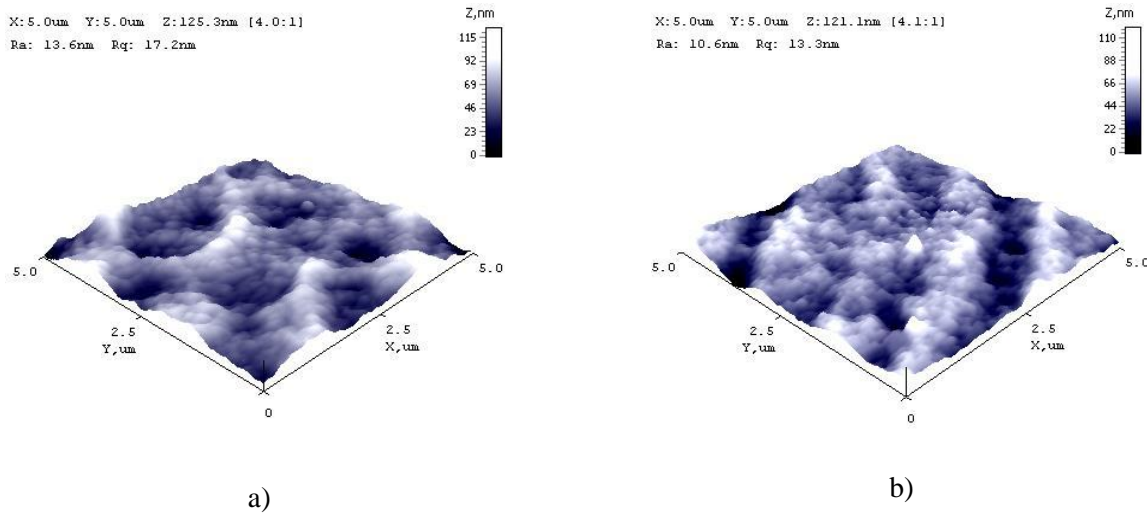


Fig.8. AFM images of Cr-Mn-Si-Cu-Fe-Al+Ti (a) and Mn-Fe-Cu-Al+Ti (b).

For most of the coatings studied, a cellular structure is observed. A cellular substructure is often formed upon solidification as a result of the occurrence of concentration supercooling [13]. If the formation of a cellular structure at the crystallization front has a zone of a liquid melt enriched in an impurity, then the appearance of impurity segregation at the cell boundaries is due to the lateral diffusion flow of the impurity from the top of the growing protuberance. The amount of impurity that actually reaches the cell boundary is difficult to measure, but it depends on the depth of the notch between the cells. As the supercooling increases, the depressions between the cells become deeper, which should lead to an enrichment of the cell boundaries by an admixture due to the diffusion of the impurity from the top of the cell. The concentration of impurities on the boundaries can be several times greater than the concentration at the center of the cell.

Such a model is quite suitable for explaining the observed cellular structure, where the role of the dopant is played by titanium nitride. However, there remains the question of the cause of the self-organization of the crystallizing melt on the surface of the substrate.

To solve the problem of the self-organization of the structural units of coverage, we consider the model of Benard cells. Benard cells are the emergence of order in the form of convective cells in the form of cylindrical shafts or regular hexahedral figures in a layer of viscous liquid with a vertical temperature gradient (Figure 9) [14].

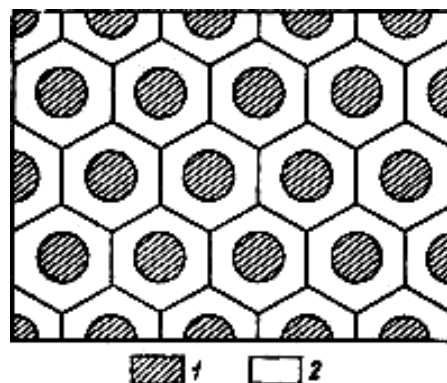


Fig.9. Diagram of Benard cells.
1 - upward movement, 2 - downward movement [14]

In the analysis of processes in the Benard system, the Rayleigh number is chosen as the control parameter: g is the acceleration due to gravity, L is the characteristic dimension, b is the coefficient of volumetric expansion, dT is the temperature gradient, ν is the kinematic viscosity, and a is the thermal diffusivity coefficient of the medium. Since the kinematic viscosity is $\nu \sim 1 / \sigma$, σ is the surface tension, it follows from the above expression for the Rayleigh number that the control parameter in our case is surface tension (Table 2). In the process of ion-plasma coating deposition and during cooling in the latter, stress states are formed which can be sources of multiplication of dislocations throughout the deposited coating. Plastic deformation of crystals (and coatings) is accompanied by the formation of a deformation relief on their surface that reflects the process of localization of deformations in the crystal at the meso-, micro- and nanoscale levels [15].

It is believed that a cellular dislocation structure is a process of self-organization of dislocations under conditions of multiple slip. For its occurrence, it is necessary to fulfill a certain criterion (as in the case of Benard cells), which relates the coefficients of multiplication, immobilization, and annihilation of dislocations.

Conclusion

The experimental data obtained in principle fit into all the models considered here: the concentration super cooling associated with the presence of a radial gradient of the concentration of an impurity of titanium nitride; Benard cells, the occurrence of which is due to the presence of a vertical temperature gradient; cellular dislocation structure associated with the presence of plastic deformations in the coating. The final choice of the model and, accordingly, the control parameter has not yet been made. It is possible that the process of coating formation is influenced by all mechanisms in one or a degree.

Acknowledgments

The work was carried out under the program of the Ministry of Education and Science of the Republic of Kazakhstan, Grant No. 0118RK000063.

REFERENCES

- 1 Mandelbrot B. *The fractal geometry of nature*. San Francisco: Freeman, 1982, 459 p.
- 2 Li J.M., Lü L., Lai M., Ralph B. *Image-Based Fractal Description of Microstructures*. Kluwer, 2003, 284 p.
- 3 Massopust Peter R. *Fractal Functions, Fractal Surfaces, and Wavelets*. Academic Press, 2016, 410 p.
- 4 Janahmadov A.Kh., Javadov M.Y. *Synergetics and Fractals in Tribology*. Springer International Publishing Switzerland, 2016, 391 p.
- 5 Brambila F. *Fractal Analysis: Applications in Health Sciences and Social Sciences*. ITOe, 2017, 218p.
- 6 Ghanbarian B., Hunt A.G. *Fractals: Concepts and Applications in Geosciences*. CRC Press, 2017, 364 p.
- 7 Kumar D.K., Aliahmad B., Arijunan S.P. *Fractals: applications in biological signalling and image processing*. Boca Raton: CRC Press, 2017, 191 p.
- 8 Yurov V.M., Laurinas V.Ch., Guchenko S.A., Zavatskaya O.N. *Surface tension of hardening coatings. Strengthening technologies and coatings*, 2014, No. 1, pp. 33 – 36.
- 9 Yurov V.M., Guchenko S.A., Laurinas V.Ch. *The role of surface tension in the formation of plasma coatings*. Scientific review. Technical science. - 2016, №4. – P. 124-139.
- 10 Feder J. *Fractals*. Springer Science. Business Media, LLC, 1988, 305 p.
- 11 Kubich V.I., Yurov V.M. The thermodynamic aspect of film starvation in triboconjugation. *Problemi tertya ta znoshuvannya*. 2016, No. 1(70), pp. 58 – 66.
- 12 Haken H. *Information and Self-Organization. A Macroscopic Approach to Complex Systems* (Springer Series in Synergetics). Springer - Verlag, New-York. 2006, 346 p.
- 13 Winegard W.C. *An Introduction to the Solidification of Metals*. London, Institute of Metals, 1964, 170 p.
- 14 Haken H. *Advanced Synergetics: Instability Hierarchies of Self-Organizing Systems and Devices*. - Springer, 1983, 371 p.
- 15 Malygin G.A. Modeling of the Deformation Relief of the Surface of a Plastically Deformed Crystal. *Solid State Physics*, 2007, Vol. 49, No. 8, pp. 1392 – 1397.

Article accepted for publication 23.04.2018

NONLINEAR RADIATION PROCESSES IN SOLIDS

Baktybekov K.S.

S.Seifullin Kazakh AgroTechnical University, Zhenis avenue, 62 Astana 010011 Republic of Kazakhstan,
k.baktybekov@gharysh.kz

There are some features in the research of the mechanisms of radiation exposure to solids, that complicate the understanding and quantitative description of such processes. First, the system "substance + radiation exposure" is open. In an open system, deviations of thermodynamic parameters from their equilibrium values lead to processes of energy and matter transfer. Secondly, the processes that occur as a result of the interaction of materials with radiation exposure are nonlinear. Continuous exchange of matter and energy with the environment leads to the fact that the system realizes stable dynamic equilibrium states that are far from the state of thermodynamic equilibrium. This conditions characterized by the existence of a certain spatial or temporal ordering so-called dissipative structure.

Keywords: *chaos and structures, fractal, modeling of radiation defects, thermoluminescence.*

Introduction

Recently, the radiation treatment of materials has been increasingly used. In this case, the radiation energy of electromagnetic, X-ray or gamma rays, as well as beams of charged particles are used. The main importance, such work was acquired in connection with the use of nuclear power and the possible use of thermonuclear installations. Materials used in outer space often experience complex effects of micrometeorites, electromagnetic and corpuscular radiation. All these processes lead to a change in the structure of the material, and, consequently, to the acquisition of new properties, which are often undesirable when the material is used.

The result of the substance interaction and external action is the formation of new structures in the materials under research, leading to a change in their original properties. Nonlinear systems are affected by random small effects generated by nonequilibrium, instability, and manifested in the accumulation of fluctuations, bifurcations, phase and spontaneous transitions.

The smallest parameter's change, controlling the nonlinear system can lead to a giant response of the system to an external action and, as a rule, leads to the self-organization effect studied by synergetics [1, 2]. The self-organization shows that elements of a non-linear dynamical system start to be ordered in the system structure, which leads to the formation of regular (fractals) or irregular (multifractals) spatial structures [3-6]. Thus, it can be assumed a priori that new structures formed in materials as a result of interaction with external action have a structure with fractional cluster dimension, i.e. the fractal analysis methods fractal can be used for their description.

The processes occurring during the interaction of radiation with matter are the simplest cases in which strongly nonequilibrium condition of a solid are formed. When it is irradiation, the fast particle collides with the substance atom, chooses it out of the node into the interstitial space. In this case, the lattice site remains empty, and two defects are formed: a vacancy and an interstitial atom (Frenkel defects). If a particle is heavy, for example a neutron or an ion, and if the energy of the particle is large enough, then, having extracted one of the atoms from the node and losing some of the energy, it can continue to collide until its energy runs out. In turn, an atom knocked out of a node can also have enough energy to produce defects. As a result, a cascade is formed, in which there can be several hundred pairs of defects.

1. Processes in irradiated solids

Let us consider how the condition of the irradiated solid changes in time by recourses [7, 8]. The irradiation source continuously generates defects in a solid. At the same time, the processes in which the defects are destroyed are in the substance. First, it is the annihilation process, when two opposite defects occur and mutually destroy each other. Secondly, the defect can "die on drains" if it approaches the external surface or internal drains - defects of a different type. Consequently, in the irradiated material, as a result of external action, defects are continuously created, but as a result of processes occurring in the solid, they continuously disappear, as a result of the balance of these processes, a certain steady concentration of defects is maintained. We can see that in this case a typical weakly nonequilibrium system should be observed, which behaves like a closed equilibrium system, but does not evolve to a state of equilibrium, but to a stationary state with a certain constant concentration of defects in the volume. In this case defects should be distributed approximately uniformly in the volume, if we do not take into account the regions of the cascades that play the role of fluctuations in the concentration of defects. However, experiments have been carried out experimentally [9], where the figure of radiation damage is significantly different from that described, spatially organized structures are observed, which apparently corresponds to the regime of strongly nonequilibrium conditions. In literature recourse [10] the system explanation of defected divergence of theory and experiment on the base of representations of dynamic chaos, which are in recombination-stimulating processes.

2. The results of modeling radiation-thermal processes

For the structural transformations analysis, occurring in the systems with two types of interacting particles, a quantity called the conditional interaction potential (CIP) is introduced in literature resource [11, 12]. This parameter allows us to characterize the size of the resulting structures and to reveal their fractal nature.

To calculate the CIP it is necessary to have a figure of the particle distribution on the surface under study or to know the spatial coordinates of the interacting molecules at the required time. The digitized image is divided into the same cells, and the scale of the partition runs through all values, which is a multiple of the original surface. The value of the CIP is calculated for their pair of particles in each cell, according to formula

$$U = \frac{1}{2} \sum_k \sum_{i,j} \frac{q_i q_j}{r_{ij}} \quad (1)$$

where i, j – component index of pair, k – number of interaction radius, determined by partition number, q_i, q_j – conditional single «charges», used for difference between two kinds of particles in a system ($q_i = 1, q_j = -1$ или $q_i = -1, q_j = 1$ in dependence of initial conditions), r_{ij} – distance between interacting particle.

A characteristic feature of the dependence of the CIP on the partition scale is the presence of one or more maxima, which indicate the formation of aggregates of the same particles. The UWB change in time makes it possible to trace the evolution of the observed structure in a solid. As a rule, the UWB time dependence has a minimum in the negative region, which corresponds to a maximum of information entropy, which corresponds to a chaotic distribution of particles on the surface and in the volume of the crystal. If the system has synergistic effects, its entropy decreases to a certain value. In this case, the CIP particle in the system grows to a certain positive value and reaches saturation. The kinetic curves at the saturation stage have a quasi-oscillatory character, which corresponds to the dynamic processes of growth and destruction of the clusters formed. It should be noted that the maximum of information entropy falls on the minimum of the conditional interaction potential (Figure 1), which also confirms the chaotic distribution of defects at this time.

This information entropy according to Haken [13] is defined as the average value of the synergetic information I , acquired at birth or structure destruction with probability p_i :

$$I_i = -\ln p_i, \quad S = -\sum_i p_i \ln p_i, \quad \sum_i p_i = 1. \quad (2)$$

This formula generally coincides with Shannon's entropy [14] -as a measure of the information necessary for determining the location of the system in a certain macrostate:

$$S = -\sum_i p_i \ln p_i, \quad (3)$$

However, these expressions have a different physical meaning. The formulation (2) can be used to research the system dynamics in the process of its evolution, while the entropy (3) describes the statistical condition of the system at this moment.

In Table 1 are shown the calculated values of the characteristic dimensions of aggregates, random entropy, and the observed entropy in modeling of long-term irradiation on lattices of different sizes [12].

Table 1. The information entropy values, calculated for some characteristic aggregates sizes and in a volumetric sites of different sizes

| The lattice size | Aggregates' Characteristic size | Observed system entropy | Chaotic distribution entropy |
|------------------|---------------------------------|-------------------------|------------------------------|
| 1000x1000 | 10x10 | 7.31 ± 0.10 | 9.21 |
| | 5x5 | 7.65 ± 0.12 | 10.59 |
| 500x500 | 10x10 | 7.09 ± 0.09 | 7.82 |
| | 4x4 | 7.48 ± 0.10 | 9.66 |
| 100x100 | 10x10 | 3.87 ± 0.05 | 4.60 |
| | 5x5 | 4.12 ± 0.00 | 5.99 |
| 100x100x100 | 10x10x10 | 6.83 ± 0.11 | 46.05 |
| | 4x4x4 | 8.58 ± 0.15 | 160.94 |

The defect structure destruction, formed by electron-hole centers accumulated in the crystal under the influence of radiation can be traced in the research of the process of thermoluminescence end thermally stimulated conductivity (TSC). The curves analysis of thermoluminescence (TL) arising in solids due to the recombination of charge carriers (electrons and holes) trapped by the lattice traps of a material is impossible without a detailed interpretation of the nature and mechanism of the dependence of thermoluminescence on crystal-chemical, physical-chemical and geological factors. It is known that the TL intensity depends on the number of recombining electron-hole centers in the crystal, the radiation dose rate and the duration of its exposure to the crystal. In connection with this, the TL process research was conducted of in order to elucidate the effect of the type of distribution of electron-hole centers in a crystal to the process.

When TL end TSC modeling, the experimental data of the activation energy and the heating rate from the work [7] for the NaCl crystal were used as the process parameters. The capture centers associated with radiation defects are mainly annealed to room temperature, and are F, F - aggregate and V-centers. The simplest mechanism of the recombination process realized in the model used is the migration of free charge carriers of the same sign to the captured charge carriers of the opposite sign. The TL curves correctness was verified by the Voigt's formulas (4), Broinlich formula (5), and Lushchik formula (6), which used in methods for determining the depth of the traps [15].

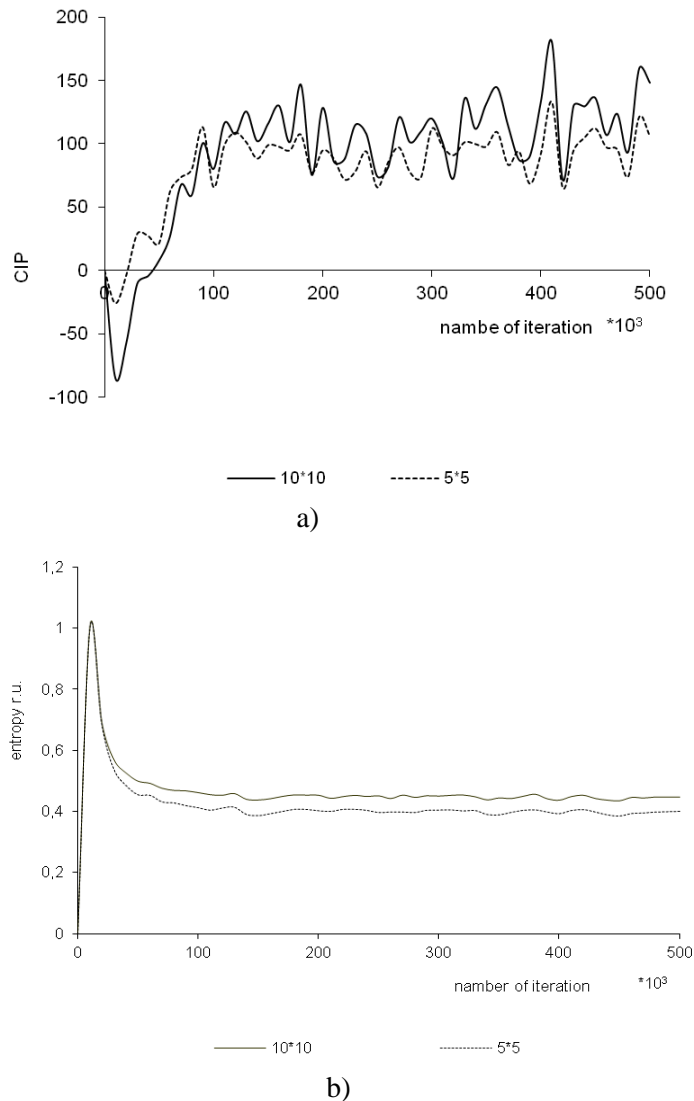


Fig.1. CIP dependence (a) and the specific value of information entropy (b) the structure of radiation defects from the duration irradiation of a two-dimensional NaCl crystal with a lattice of 1000x1000 at a dose rate of 0.1% for two characteristic sizes of aggregates.

There are shown the TL and TSC processes of modeling results in a NaCl-type lattice and the experimental data of the authors [7] in fig 2. The activation energies of the E centers calculated using the parameters obtained in modeling the TL process satisfy semi-empirical relationships:

$$18T_m \leq E/k \leq 25T_m, \tag{4}$$

$$E = \frac{kT_{m1} \cdot T_{m2}}{T_{m1} - T_{m2}} \ln \left(Q_1 T_{m2}^2 / Q_2 T_{m1}^2 \right), \tag{5}$$

$$E = kT_m^2 / (T_2^* - T_m), \tag{6}$$

where Q – the rate of crystal heating; T_m is the maximum temperature of thermoluminescence; T_2^* - temperature at half the maximum intensity of glow from the high-temperature side; k is the Boltzman’s constant; indices 1 and 2 denote the parameters for two TSL curves.

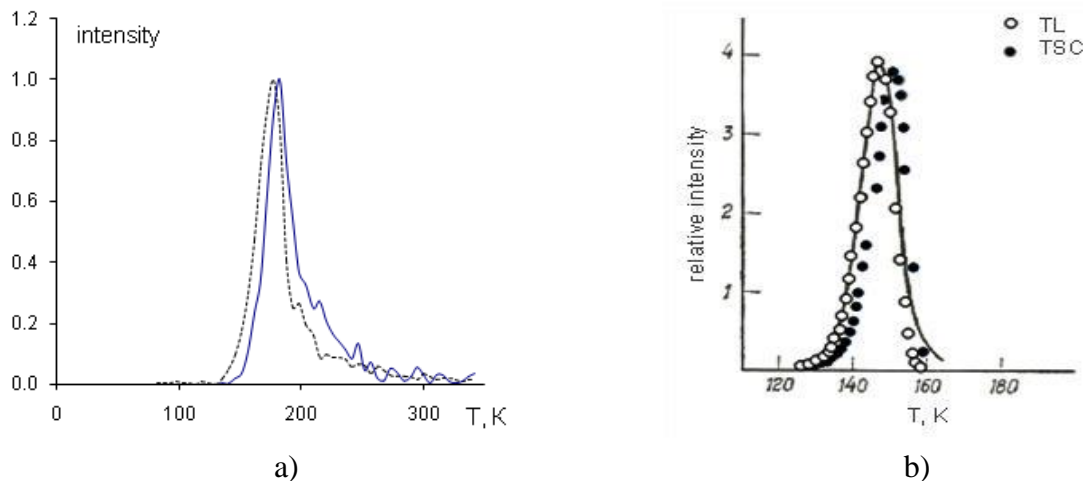


Fig.2. Curves TL и TSC: a) NaCl, computer modeling, $E/k = 3868$ K; TL _____ TSC;
 b) NaCl:Ag, experimental data [7], $E/k = 3868$ K

Conclusion

Thus, it can be argued that the mathematical model with the initial multifractal defect distribution adequately reflects the real system and can be used to the research the thermoluminescence phenomenon.

REFERENCES

- 1 Nikolis G., Prigogin I. *Self-organization in non-equilibrium systems*. Moscow, World, 1979, 512 p.
- 2 Glensdorf P., Prigogin I. *Thermodynamic theory of structure, stability and fluctuations*. Moscow, World, 1973, 280 p.
- 3 Zaslavsky G.M., Sagdeev R.Z., Usikov D.A., Chernikov A.A. *Weak chaos and quasi-regular structures*. Moscow: Science, 1991, 240 p.
- 4 Kronover R.M. *Fractals and chaos in dynamic systems. Fundamentals of the theory*. Moscow, Postmarket, 2000, 353 p.
- 5 Mandelbrot B. *The fractal geometry of nature*. San Francisco, Freeman, 1982, 459 p.
- 6 Bozhokin S.V., Parshin D.A. *Fractals and multifractals*. Izhevsk, SRC "RHD", 2001, 128 p.
- 7 Lushchik Ch.B., Vitol I.K., Elango M.A. Decay of electronic excitations into radiation defects in ionic crystals. *Uspehi Phisicheskikh Nauk*, 1977, Vol. 122, Issue 2, pp. 223 – 251. [in Russian]
- 8 Lisitsyn, V.M. Formation and Evolution of Primary Defectiveness in Ionic Crystals. *Proceeding of the Tomsk Polytechnic University*, 2000, Vol. 303, Issue 2, pp. 7 – 23. [in Russian]
- 9 Khmelevskaya V.S., Malyнкиn V.G. Dissipative structures in metallic materials after irradiation and other types of strong impact. *Materials Science*, 1998, Vol. 2, pp. 25 – 32. [in Russian].
- 10 Avilov A.B., Arapov B.A., Oxygenendler B.L. On the role of dynamic chaos in recombination-stimulated atomic processes. *Letters in ZhTPh*. 2000, Vol. 26, No. 2, pp. 23 – 27. [in Russian]
- 11 Baktybekov K., Vasil'eva I. The simulation of interaction of dielectric materials with soft space radiation. *Proceedings of the 9th Intern. Symposium on Materials in a Space Environment*. Nordwijk, 2003, pp. 719 – 721.
- 12 Baktybekov K.S., Vasilieva IF, Vertyagina E.N. Modeling of the aggregation of radiation defects in solids. *Bulletin of KarGU. Natural sciences*. 2003, Vol. 31, pp. 165 – 172.
- 13 Hacken G. *Information and self-organization*. Moscow, World, 1991, 240 p.
- 14 Shannon C.E. A mathematical theory of communication. *Bell Systems Tech. J.* 1948, Vol. 27, pp.379 – 423.
- 15 Broinlich P. Thermoluminescence and thermally stimulated current - methods for determining trapping parameters. *In the collection: "Physics of Minerals"*. Ed. A.S. Marfunin. Moscow: World, 1971, pp.134 – 155. [in Russian]

UDC 629.783

SPACECRAFT DISPOSAL IN QUASI-GEOSTATIONARY ORBIT

Ashurov A.E.

L.N. Gumilyov Eurasian National University, Astana, Republic of Kazakhstan,
ae_ashurov@yahoo.com

The results of simulation of the process of the disposal (post-mission disposal or disposal after failure as a result of emergency) of a spacecraft in quasi-geostationary orbit are given. The necessary impulses, fuel consumption for maneuvers, the required time for the raising the orbit to 300 km, changes in the major semi-axis and eccentricity of the orbit and the satellite's drift in longitude are calculated. The process of raising the orbit is considered as a result of successive starts of gas engines (GE) and corresponding changes in the indicated orbital parameters. The dependence of the satellite drift and longitude for different values of eccentricity is presented. It is shown that, within the maximum duration of the engine operation time of the GE, the duration of their individual starts does not significantly affect the final results of the disposal.

Keywords: Spacecraft; geostationary orbit; disposal; maneuvers; numerical simulations; orbit parameters

Introduction

A geostationary satellite whose service life ends, in accordance with the recommendation of the International Telecommunication Union [1], should be withdrawn from the geostationary orbit (GSO) area until the fuel stocks are exhausted in order to avoid the risk of collision with operating GSO satellites. At the same time, the minimum perigee height should ensure that the satellite does not return to the protected GSO zone after disposal from the geostationary orbit, which extends 200 km above the GSO. For satellites with orbital eccentricity $e < 0.003$, the required altitude is defined as:

$$\Delta H > 235 + 1000 Cr A/M,$$

where Cr is the coefficient of reflectivity at the beginning of the service life, A is the area of the satellite angle exposed to the Sun, M is the dry mass of the satellite.

The Control Center of these Spacecrafts (SC) should monitor the fuel consumption on board to ensure that the amount necessary for maneuvering to take off from the GSO is available. In addition, it is required to have a fuel stock to take into account the effect of possible inaccuracies in determining the orbit and the errors of maneuvering.

The results of work [2] show that geosynchronous orbiting satellites at the end of their service life should be brought to a height of not less than 300 km above the GSO.

Thus, the disposal of spacecraft from a geostationary orbit is regulated by international legal acts. Although they are recommendatory in nature, in fact, they are mandatory for implementation.

Since the issue of flight safety of satellites is always one of the most pressing issues, a lot of work is devoted to this issue. For example, it was shown in [3] that the required perigee altitude of the burial orbit cannot exceed 300 km from the height of the upper boundary of the protected region of the GSO. In addition, estimates of the necessary specific impulses of the control force for performing escape maneuvers consisting of a change in the major semi-axis of 500 km have been obtained. In particular, a specific impulse of about 18 m/s for a period of not more than one year is required for disposal from GSO.

An analysis of the fullness of GSO by spacecrafts, statistics of the disposal from orbit for 1997-2004 on the basis of TLE-elements was carried out in [4]. It is shown that at present, some of the satellites abandoned in GSO represent a danger to operating satellites. This once again proves the necessity of maneuvering the drift for each GSO satellite at the end of the active life or after failure as a result of an abnormal situation.

In [5-10] also problems related to the features of the disposal from GSO of satellites, including satellites possessing a non-zero, even significant inclination angle, are also considered. Taking into account the urgency of the problem of the SC disposal from GSO, the present work considers a method for modeling this process, for estimating the important parameters of such a maneuver: the necessary impulse, fuel consumption, required time, longitude drift and eccentricity changes. Since in most cases SCs are in a quasi-geostationary orbit with a small eccentricity and inclination angle, here we confine ourselves to this case. The case of moving a spacecraft from an ideal geostationary orbit ($e = 0$) was considered in [11].

1. Controlling the motion of the GSO satellite

Currently, geostationary satellite motion can be controlled using large and small thrust engines [12, 13]. In the case of high-thrust engines, it is assumed that the time it takes to create the necessary speed increment ΔV is negligible compared to the satellite revolution period. This kind of control is called impulse control. In this case, the action of the traction force is reduced to a sudden change in the velocity of the spacecraft without changing the coordinates during the time the engine is running [13]. Given the fact that this time is usually much shorter than the time of the orbital transition, this assumption is justified.

In the case of low-thrust engines, the running time of the engine becomes of the order of the satellite revolution period. In this case, the impact of the traction force on the orbit can be calculated by numerical integration of the differential equation of motion of the spacecraft, the acceleration due to the thrust of the engine [12, 14] on the right-hand sides of which is included. On this basis, in [15], the problem of controlling the planar parameters of the orbit of a geostationary spacecraft with the help of a low-thrust engine is solved. Since all maneuvers must be carried out from the optimality condition, in [16] the problem of optimizing the geostationary orbit with the use of an ionic low-thrust engine is considered.

As is known, if the inclusion of the engine can be considered impulse, then the velocity increment can be estimated as follows [11]:

$$\Delta V = \int_{t_0 - \Delta t / 2}^{t_0 + \Delta t / 2} \frac{\bar{F}}{m} dt \cong \frac{F \cdot \cos \alpha}{m} \Delta t \quad (1)$$

where \bar{F} is the vector of thrust, m is the mass of the space vehicle, α is the angle between the directions of maneuvering and thrust of the engine, t_0 is the calculated moment of the impulse, and Δt is the engine running time. In this case, the mass of the spacecraft can be considered constant during the operation of the engine. Since, in fact, the mass of the spacecraft is a function of time, if necessary, as the mass of the space vehicle, its mean value over the initial and final values during maneuver can be taken.

Of the three kinds of impulses (tangential, normal and lateral, or binormal), a tangential impulse is used to change the major semi-axis of the orbit, the drift speed in longitude and the eccentricity vector. Taking into account that in the problem considered by us, as a result of one small impulse ($\Delta V \ll V$), the major semi-axis changes by a small amount ($\Delta a \ll a$), it can be shown that [12-14]:

$$\Delta a = \frac{2a^2 V}{\mu} \Delta V, \quad (2)$$

where $\mu = fM$ is the gravitational parameter of the Earth.

The change of the major semi-axis is simultaneously accompanied by a change of the eccentricity e [12]:

$$\Delta e = \frac{2(e + \cos v)}{V} \Delta V, \quad (3)$$

where v is the true anomaly of the spacecraft.

Another parameter of the movement, which will change as a result of the change in the major semi-axis, is the satellite drift speed on the GSO. In the case of $e \neq 0$ and $i = 0$ (inclination of the orbit), the speed of drift is defined as [12]:

$$\dot{\lambda} = 2\pi \left(\frac{1 + 2e \cdot \cos v}{T_s} - \frac{1}{T_E} \right), \quad (4)$$

where T_s is the sidereal period of the satellite revolution, T_E is the duration of the stellar day.

The difference of the sidereal period from the stellar day will lead to the appearance of a drift along the longitude. In this case, the longitude of the spacecraft at time t is defined as (in the linear approximation):

$$\lambda = \lambda_0 + \dot{\lambda}(t - t_0), \quad (5)$$

where λ_0 is the longitude of the spacecraft before the start of the drift at the time t_0 .

The use of (4) allows us to take into account not only the evolution of the mean longitude, but also the longitude variations around the mean value, caused by the presence of eccentricity and natural short-period variations.

If in the process of transferring the spacecraft from one point of standing to another or when putting a burial place into an orbit, the eccentricity is not superimposed, then by means of a tangential impulse, a transferring can be started at any time.

2. Results of modeling and discussions

As in [11], we consider the process of moving a spacecraft from a GSO to a height of 300 km. The process of rising of the orbit will be considered as a result of successive starts of gas engines (GD) and corresponding changes in the indicated orbital parameters.

To simulate the disposal process, the following initial parameters have been adopted:

- the major semi-axis of the orbit is $a_0 = 42164125$ m;
- eccentricity $e_0 = 0$;
- circular speed $V_0 = 3075$ m/s;
- mass of space vehicle $m_0 = 1080$ kg;
- thrust of the engine $F = 0.009$ N;
- angle between the directions of maneuvering and engine thrust $\alpha = 60^\circ$;
- mass fuel consumption for one gas engine = 0.016 g/s;
- number of simultaneously operating gas engines $N = 4$;
- initial longitude of spacecraft $\lambda_0 = 103^\circ$;
- engine operating time $\Delta t = 1800$ s; 5000s.

Numerical simulation is performed in the following sequence.

1) Calculation of the increment of the velocity ΔV by the formula (1). In this case, for each individual maneuver, as spacecraft mass is taken its mean value $m_m = (m_{i-1} + m_i)/2$, where m_{i-1} and m_i are the masses of the spacecraft at the beginning and end of the maneuver. The spacecraft mass at the end of the maneuver is defined as $m_i = m_{i-1} - dm = m_{i-1} - \dot{m} \cdot \Delta t$.

2) Calculation of the change in the major semi-axis Δa by formula (2). At the same time, as the major semi-axis a and velocity V , values are taken that correspond to the beginning of the maneuver.

3) Calculation of the change in eccentricity Δe by formula (3). As in the previous case, as the velocity V , values are taken that correspond to the beginning of the maneuver. After the maneuver, the velocity, the major semi-axis and the eccentricity will become, respectively

$$V = V_0 + \Delta V, \quad a = a_0 + \Delta a, \quad \text{and} \quad e = e_0 + \Delta e.$$

4) Calculation the sidereal period of revolution of the satellite T_s corresponding to the changed major semi-axis a , and the duration of the stellar day T_E corresponding to the major semi-axis of the ideal orbit a_0 by the formula:

$$T = 2\pi \sqrt{\frac{a^3}{\mu}}.$$

5) Solution of the Kepler equation and finding the eccentric anomaly E , where M is the mean anomaly:

$$M = E - e \sin E.$$

6) Calculation of the true anomaly v :

$$\operatorname{tg} \frac{v}{2} = \sqrt{\frac{1+e}{1-e}} \operatorname{tg} \frac{E}{2}.$$

7) Calculation of the speed of the drift $\dot{\lambda}$ by the formula (4).

8) Calculation of the longitude value of the spacecraft at the end of the maneuver:

$$\lambda = \lambda_0 + \dot{\lambda} \cdot \Delta t.$$

In order to determine the effect of the duration of the engine on simulation results, in [11] the calculations were carried out at $\Delta t = 1800$ s; 3600 s and 5000 s. The last value is chosen based on the limitations on the duration of operation of some gas engines that are used in practice. Calculations showed that in all three cases the results are almost identical.

Since the case $e=0$ was considered in [11], in the present paper the effects on the results of modeling not only the duration of the engine operation, but also the eccentricity of the orbit are studied. For this purpose, we have considered the cases $\Delta t = 1800$ s and $\Delta t = 5000$ s with different eccentricity values (Table 1).

Table 1.

| e | $\Delta t, s$ | Nesc. time, day | $\Delta V, m/s$ | Fuel consumption, kg | Δe | $\Delta \lambda, \text{degree}$ | λ, degree |
|------|---------------|-----------------|-----------------|----------------------|------------|---------------------------------|--------------------------|
| 0.01 | 1800 | 7.3851 | 10.841 | 40.837 | 1.52e-04 | 13.418 | 89.582 |
| | 5000 | 7.3854 | 10.841 | 40.838 | 1.75e-04 | 13.268 | 89.732 |
| 0.03 | 1800 | 7.3851 | 10.841 | 40.837 | 1.51e-04 | 15.431 | 87.569 |
| | 5000 | 7.3854 | 10.841 | 40.838 | 1.75e-04 | 14.926 | 88.074 |
| 0.05 | 1800 | 7.3851 | 10.841 | 40.837 | 1.50e-04 | 21.715 | 81.285 |
| | 5000 | 7.3854 | 10.841 | 40.838 | 1.74e-04 | 20.836 | 82.164 |
| 0.07 | 1800 | 7.3851 | 10.841 | 40.837 | 1.50e-04 | 32.262 | 70.738 |
| | 5000 | 7.3854 | 10.841 | 40.838 | 1.74e-04 | 30.991 | 72.009 |

As can be seen from this table, the required time for rising of the orbit to 300 km, the necessary increment of the velocity ΔV and fuel consumption are practically independent of the eccentricity and the duration of the engine operation. In this case, the eccentricity of the orbit remains practically unchanged throughout the entire process of disposal. But the value of the eccentricity significantly influences the drift speed and the finite value of the longitude of the spacecraft.

The calculations showed a linear dependence of the change in the major semi-axis on time, and $\Delta a = 300$ km is achieved in 7.385 days. Figure 1 shows the longitude drift $\dot{\lambda}$ as a function of time for the two extreme values of eccentricity considered. As can be seen from the figure, the use of this expression for $\dot{\lambda}$ made it possible to reveal not only the evolution of the mean drift, but also its oscillations around the mean value, caused by the presence of eccentricity.

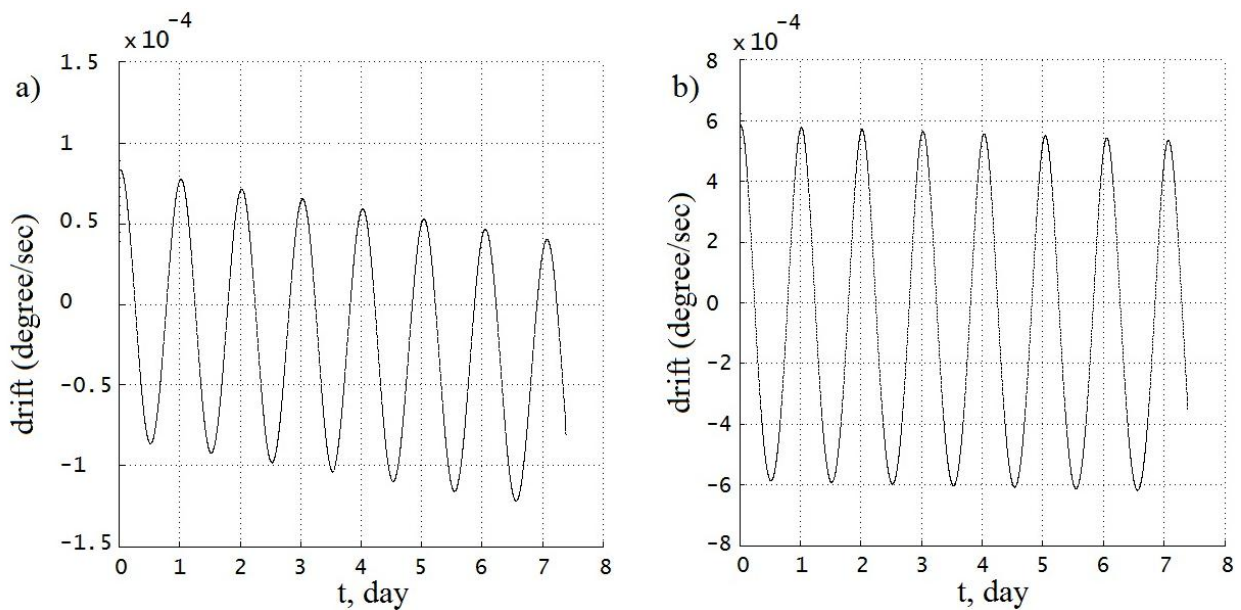


Fig. 1. Changes in the drift of the longitude ($\dot{\lambda}$) with eccentricity values $e = 0.01$ (a) and $e = 0.07$ (b).

Figure 2 shows the changes in longitude (λ) also with the two extreme values of eccentricity considered. Here, as well as in figure-1, not only the evolution of mean longitude, but also its oscillations around the mean value, caused by the presence of eccentricity and natural short-period variations, are revealed.

In both cases, an increase in the eccentricity resulted in an increase in the amplitude of the oscillations of the parameters considered, drift and longitude of the space vehicle.

On the basis of the results obtained, it can be argued that, when a spacecraft is taken from a GSO with permanently-powered engines, the eccentricity does not affect the fuel consumption and rise time of the orbit to the disposal orbit. But it has a significant influence on the drift and longitude change of spacecraft.

In order to test the need for such a simulation, we will consider the process of moving a spacecraft from a GSO as one whole maneuver.

Calculation of the velocity increment ΔV by the formula $\Delta V = \mu \cdot \Delta a / 2a^2 V$, where $\Delta a = 300$ km, $V = V_0 = 3075$ m/s and $a = a_0 = 42164125$ m gives $\Delta V = 10.94$ m/s. This value differs from the value of ΔV obtained as a result of modeling by less than 1%. This gives grounds to state that in order to estimate the necessary velocity increment ΔV to disposal spacecraft from GSO, there is no need for detailed simulation of the process.

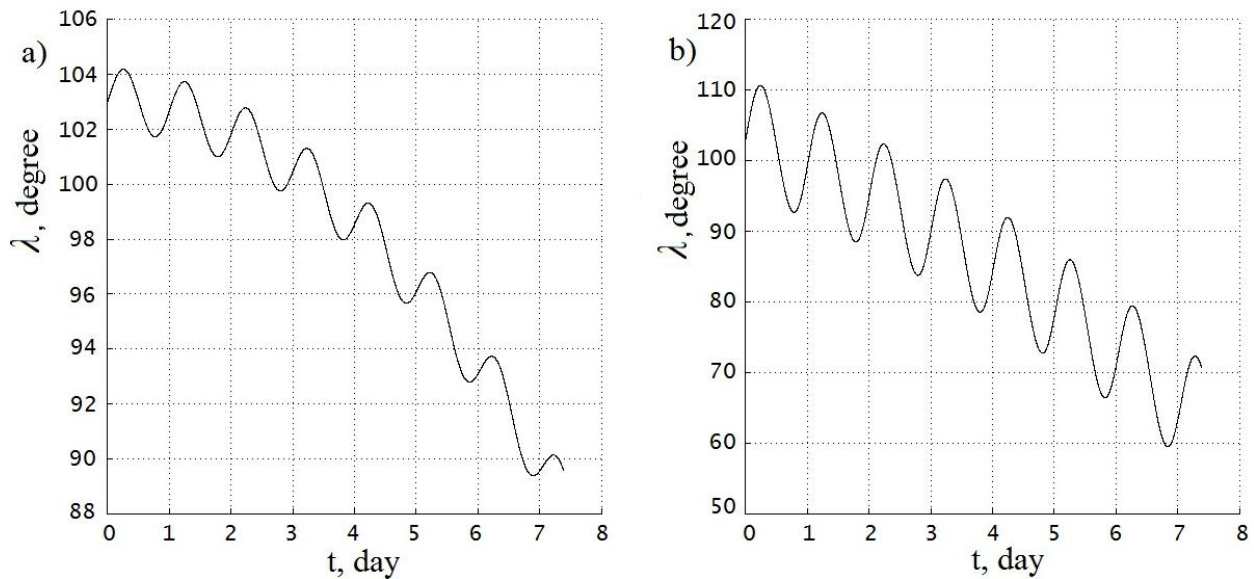


Fig. 2. Longitude changes (λ) for eccentricity values $e = 0.01$ (a) and $e = 0.07$ (b).

Similarly, calculating the change in eccentricity using the formula $\Delta e = 2 \cdot \Delta V / V$, where $\Delta V = 10.94$ m/s and $V = V_0 = 3075$ m/s also gives a very close values to the simulation results: $\Delta e = 0.0071$, which is a deviation of 1.43%.

Unlike the previous parameters, a significant difference arises in the estimation of the operating time of the engines: $\Delta t = \Delta V \cdot m / F \cdot \cos \alpha = 2625600$ s. Taking into account the fact that 4 engines operate simultaneously: $\Delta t = 656400$ s = 7.5972 days, i.e. the deviation is 0.2118 days.

As a consequence of the longer engine operation, there will be higher fuel consumption: 42.010 kg for the entire maneuvering period, i.e. 1.172 kg more than in the case of modeling.

The above parameters determine the longitude drift of the spacecraft. After moving the spacecraft to a height of 300 km above the GSO, the change in the period of revolution is $\Delta T = 921$ s. This in turn leads to drift = 3.8382 degrees per turn. Taking into account the disposal (moving) time at 7.5972 days, we get the longitude displacement $\Delta \lambda = 29.16$ deg., which differs from the simulated value by 14.979 deg. Thus, the spacecraft had to be at longitude $\lambda = 73.84$ deg.

A tangible difference in the estimates of the duration of the engine operation is associated with taking into account (or not taking into account) changes in the mass of the spacecraft due to fuel consumption. As a result of this, there are differences in the estimates of the total required fuel mass and changes in the longitude of the space vehicle.

Thus, it can be argued that a more accurate simulation of the SC disposal process from the GSO is justified in critical cases associated with the fuel stock, the time reserve for disposal or drift by longitude. This will allow you to choose the best variant for this maneuver.

Conclusion

Numerical simulation of the process of spacecraft disposal from a quasi-geostationary orbit to a height of 300 km has been carried out for the example of a spacecraft with a mass of 1080 kg, initial longitude 103° , equipped with gas engines. The changes in the major semi-axis and the eccentricity of the orbit, the longitude drift of the satellite, and the fuel consumption is considered as a result of consecutive starts of gas engines.

Simulation was carried out for three values of the duration of the engine: $\Delta t = 1800$ s; 3600 s; 5000 s. Calculations have shown that, within the maximum duration of the operations of gas engines, the duration of their individual operations does not significantly affect the final results of the disposal from orbit.

To assess the need for such a simulation, the process of moving SC from GSO is also considered as a one-time maneuver.

A tangible difference in the estimates of the duration of engine operation is due to the change in the mass of the spacecraft due to fuel consumption. As a result of this, there are differences in the estimates of the total required fuel mass and changes in the longitude of the space vehicle.

The analysis allows us to state that a more accurate simulation of the process of disposal of a spacecraft from a geostationary orbit is justified in critical cases associated with a fuel reserve, a time reserve for disposal or with a restriction on longitude drift.

REFERENCES

- 1 Recommendation ITU-R S.1003-2. *Environmental protection of the geostationary-satellite orbit. S Series. Fixed-satellite service.* Available at: <http://www.itu.int/rec/R-REC-S.1003-2-201012-I/en>. Date of the application: 14.06.2018.
- 2 Report by the Secretariat of the Committee on the peaceful uses of outer space. General Assembly. *Steps taken by space agencies for reducing the growth or damage potential of space debris.* A/AC.105/681, 17 December 1997. Available at: http://www.unoosa.org/pdf/reports/ac105/AC105_681R.pdf. Date of the application: 14.06.2018.
- 3 Doroshkevich V.K., Pirozhenko A.V., Xitko A.V., Xorolskyi P.G. By the definition of the requirements for the disposal systems of space objects. *AAEKS*. 2010, No.1, pp. 11 – 17.
- 4 Jehn, R., Agapov, V., Hernández, C. End-Of Disposal of Geostationary Satellites. *Proceedings of the 4th European Conference on Space Debris (ESA SP-587), ESA/ESOC, Darmstadt, Germany*, pp. 373-378.
- 5 Rosengren A. J., Scheeres D. J., McMahon J. W. The Classical Laplace Plane as a Stable Disposal Orbit for Geostationary Satellites. *Advances in Space Research*. 2014, Vol.53, No.8, pp.1219 – 1228.
- 6 Gkolias I., Colombo C. End of life disposal of geosynchronous satellites. *Proceedings of the 68th International Astronautical Congress*. Adelaide, Australia, IAC-17-A6.4.3. 2017, pp.1 – 13.
- 7 Mc Knight D.S., Di Pentino F. R. New insights on the orbital debris collision hazards at GEO. *Acta Astronautica*. 2013, Vol.85, pp.73 – 82.
- 8 Anderson P.V., Schaub H. Local debris congestion in the geosynchronous environment with population augmentation. *Acta Astronautica*. 2014, Vol. 94, pp. 619 – 628.
- 9 Tang J., Hou X., Liu, L. Long-term evolution of the inclined geosynchronous orbit in Beidou Navigation Satellite System. *Advances in Space Research*. 2017, Vol.59, No.3, pp. 762 – 774.
- 10 Lücking C., Colombo C., McInnes C. R. Solar radiation pressure-augmented deorbiting: passive end-of-life disposal from high-altitude orbits. *Journal of Spacecraft and Rockets*. 2013, Vol. 50, pp. 1256 – 1267.
- 11 Ashurov A.E. Simulation of the Spacecraft disposal in geostationary orbit. *Herald of the L.N. Gumilyov Eurasian National University*. 2016, No.6, Part II, pp. 241 – 246.
- 12 Chernjavskiy G.M., Bartenev V.A., Malyshev V.A. *Control of the geostationary satellite orbit*. Moscow, Mashinostroenie Publ., 1984, 144 p. [in Russian]
- 13 Ivanov N.M., Lysenko L.N. *Spacecraft ballistics and navigation*. 2004, Moscow, Дрофа, 544 p.
- 14 Soop, E. M. *Introduction to Geostationary Orbits*. European Space Agency, Scientific & Technical Information Branch, 1983. 143 p.
- 15 Salmin V.V., Chetverikov A.S. Control of in-plan orbit parameters of a geostationary low-thrust satellite. *Herald of the Samara state aerospace university*. 2015, Vol.14, No. 4, pp. 92 – 101.
- 16 Goodyear A.M. S, Spencer D.B. Optimal low-thrust geostationary transfer orbit using legendre-gauss-radau collocation. *Astrodynamic*s. 2016, Vol. 156, pp. 3073 - 3088.

UDC 539.32

X-RAY STRUCTURAL STUDIES OF POLYETHETRAFLUOROETHYLEN

Kupchishin A.I.^{1,2}, Tlebaev K.B.¹¹AbayKazakh National Pedagogical University, Almaty, Kazakhstan, ankupchishin@mail.ru²al-Farabi Kazakh National University, Almaty, Kazakhstan

X-ray diffraction studies of ultradisperse powder, ordered with the spiral structure of industrial (F-4) and modified polytetrafluoroethylene (PTFE) on different X-ray machines with different shooting conditions were performed. The obtained X-ray diffraction patterns are noticeably differed between themselves. In contrast to X-ray diffraction patterns of ultrafine powder, which has two reflexes and a modified PTFE with a single reflex, on the fluoroplastic-4 X-ray diffraction pattern, in addition to the polytetrafluoroethylene line, additional diffraction peaks (a wide diffuse halo and a series of reflections) that indicate the presence of several phases of fluoroplastic or a modification of the structure were found. The analysis of X-ray diffraction patterns showed that the standard PTFE line observed at an angle ($2\theta = 18.15^\circ$) is typical for all samples. It was established that the difference in X-ray diffraction patterns is due to the prehistory of obtaining PTFE samples.

Keywords: X-ray diffraction pattern, polytetrafluoroethylene, powder, ultra disperse, helical structure, hexagonal cell, lattice, sample, profile, crystalline object.

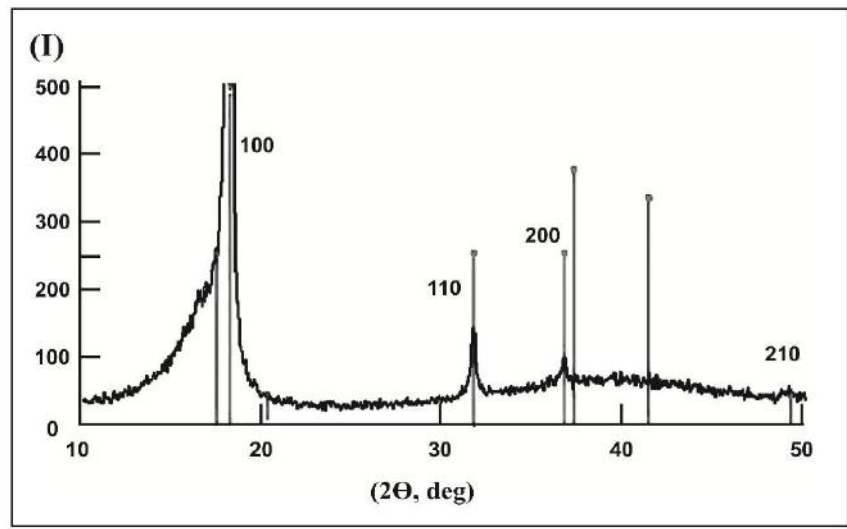
Introduction

In recent years, there has been a significant increased in interest in the radiation modification of polytetrafluoroethylene (PTFE) and composite materials based on it obtained by the action of beams of different particles, including high-energy electrons. The considerable attention to PTFE is associated with the discovery of a significant improvement in a number of important from the point of view of practical properties of this polymer after radiation exposure in the temperature region above the melting point.

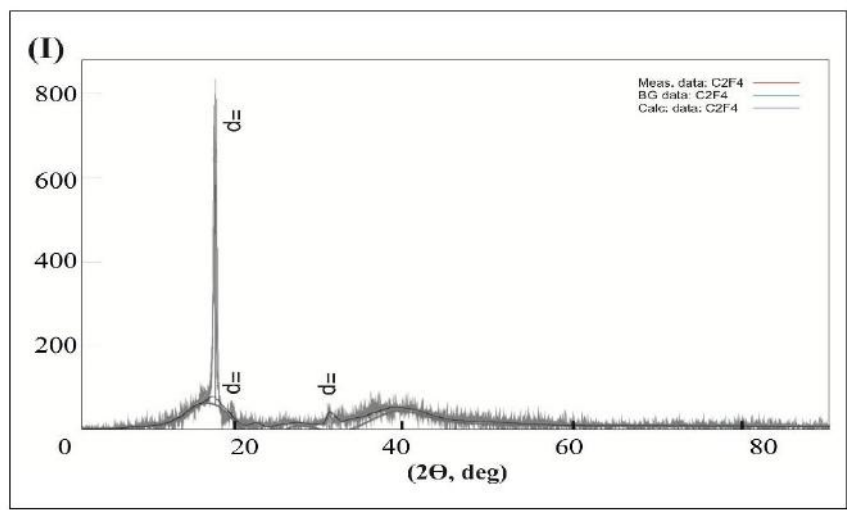
The main emphasis in this case is done on molecular mechanisms and molecular structure since the macroscopic properties of PTFE depend on its supramolecular structure and morphology. In this regard, the study of the morphology of the radiative modifications of PTFE along with the elucidation of molecular mechanisms is of independent interest especially when studying the properties of compositions based on PTFE with electrically conductive fillers of complex composition, a filler made from modified carbon fiber reinforced with quartz, using ultrafine inorganic compounds like aluminum-silicon oxynitride which is a solid refractory solution with an average particle size of 100 nm, at the study of modified PTFE films and their modification [1, 2]. Proceeding from the foregoing the considerable interest represents a study of the crystalline structure of PTFE which has a high degree of crystallinity both immediately after production of the material and at the present time. The special meaning information on the crystal structure is acquired in connection with the need to clarify the nature of various modifications and derivatives of PTFE including composite and ultra disperse materials and understanding their structure.

Therefore, for the analysis and interpretation of the structural structure of various modifications and derivatives of PTFE it is necessary to carry out a comparison with the data for industrial PTFE.

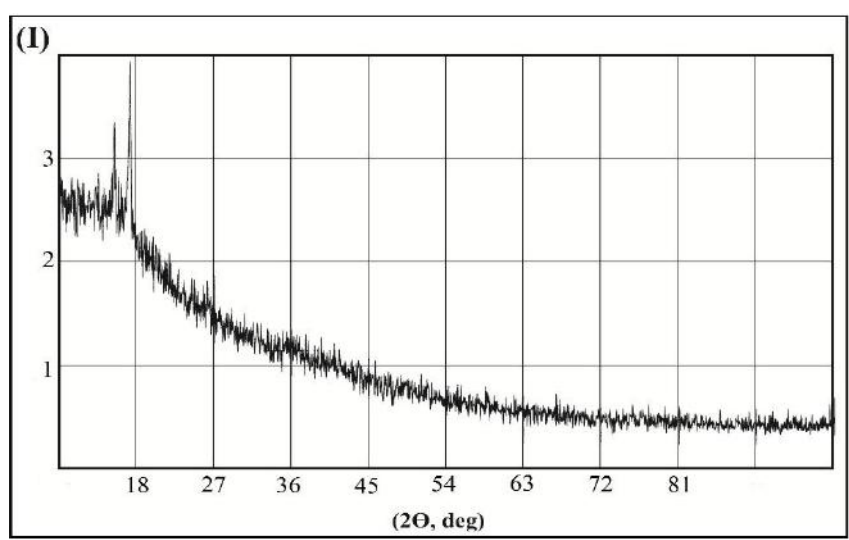
In this paper, profiles of X-ray patterns of samples of ultra disperse powder of (PTFE) (a), industrial PTFE-4 (b) and modified PTFE (c) have been studied (fig.1).



a



b



c

Fig.1. X-ray profiles of ultra disperse powder (a), PTFE-4 (b) and modified PTFE (c).

1. Experimental installations and measurement techniques

In the case of UPTFE the powder diffractometry method was used. X-ray diffraction data for a sample of PTFE were obtained on a MiniFlex-600 tabletop X-ray diffractometer from RIGAKU (Japan). The 5th generation MiniFlex-600 diffractometer is a multifunctional instrument intended for high-quality and quantitative phase analysis of polycrystalline materials.

MiniFlex is the only desktop X-ray diffractometer equipped with an automatic sample loader. The sample was an ultrafine PTFE powder. Survey conditions: tube voltage was 40 kV, tube current was 15 mA, and anode material was Cu, scan angle range from -3° to 145° (scanning dependent Θ - 2Θ). The scanning speed was from 0.01 to 100 $^\circ/\text{min}$ (2Θ). The minimum step is 0.005° (2Θ).

The X-ray diffractometer DRON-7 is a general-purpose diffractometer designed to measure the intensity and angles of diffraction of X-rays scattered by a crystalline object in solving X-ray diffraction and X-ray diffraction analysis of materials and is used in industrial, research and training works in various fields of science and production (materials science, ferrous and non-ferrous metallurgy, machine building, mineralogy, crystallography, chemistry, pharmacology, criminalistics and others). X-ray diffraction data of the modified sample were obtained by the DRON-7 diffractometer at $20 - 22^\circ$. The operation of the diffractometer is controlled from a personal computer (PC). It is designed to work with the following factors: a) ambient temperature from 10 to 35°C ; b) relative air humidity up to 80% at 25°C ; c) atmospheric pressure of 84 – 107 kPa (630 – 800 mm Hg) and provides operation with X-ray tubes of the type BSV27, BSV28 and BSV29 in the third design version.

The basic set includes an X-ray tube 2.5BCB27-Cu. The measuring range of angles 2θ is from minus 100 to plus 165° ; the measuring range of the angles is from 0 to 360° . The power of the diffractometer is provided by a single-phase alternating current network with a frequency of (50 ± 1) Hz, by the voltage of 220 V with a permissible deviation of $\pm 10\%$ from the nominal value. The power consumed by the diffractometer is not more than 5.5 kW.

The steady speed of angular movements along the axis of the bracket of the detection unit and the axis of the sample is at least 500 $^\circ/\text{min}$. The absolute error in measuring the angular positions of the diffraction maxima does not exceed $\pm 0.02^\circ$. The basic instrumental error in measuring the counting rate of X-ray pulses does not exceed 0.25 %.

When measuring the X-ray diffraction spectrum, a diffractometer with a PC provides automatic output of information to peripheral devices. The limit of the permissible deviation of the installation of the angular position of the bracket of the detection unit and the sample holder from the specified angle of rotation is ± 0.005 . The minimum scanning step is 0.001.

The diffractometer DRON-7 uses the characteristic CuK_α radiation with a wavelength $\lambda = 1.54178$ monochromatized with a monochromator crystal, the shooting step is 0.50. The scan interval is $10 - 100^\circ$ for 2θ shooting method: $2\text{THETA}-\text{THETA}$. Exposure = 1 sec.

X-ray diffractometry studies of an industrial fluoroplastic sample were performed on an automatic diffractometer Bruker D8 Advance with a digital recording of the measurement results. The survey was carried out in the geometry of a divergent X-ray beam with Bragg-Brentano focusing (BB). The D8 ADVANCE automatic x-ray diffractometer (Bruker AXS GmbH, Germany) is designed for X-ray diffraction studies of various crystalline materials in scientific research institutions and laboratories of industrial enterprises. The investigated samples were a fluoroplastic film reinforced on a glass substrate and a fluoroplastic plate with a thickness $h = 1.5$ mm cut from the cross-section of a rod with a diameter $d = 40$ mm.

To record the diffraction pattern at a temperature of 15°C , the fluoroplastic plate was placed on the tantalum tape of the heater of the high-temperature vacuum chamber with the front cover removed. Measurements at a temperature of 15 and 20°C were carried out at atmospheric pressure, heating the sample to 50 and 60°C was carried out after pumping the high-temperature vacuum chamber with a turbo molecular pump to a pressure of $1 \cdot 10^{-4}$ mm Hg. X-ray patterns of the samples

were obtained on a diffractometer using copper radiation and a graphite monochromator on a diffracted beam. The sample shooting mode was as follows: the voltage on the X-ray tube 40 kV at a current of 40 mA. The scanning step was 0.02 degrees 2θ ; the diffraction intensity measurement time at this step was 5.0 seconds. The sample in the standard holder rotated in its plane at a speed of 60 t/m. A high-temperature vacuum chamber was used for shooting intensity of diffraction at a sample temperature of 50 and 60 °C.

2. Results and discussion

On Figure 1a, b and c X-ray diffraction patterns of ultra disperse powder, PTFE-4 and modified PTFE are presented. As is seen from the X-ray diffraction patterns they differ from each other. On the other hand, for all PTFE samples with a scattering angle $2\theta = 18.158^\circ$ an intense peak characterizing the crystallinity of the sample is observed.

The X-ray pattern of the ultrafine PTFE powder is somewhat unusual for a crystalline substance there are two peaks one less intense $\sim 16.396^\circ$ (2θ) characterizing an amorphous halo and a disproportionately intense peak at 18.158° . The appearance of only two reflections of the form (h , k , l) means that this set of reflections (Table 1) is described by a planar (two-dimensional) hexagonal lattice with a parameter, $a = 5.681 \text{ \AA}$. The value of the lattice parameter corresponds well to the parameters of the PTFE unit cell at a temperature of 300 K [1]. The presence on the X-ray patterns of only basal type reflexes is caused by a strong predominant orientation of the particles on the surface.

Table 1. X-ray diffraction data of ultrafine PTFE powder $a = 5.653 \text{ \AA}$ for a planar symmetry group

| $2\theta^\circ$ | $d, \text{ \AA}$ | I, % | h | k | l |
|-----------------|------------------|-------|-----|-----|-----|
| 16.396 | 2.8271 | 100.0 | 1 | 0 | 0 |
| 18.040 | 4.9297 | 100.0 | 1 | 1 | 0 |

On X-ray diffraction pattern of industrial fluoroplastic-4 in contrast to ultrafine powder and modified PTFE there are a number of additional diffraction peaks and a wide flat region that can be interpreted by a phase transition $\text{II} \rightarrow \text{IV}$ from a triclinic lattice II to a three-dimensional hexagonal cell IV with parameters $a = 5.653 \text{ \AA}$, $c = 19.512 \text{ \AA}$ at a temperature of 293 K which also agrees well with the literature data [3, 4].

The phase transition $\text{II} \rightarrow \text{IV}$ consists in decreasing the twist of the helix from the state 13_6 (13 segments per six complete turns of the helix) to 15_7 in terms of helical symmetry. Further transformation is considered as a loss of ordering along the packing axis of macromolecules of the polymer which is manifested in the mutual rotation of individual, adjacent spirals [1].

On the X-ray diffraction pattern of the modified PTFE only one intense reflex is observed at an angle of $2\theta = 18.00^\circ$ corresponding to the crystalline form II. The absence of additional reflexes can be interpreted in that when pressing the powder under high pressure then heating above the melting point and abrupt cooling leads to the formation of crystalline form II, namely, the triclinic lattice.

Conclusion

1. New experimental data on the X-ray diffraction patterns of ultradisperse powder, industrial and modified PTFE have been obtained. It is shown that the X-ray diffraction patterns are strongly differed between themselves.

2. Comparison of the X-ray diffraction patterns of ultradisperse powder and modified PTFE with an industrial X-ray diffraction pattern revealed the nature of the structure of the powder and modified of PTFE.

3. The practical significance of the obtained research results will allow them to be used in the development of polymer composite materials based on PTFE for clarifying the nature and understanding of their structure.

Acknowledgements

This work was supported by the Project No 9 of the Ministry of Education and Science of Kazakhstan Republic

REFERENCES

- 1 V.M. Buznik, V.M. Fomin, A.P. Alkhimov et al. *Metal polymer nanocomposites*. Novosibirsk, Publishing house of the SB RAS. 2005, 56 p. [in Russian]
- 2 Prierce R.H., Clark E.S., Whitney J.F., Bryant W.M.D. Crystal Structure of Polytetrafluoroethylene. *Proceeding of the 130th Meeting of the American Chemical Society*, 1956, pp. 9 – 14.
- 3 Clark E.S. and Muus L.T. Technology of Fluoropolymers // *Z. Krist.*, 1962, B.117, pp. 108 – 118.
- 4 Clark E.S., Muus L.T. Technology of Fluoropolymers // *Z. Krist.*, 1962, B.117, pp. 119 – 127.

Article accepted for publication 24.01.2018

UDC: 530.1; 538.97; 539.216.1; 539.216.2; 539.23

ELECTRICAL PROPERTIES OF QUANTUM NANOWIRES

Zhanabaev Z.Zh.¹, Grevtseva T.Yu.¹, Ikramova S.B.¹, Filippov N.V.²¹National Nanotechnology Open Laboratory, Almaty, Kazakhstan,
²al-Farabi Kazakh National University, Almaty, Kazakhstan

In the present work we suggest equations for the description of electrical conductivity of semiconductor quantum nanowires. By use of these equations we explain such features of their current-voltage characteristics as existence of areas with negative differential resistance as well as oscillating behavior of the curves. We take into account scale-invariant, hierarchically self-similar, fractal structure of nanostructures. We consider that quantum nanowires form fractal clusters at their interaction. Electrical potential of these structures can be described as a fractal measure. Theoretical results are confirmed by specific experimental results on study of electrical properties of nanocluster semiconductors.

Keywords: nanostructure, morphology, fractal dimension, current-voltage characteristics, semiconductor.

Introduction

Investigation of structure and physical (including electrical) properties of nanoclusters semiconductors is one of the urgent problems of modern electronics. Unique physical properties of these materials make it possible to use them in different nanoelectronic devices such as nanosensors, solar cells, batteries, etc. [1-3].

Surface structure of nanocluster films is characterized by hierarchically self-similar and scale-invariant structure. This fact has been confirmed by experimental photographs obtained by use of modern methods of microscopy such as atomic force, scanning tunneling, electron microscopy [4-7]. Growth of films at non-linear and non-equilibrium conditions in open systems leads to formation on their surfaces of quantum-sized structures such as quantum nanowires, dots, wells with different arrangement. Type of nanostructures on a film surface significantly determines its electrical and optical properties.

Regularities of electrical conductivity of semiconductor nanowires have been described in many experimental and theoretical papers developing the theory proposed by Landauer for the description of quantum conductivity [8-10]. The theory is based on the description of tunnel contacts between two quasi-one-dimensional structures. However, universal approaches for explanation of processes related to this problem have not yet been completely established.

Recent studies have shown that current-voltage characteristics of semiconductor nanowires are generally non-monotonic functions and have a number of characteristic features such as oscillating behavior of curves of the current-voltage characteristics, hysteresis loops, existence of areas with negative differential resistance [11-15]. These features are inherent in current-voltage characteristics of semiconductor nanowires both at low (about several kelvins) and at room temperatures. Such behavior of the curves is typical for semiconductor nanowires with different chemical composition [16-18].

Electrical conductivity of semiconductor nanostructures depends on method used for growth of the film, and, therefore, on its porosity, types of nanostructures grown on the film surface and their mutual arrangement. Nowadays, there is no complete theory which is fully explaining the above-mentioned features of electrical conductivity of nanocluster semiconductor films (hysteresis loops on current-voltage characteristics, their oscillating behavior, amplitude and location of oscillations,

areas of current-voltage characteristics with negative differential resistance, etc.) depending on their nanoscale structure.

Earlier in our papers, we have explained some electrical properties of nanowires based on the idea of fractal structure of nanocluster semiconductor films [4-7]. Because of non-linear fluctuation properties, nanowires are self-similarly deformed and, interacting, form fractal clusters. A quantum nanowire has an irregular structure, so, for its description we must take into account not only value of external potential between electrodes, but also value of potential providing by internal non-uniform distribution of electrons. Values of this potential can be represented as non-linear fractal measures. As usual, nanoclusters have fractal geometrical structure.

So, such structures are characterized by multi-barrier tunneling effects leading to formation of areas with negative differential resistance and hysteresis loops in current-voltage characteristics of nanostructures [6, 18].

Aim of the present work is to describe by use of our equations some regularities of electrical conductivity of semiconductor thin films containing quantum nanowires.

1. Electrical conductivity of quantum nanowires

Electrical properties of quantum nanowires can be described by use of the approach suggested in our previous works [6, 18]. According to this approach, a separate nanostructure (quantum nanowire) can be considered as a resistor with ideal contacts, to which external voltage U is applied.

Quantum nanowires containing in semiconductor films can form fractal nanoclusters because of self-organization. These nanoclusters have different sizes and chaotically oriented to each other. Inside a cluster, an electron moves under action of so-called scattering potential $V(U)$ characterizing metastable statements. The cluster potential is an additive value and because of this it can be considered as a nonlinear fractal measure.

Considering that resistance R is also a fractal measure, the system of equations describing current I inside a nanowire, potential V of a fractal cluster and its electrical resistance can be described as

$$I(U) = \frac{V(U)}{R(U)}, \tag{1}$$

$$V(U) = V_0 \left(\left| 1 - \left| \frac{V(U)}{U} \right| \right| \right)^{-\gamma}, \tag{2}$$

$$R(U) = R_\lambda \left(\left| 1 - \left| \frac{U}{I(U)R(U) - V_0} \right| \right| \right)^{-\gamma}, \tag{3}$$

where $\gamma = D - d$ is scaling factor, D is fractal dimension of space where a single nanowire with topological dimension $d = 1$ is placed in, R_λ is resistance of a regular (non-fractal) wire, λ is the de Broglie wavelength.

Structure of nanoscale clusters formed in a film substantially determines regularities of electrical conductivity of the considered film. Singularities of surface structure of a nanostructured semiconductor film can be taken into account by corresponding choice of parameter γ . Due to the fact that properties of nanowires change as current passes through them, we accept difference between value of current and relation $V_0/R(U)$ in Eq. (3) as a determining variable.

2. Results and discussion

Current-voltage characteristic of a quantum nanowire obtained by numerical analysis of equations (1)-(3) is presented in Figure 1. As an estimated value, we can accept that $V_0 = E_g$, where E_g is value of silicon band gap measured in eV, because this value also characterizes the breakdown of energy values at the boundary of structures (Brillouin zones). According to physical meaning, $V_0 = E_g$ is maximal value of negative potential localizing an electron in a fractal cluster. We have used external voltage U as a determining variable. For the correct choice of numerical value of parameter $\gamma = D - d$ we have taken into account that generally value of topological dimension d isn't equal to maximal integer part of fractal dimension D . A quantum nanowire can be considered as a structure $d = 1$ and $1 < D < 2$. So, for our calculations we have accepted value of γ as $0 < \gamma < 1$.

As can be seen from the Figure 1, the current-voltage characteristic is a non-monotonic function, characterizing by oscillating behavior and contains areas with negative differential resistance. Oscillations of the curves related with nanocluster stricter of the films. Amplitude of oscillations is described by value of scaling factor γ by the following way: increase of the amplitude of oscillations corresponds to increase of γ . Figure 1 demonstrates that the current-voltage characteristic contains areas with negative differential resistance. It can be explained by fractality of geometry of formations consisting of quantum nanowires leading to multi-barrier tunneling effects.

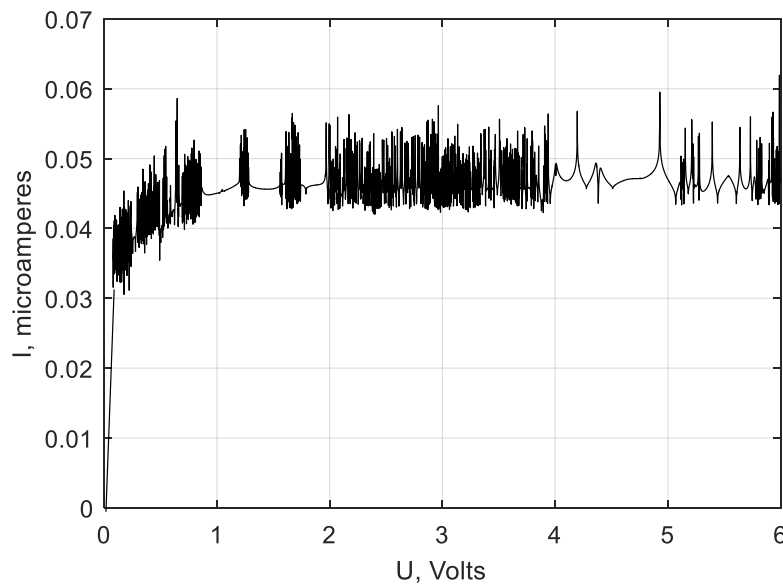


Fig. 1. Current-voltage characteristic of quantum nanowire.

$$V_0 = 1.12 \text{ V}, \gamma = 0.03.$$

Figure 1 also demonstrates that oscillations on curves of the current-voltage characteristic are clustered. This effect is confirmed by experimental studies described in [10, 13] and can be explained by quantization of conductivity in semiconductor thin films.

Clustering of oscillations is related to quantization of film conductivity presented in Figure 2. Dependence of resistance on external voltage presented in this figure has been obtained by use of Eqs. (1)-(3). Scaling factor used for modeling of this dependence is relatively small because of small difference between values of fractal and topological dimensions. Quantization of conductivity

corresponds with statements of the ballistic theory of electrical conductivity. According to these statements electrical resistance of a system depends on quantum effects in this system. It's necessary to notice that singularities of quantum effects observed in nanostructured semiconductor films are substantially determined by types of quantum-size structures contained in these films (quantum dots, quantum wells, quantum nanowires) and their relative position.

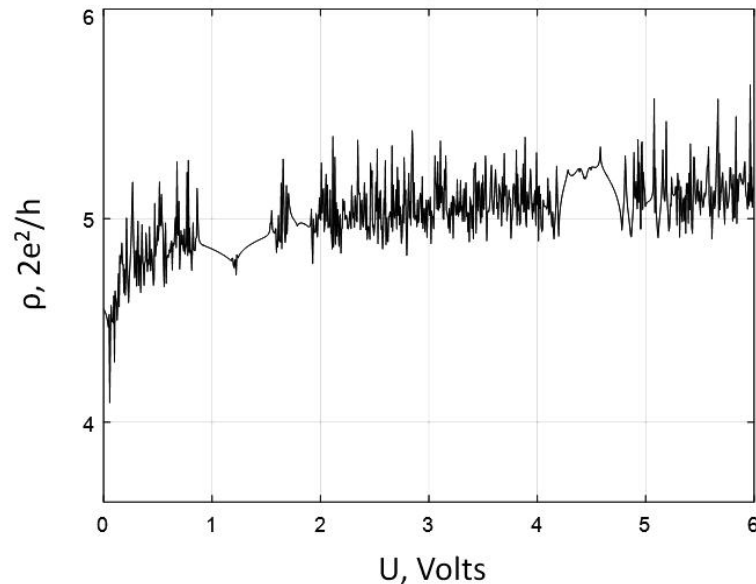


Fig. 2. Dependence of conductivity of quantum nanowire on external voltage.
 $V_0 = 1.12 \text{ V}$, $\gamma = 0.03$.

As an example, quantizing process of conductivity of an electron gas in a film AlGaAs / GaAs is schematically shown in Figure 3 [19]. The abscissa axis is the voltage in volts, the ordinate axis is conductivity in units of measurements of quantum conductivity $2e^2/h$. Here e is elementary charge, h is the Planck constant. Such dependence is typical for semiconductor film with different nanocluster structure and chemical composition.

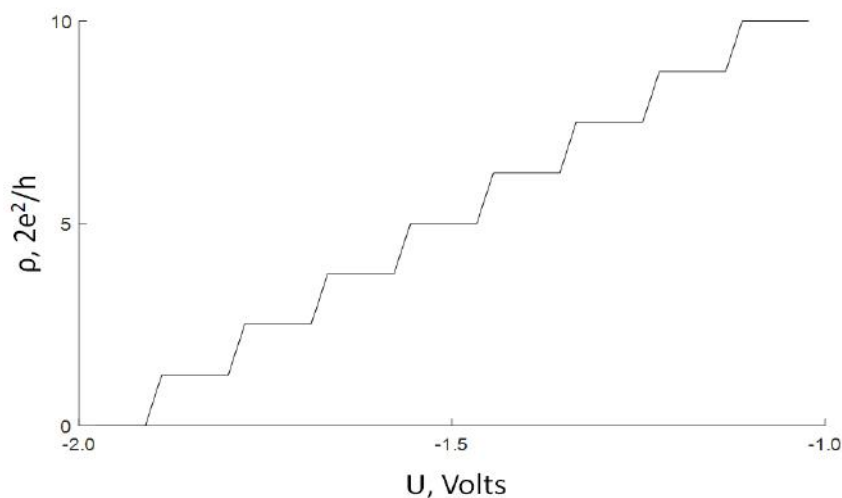


Fig. 3. Quantization of electron gas conductivity in semiconductors

Quantization of conductivity has been observed in a big amount of experimental research works. This effect is typical not only for semiconductor thin films, but also for metals and carbon nanotubes with different configurations [11-15]. Stepwise nature of the dependence of conductivity on external voltage is observed not only at low temperatures about several kelvins, but at room temperatures also.

Thus, it can be noted that formulas (1)-(3) correctly describe the basic regularities of electrical conductivity of quantum nanowires.

Conclusion

In this paper we have presented a new approach for the description of regularities of electrical conductivity of semiconductor films containing quantum-sized structures. We have taken into account scale invariant, hierarchically self-similar fractal structure of these films. By use of the equations suggested in the present paper we have described such features of current-voltage characteristics of nanostructured semiconductor films as their oscillating behavior, clustering of the oscillations because of quantum effects in the considered systems, existence of areas with negative differential resistance related with multi-barrier tunneling effects. Theoretical results obtained in this paper qualitatively agree with corresponding experimental data [8-15] on study of electrical properties of nanostructured semiconductors.

Results of the present work can be used for development of nanoelectronic devices and improvement of their parameters.

ACKNOWLEDGEMENTS

This paper is supported by Ministry of Education and Science of the Kazakhstan Republic (Grant number is AP05132854).

REFERENCES

- 1 Gonchar K.A., Osminkina L.A., Galkin R.A., Gongalsky M.B., Marshov V.S., Timoshenko V.Yu., Kulmas M.N., Solovyev V.V., Kudryavtsev A.A., Sivakov V.A.. Growth, Structure and Optical Properties of Silicon Nanowires Formed by Metal-Assisted Chemical Etching. *Journal of Nanoelectronics and Optoelectronics*. 2012, Vol. 7, No 6, pp. 602-606.
- 2 Bunkov K.V., Golovan L.A., Gonchar K.A., Timoshenko V.Yu., Kashkarov P.K., Kulmas M., Sivakov V. Dependence of Raman scattering efficiency in silicon nanowire arrays on excitation wavelength. *Semiconductors*. 2013, Vol. 47, No 3, pp. 354-357.
- 3 Artoni P., Irrera A., Iacona F., Pecora E.F., Franzò G., Priolo F. Temperature dependence and aging effects on silicon nanowires photoluminescence. *Optics Express*. 2012, Vol. 20, No. 2, pp. 1483-1490.
- 4 Zhanabaev Z.Zh., Grevtseva T.Yu., Danegulova T.B., Assanov G.S. Optical Processes in Nanostructured Semiconductors. *Journal of Computational and Theoretical Nanoscience*. 2013, Vol. 10, No 3, pp. 673-678.
- 5 Zhanabaev Z.Zh., Grevtseva T.Yu. Physical Fractal Phenomena in Nanostructured Semiconductors. *Reviews in Theoretical Science*. 2014, Vol. 2, No 3, pp. 211-259.
- 6 Zhanabaev Z.Zh., Grevtseva T.Yu., Ibraimov M.K. Morphology and Electrical Properties of Silicon Films with Vertical Nanowires. *Journal of Computational and Theoretical Nanoscience*. 2016, Vol. 13, pp. 615-618.
- 7 Zhanabaev Z.Zh., Timoshenko V.Yu., Turmukhambetov A.Zh., Grevtseva T.Yu., Assilbayeva R.B. Structure of porous silicon films. *Eurasian Physical Technical Journal*. 2017, Vol. 14, No 1(27), pp. 30-33.
- 8 Landauer R. Spatial variation of currents and fields due to localized scatterers in metallic conduction. *IBM Journal*. 1957, No 6, pp. 223-231.
- 9 Nutku F., Donmez O., Cokduygular E., Sarcan F., Kuruoglu F., Mutlu S., Yildirim S., Erol A. Effect of thermal annealing and nitrogen composition on quantum transport in GaInNAs alloy based modulation doped quantum well structures. *Journal of Alloys and Compounds*. 2017, Vol. 695, pp. 404-409.

- 10 Lancaster T., Pexton M. Reduction and emergence in the fractional quantum Hall state. *Studies in History and Philosophy of Modern Physics*. 2015, Vol. 52, pp. 343-357.
- 11 Peng X., Yang Y., Hou Y., Travaglini H.C., Hellwig L., Hihath S., K. van Benthem, Lee K., Liu W., Yu D. Efficient and Hysteresis-Free Field Effect Modulation of Ambipolarly Doped Vanadium Dioxide Nanowires. *Physical Review Applied*. 2016, Vol. 5, pp.1-9.
- 12 Alexander-Webber J.A., Groschner C.K., Sagade A.A., Tainter G., Gonzalez-Zalba M.F., R. Di Pietro, Wong-Leung J., Tan H.H., Jagadish Ch., Hofmann S., Joyce H.J. Engineering the Photoresponse of InAs Nanowires. *Applied Materials & interfaces*. 2017, Vol. 9, pp. 43993-44000.
- 13 Rajeev K.P., Opoku C., Stolojan V., Constantinou M., Shkunov M. Effect of Nanowire-dielectric Interface on the Hysteresis of Solution Processed Silicon Nanowire FETs. *Nanoscience and Nanoengineering*. 2017, Vol. 5, No 2, pp. 17-24.
- 14 Abay S., Persson D., Nilsson H., Wu F., Xu H.Q., Fogelstrom M., Shumeiko V., Delsing P. Charge transport in InAs nanowire Josephson junctions. *Physical Review B*. 2014, Vol. 89, pp. 1-11.
- 15 Yu G.-F., Yu M., Pan W., Han W.-P., Yan X., Zhang J.-Ch., Zhang H.-D., Long Y.-Z. Electrical Transport Properties of an Isolated CdS Microrope Composed of Twisted Nanowires. *Nanoscale Research Letters*. 2015, Vol. 1, pp.1-7.
- 16 Martínez L., Ocampo O., Kumar Y., Agarwal V. ZnO-porous silicon nanocomposite for possible memristive device fabrication. *Nanoscale Research Letters*. 2014, Vol. 9, No 437, pp. 1- 6.
- 17 Yaseen Z.A., Yiseen G.A. Morphology of Porous Silicon Nanostructures in p-type Silicon Based on Novel Comparison between Two Electrochemical Cells Design. *International Journal of Electrochemical Science*. 2016, Vol. 11, pp. 2473-2485.
- 18 Ibraimov M.K., Sagidolda Y., Rummyantsev S.L., Zhanabaev Z.Zh., and Shur M.S. Selective Gas Sensor Using Porous Silicon. *Sensor Letters*. 2016, Vol. 14, No 6, pp. 588-591.
- 19 Kruglyak Yu.A. From ballistic conductivity to diffusion in the Landauer-Datt-Lundstrom transport model. *Nanosystems, Nanomaterials, Nanotechnologies*. 2013, Vol. 11, No. 4, pp. 655-677. [in Russian]

UDC: 532.783:541.1:539.21:535.37

THE INFLUENCE OF VARIOUS EFFECTS ON THE ORDERING OF LIQUID CRYSTALS LOCATED ON NANORIBBON GRAPHENE

Agelmenev M.E.¹, Bratukhin S.M.², Polikarpov V.V.²

¹Karaganda State University named of academician E.A.Buketov, Karaganda, Republic of Kazakhstan, amaxut58@gmail.com

²Central Kazakhstan Academy, Karaganda, Republic of Kazakhstan

Experiments on computer simulations of the behavior of polar nematic phenylpropargyl ethers of parachlorophylenes on the surface of graphene made it possible to reveal a number of regularities. The dynamics of molecules under the action of an electric field and temperature was investigated. As a method of investigation, the molecular dynamics method was used in the approximation of the liquid aggregate state. The simulation was carried out in an atomistic approach. A small effect of graphene type on the behavior of nematic liquid crystals (NLC) is shown. It should be noted that the NLC is highly ordered in the case of coincidence of the field directions and the flow of the NLC. It is found that with increasing electric field strength the ordering of the cluster grows nonlinearly. And the greatest growth is observed in the field of enlightenment. This allows us to assert that the primary role of graphene and the electric field is the self-organization of the NLC in the region of an isotropic liquid..

Keywords: nematicliquid crystals, graphene, computer modeling

Introduction

Graphene has a great interest due to its electrical and thermoelectric properties. This allows us to obtain new nanocomposite materials [1-9] and to improve the performance of electronic devices [10-15] with graphene. These studies on changes in the electronic states of metal ions [1-2], photoelectrochemical response [3], absorption processes [4], the nature of the interaction [5], electrical [6-7] and temperature conductivity [8], phase transition temperatures [9] show the crucial role of graphene. The high mobility of the current carriers makes its use attractive as an electrode [10-11] in various devices [12], such as solar cells [13-14], lithium battery [15]. It is clear that for an effective use of graphene in devices there is need of understanding of the processes occurring in composite materials with graphene at the temperature and other influences.

The physical and chemical properties of the components definitely have significant effect on it. The widely used in electronics the liquid crystals are one of these materials by Wahle et al. [16]. As noted Divariet al. in [17], the ratio between length and width of the graphene has large impact on these properties. The founded effect of the flow of nematic liquid crystals (NLC) in [18] on the graphene surface at the temperature change had been experimentally confirmed [19].

Therefore, the understanding of influence of graphene size and its type on the properties located on the surface of such electronic products as the NLC must be considered when creating optoelectronic devices based on these compounds. In this regard, the aim of this study was to research the influence of the size and type of graphene, the effects of temperature and electric field on the dynamics of nematic liquid crystals based on the arylpropargyl ethers of phenols.

1. The methodology of the analysis

As a sample the nematic liquid crystal - phenylpropargyl ether of p-chlorphenol (PEC) [20], located on the graphene in a planar orientation was used. For the modeling of the behavior of these compounds we used the method of molecular dynamics based on the program GROMACS [21] version 3.3.1 approaching liquid state [22-24].

In the modeling the NPT ensemble is used, the modeling time at a given temperature was 10 ps. The radius of the cutoff of the Coulomb interaction and the dispersion was 2 nm. The successive annealing was carried out in the heating mode.

The input file for cluster formation was created, which took into account the distance between the molecules, in rows and layers of the cluster in the direction of XYZ. The grapheme sizes were varied by direction (OX), perpendicular to the director (OY). At the same time the sizes of the cluster and other side of graphene (OY) were unchanged. The direction of the electric field was set on the direction of the director.

The studies were carried out in the presence of the electric field parallel to the director. The sizes of the grapheme that were used in the modeling varied, with a ration of width (X) to the length (Y) - 1:1 (115Å: 115Å), 2:1 (230Å: 116Å), 3:1 (345Å: 116Å), 3,5 1 (401Å: 116Å).

In the study of the influence of some parameters the number of molecules of PEC was unchanged and they were oriented planar respectively to the graphene’s plane. The structure of the graphene was chosen in the form of zigzag (Z) and armchair (A) [25]. The method of preparing and analysis of modeling results is presented in [22, 26].

2. Results and discussion

3.1 The effect of the grapheme type on the dynamic behavior of the NLC

In the first part of the studies of the influence of the grapheme type on the behavior of nematic liquid crystals for different directions of the electric field vector of $1 \times 10^7 \text{V/m}$ (along the x, y, z) were carried out. The cluster size was $14 \times 14 \times 3$ molecules, the ratio of width to length of the grapheme was close to 1:2 for armchair and zigzag structures (112Å: 235Å) with a length of 1.4210Å. The results of these studies are shown in Fig.1-3.

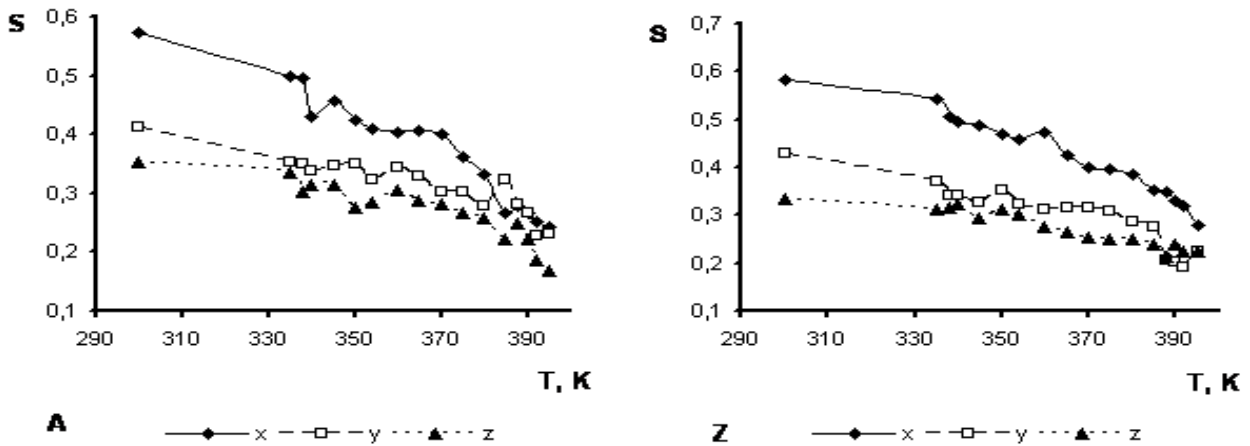


Fig.1. Temperature dependences of the degree of ordering of PEC at different orientations of the electric field (x, y, z) in case of graphene zigzag (Z) and armchair (A) structures

As seen in Figure 1, the type of graphene does not significantly affect to the nature of the curves $S(T)$. In the area of disintegration of dimers (354-360K) [26] there is an excessive bend, after which there is a slight rise (Fig. 1). The higher values of the degree of ordering in the direction of X are largely due to the flow of the NLC in this direction.

The temperature dependences of information entropy (Fig. 2) are consistent with $S(T)$ curves.

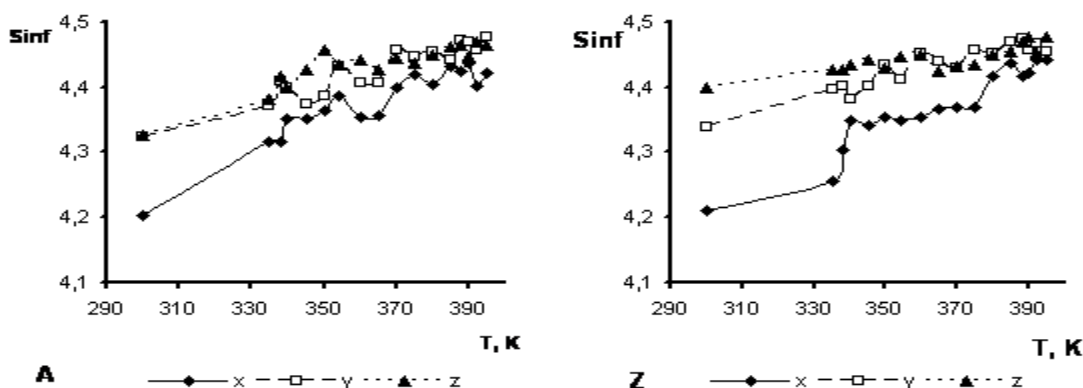


Fig.2. Temperature dependences of information entropy of the cluster with PEC at different orientations of the electric field in case of graphene zigzag (Z) and armchair (A) structures

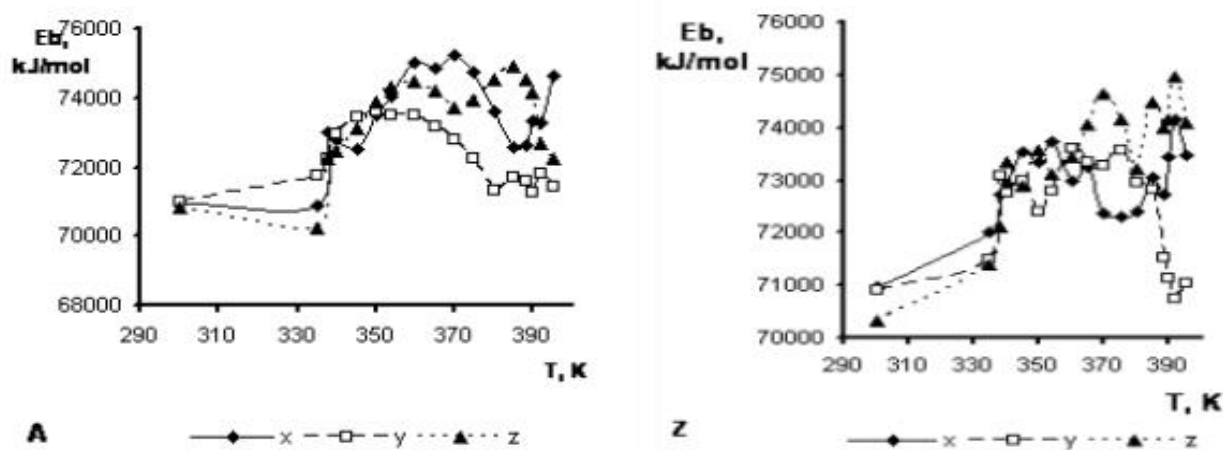


Fig.3. Temperature dependences of bond energy of the cluster with PEC at different orientations of the electric field in case of graphene zigzag (Z) and armchair (A) structures

As seen in Figure 3, there is some rise of bond energy in case of direction Z and X. The bond energy of the area of mesophase increases rapidly from the moment of melting. The minimum values of bond energy are observed at the orientation of the field along Y.

Thus, the small effect of the graphene type on the behavior of the NLC can be stated when the field direction coincides with the direction of flow the higher degree of order should be noted.

3.2 The effect of the electric field on the dynamics of the NLC

For this study the cluster of the NLC with size of $14 \times 7 \times 6$ molecules with the ratio of width to length 3:1 (345 \AA : 116 \AA), and the direction of the electric field along the OY axis, coinciding with the direction of the director was used. The magnitude of the electric voltage had the following values: $1 \times 10^7 \text{ V/m}$ (1), $2 \times 10^7 \text{ V/m}$ (2), $3 \times 10^7 \text{ V/m}$ (3), $4 \times 10^7 \text{ V/m}$ (4), $5 \times 10^7 \text{ V/m}$ (5). The graphene had the structure of armchair.

The research results are presented in Fig.4-12. As seen in Figure 4, the ordering in the Y direction after some decrease, which is until the temperature of decomposition of the dimers (354 K), further is increasing as the temperature begins to rise.

The nonlinear dependence on the magnitude of intensity occurs mainly in the area of decline, in the enlightenment area values are close to each other. The similar character of changes observed for the ordering in the direction of the X axis. The difference is that the decrease and growth of the Y axis corresponds to the growth and decay of X, respectively. One of the explanations may be a flow, at which the molecules begin to move along the X axis.

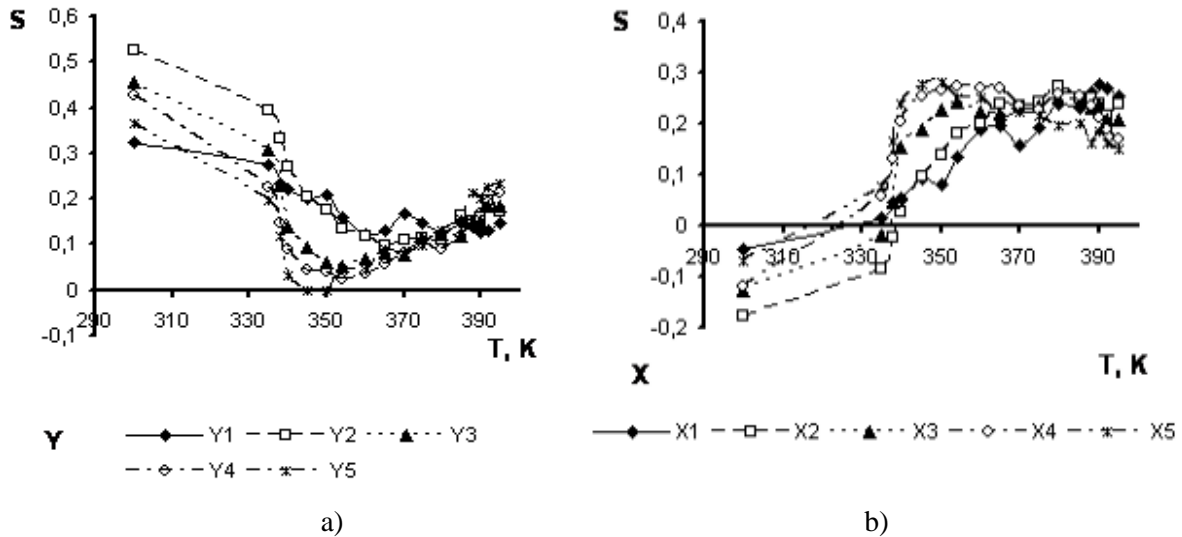


Fig.4. Temperature dependences of ordering degree of the PEC along Y (a) and X (b) directions at different values of the electric field

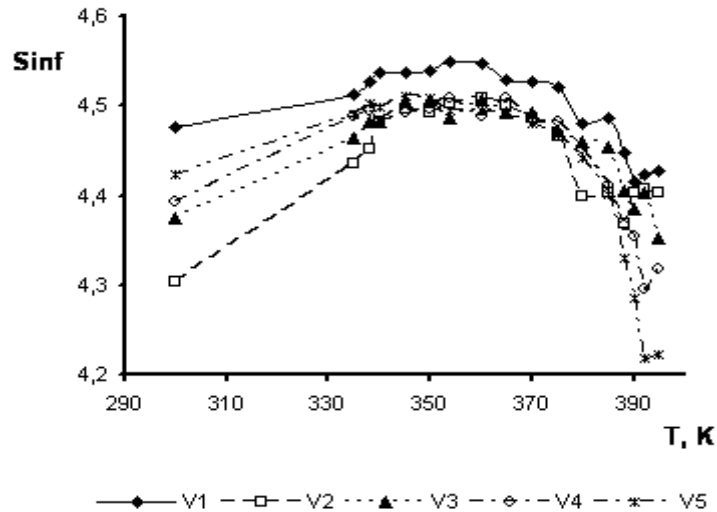


Fig.5. Temperature dependences of the information entropy of PEC at different values of electric field

The curves of the information entropy (Fig. 5) confirm this pattern. In this case it is clear that increasing the size of the fields' intensity leads to increase of ordering. For larger fields (V4, V5) the ordering in the area of enlightenment is considerably higher than the ordering in the initial state (300 K) and this trend is typical of other field values. This is may be due to both the orienting influence of graphene, and the effect of crystallization under normal substrates [27]. It should be noted that the difference in the values of entropy between the initial state and the area of enlightenment is much higher in this case as compared to [27]. It can be argued that this is due to the presence of the graphene as a substrate.

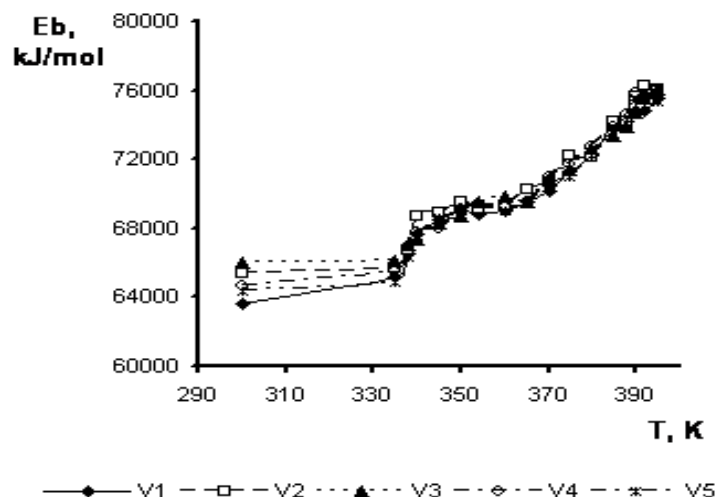


Fig.6. Temperature dependences of the bond energy of clusters' molecules at different values of the electric field

The bond energy for all values of intensity changes the same way, with a characteristic inflection in the area of disintegration of dimers (Fig. 6). The growth of the bond energy with increasing temperature indicates the predominance of processes of ordering over chaotic processes due to thermal motion. The similar values of the bond energy for all values of the field intensity, apparently, can be related to the determining role of the graphene. The free flowing of the molecules on the surface of graphene, and self-organization of polar molecules under the electric field contributes to this fact.

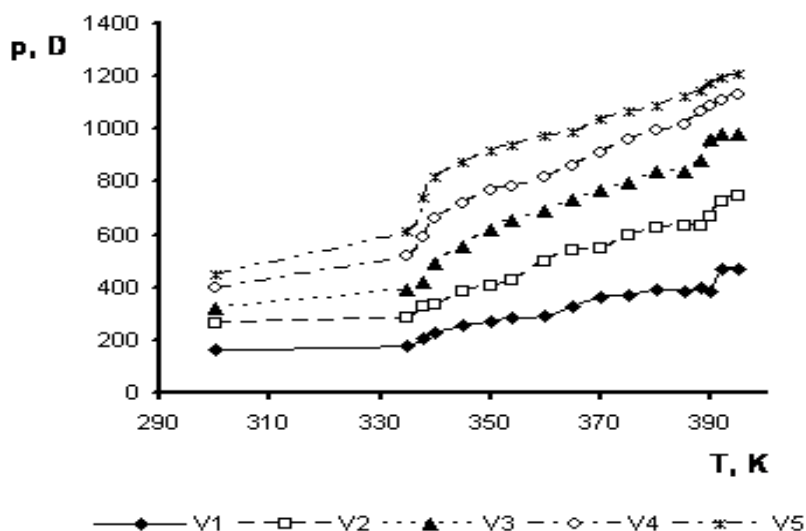


Fig.7. Temperature dependences of the total dipole moment of cluster's molecules at different values of the electric field

The discussed above the curves of temperature dependences of the degree of ordering, the information entropy and the total dipole moment cluster also comply with it (Fig. 7).

As seen in Figure 7, with increasing of field the total value of the dipole moment of the molecules in the cluster also increases. This behavior may be associated with sensitivity of the electric field to the influence of the PEC polar molecule and with the polarizability of the molecules with increasing of field intensity.

It is not difficult to see from Fig. 8-12 that increased intensity leads to the significant reversal of the cluster in the plane of graphene in the melting area (338 K). In the area of the mesophase (354 K) there is a noticeable movement of individual molecules on the surface of graphene. At the point of enlightenment (390 K) the molecules of cluster are distributed over its surface, flowing over the edge.

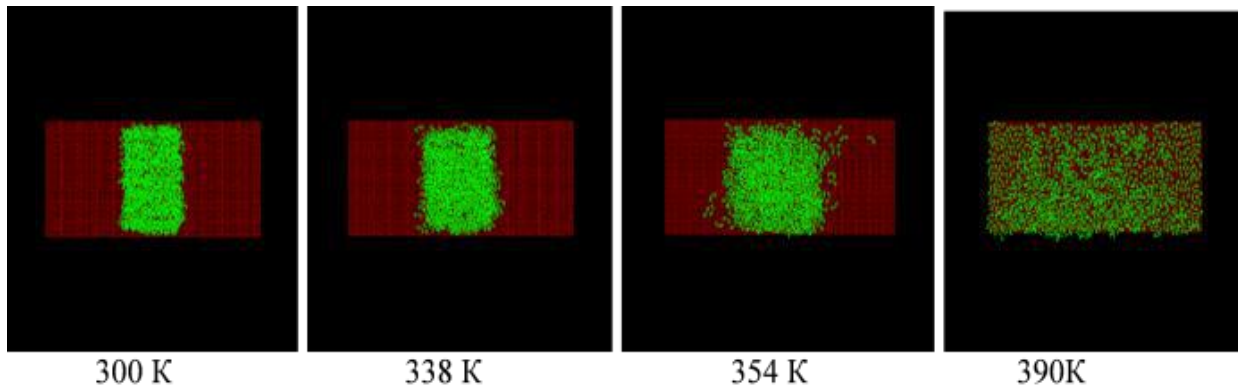


Fig.8. Cluster's view in the XOY plane at the value of electric field of $1 \times 10^7 \text{V/m}$

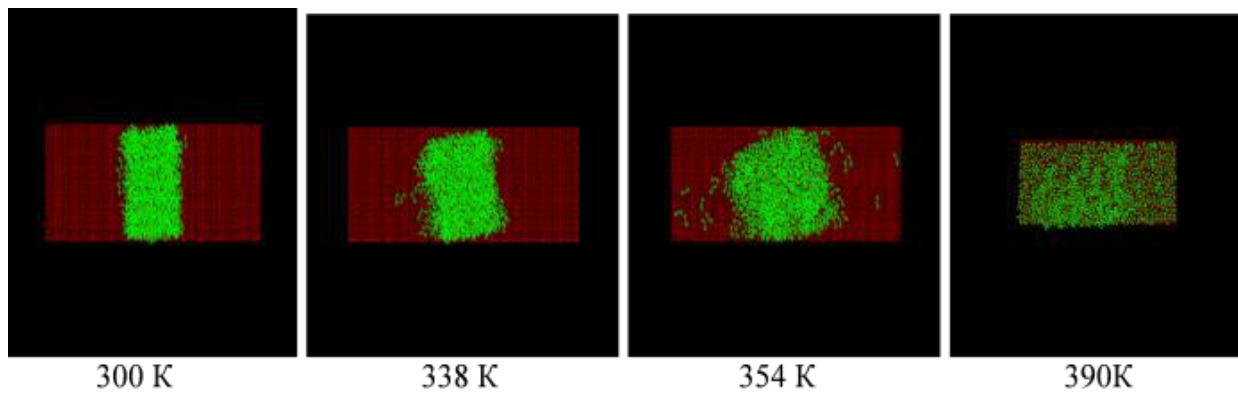


Fig.9. Cluster's view in the XOY plane at the value of electric field of $2 \times 10^7 \text{V/m}$

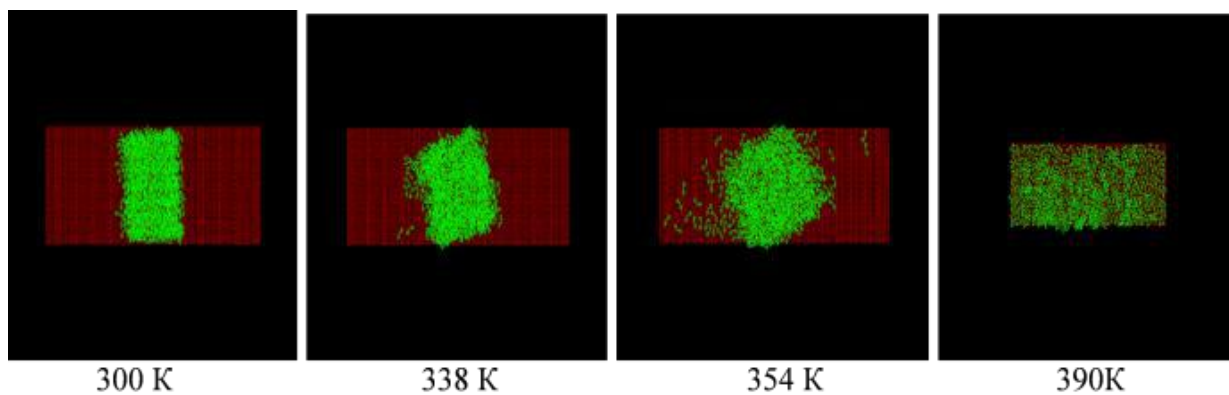


Fig.10. Cluster's view in the XOY plane at the value of electric field of $3 \times 10^7 \text{V/m}$

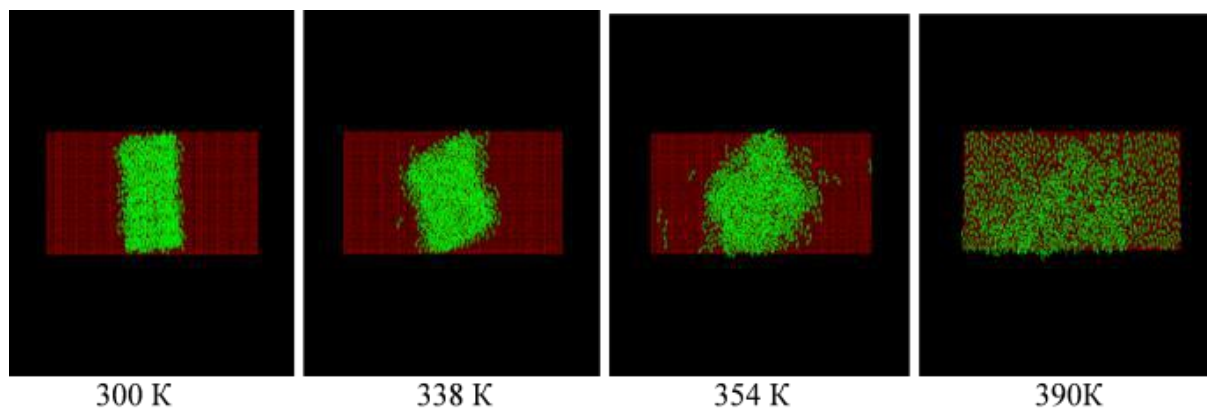


Fig.11. Cluster's view in the XOY plane at the value of electric field of $4 \times 10^7 \text{V/m}$

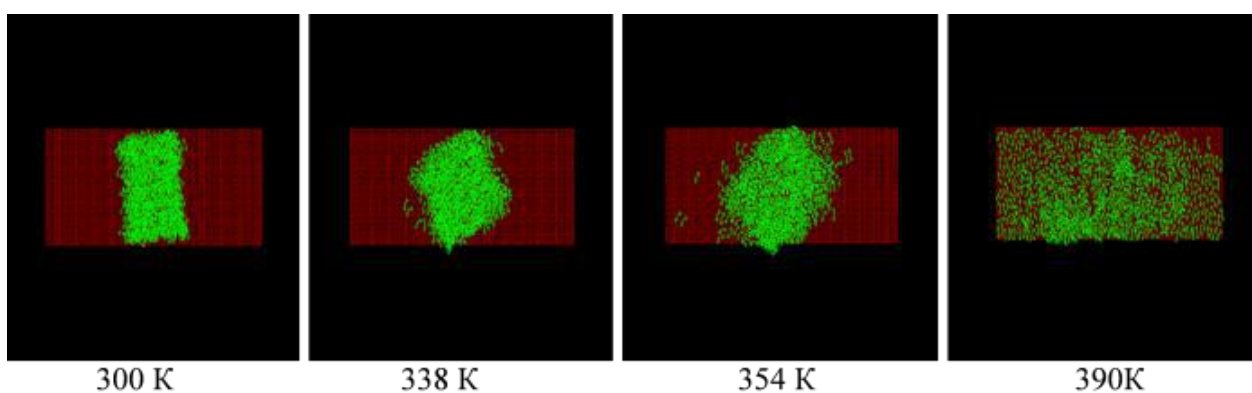


Fig.12. Cluster's view in the XOY plane at the value of electric field of $5 \times 10^7 \text{V/m}$

Thus, on the basis of the performed studies it was shown, that with increasing of the electric field intensity the ordering of clusters increases nonlinear. The greatest increase was in the area of enlightenment. Based on this fact it can be stated that graphene and electric field take a dominant role on the self-organization of the NLC in the area of the isotropic liquid.

Conclusion

The performed experiments on computer modeling of the behavior of the polar PEC, located on the surface of graphene, allowed identifying a number of laws. The little effect of the graphene type on the behavior of the NLC was shown. It was established that the ordering of nematic liquid crystals increase non-linear with increasing of the electric field. The determining role of graphene and the electric field on self-organization of the NLC in the enlightenment region was shown.

It was found that in the area of enlightenment the ordering of the NLC starts to grow when the value of the ratio of width to length is 3: 1. This allows stating that at least two processes are taking place under the influence of temperature and electric field: First - "flow" of the molecules in the direction of X, the second - the rotation of the molecule in the direction of this axis. The second process may be due to the reorientation relative to the electric field of the molecules.

REFERENCES

- 1 Kawabata H., Iyama T., Tachikawa H. Interaction of Lithium Ion (Li^+) with Chlorinated Graphene (Cl-Graphene) Surface: A Direct Ab-Initio MD Study. *Mol. Cryst. Liq. Cryst.* 2009; Vol. 504(1), pp.147-154.
- 2 Abe S., Watari F., Takada T., Tachikawa H. A DFT and MD Study on the Interaction of Carbon Nano-Materials with Metal Ions. *Mol. Cryst. Liq. Cryst.* 2009, Vol. 505(1), pp. 51 – 58.

- 3 Jung S.W., Park J-H., Seo S-W., Kim J-H., Choi C-J., Kim H., et al. Enhanced Photo electrochemical Response of Graphene-Coated Al₂O₃-TiO₂ Nanocomposite Photoanodes. *Mol. Cryst. Liq. Cryst.* 2011, Vol. 538 (1), pp. 272 – 277.
- 4 Liu W., Zhao Y.H., Nguyen J., Li Y., Jiang Q., Lavernia E.J. Electric field induced reversible switch in hydrogen storage based on single-layer and bilayer graphenes. *Carbon.* 2009, Vol. 47(15), pp. 3452-3460.
- 5 Fugetsu B., Sano E., Yu H., Mori K., Tanaka T. Graphene oxide as dyestuffs for the creation of electrically conductive fabrics. *Carbon.* 2010, Vol. 48(15), pp. 3340-3345.
- 6 Fan Y., Wang L., Li J., Li J., Sun S., Chen F., et al. Preparation and electrical properties of graphene nanosheet /Al₂O₃ composites. *Carbon.* 2010, Vol. 48 (6), pp. 1743-1749.
- 7 Ramana G.V., Padya B., Srikanth V.S., Jain P.K., Padmanabham G. Electrically conductive carbon nanopipe-graphite nanosheet /polyaniline composites. *Carbon.* 2011, Vol. 49(15), pp.5239-5245.
- 8 Wei Z., Ni Z., Bi K, Chen M, Chen Y. In-plane lattice thermal conductivities of multilayer graphene films. *Carbon.* 2011, Vol. 49(8), pp. 653-2658.
- 9 Vadukumpully S., Paul J., Mahanta N., Valiyaveetil S. Flexible conductive grapheme /poly(vinyl chloride) composite thin films with high mechanical strength and thermal stability. *Carbon.* 2011, Vol.49(1), pp. 198-205.
- 10 Blake P., Brimicombe P.D., Nair R.R., Booth T.J., Jiang D., Schedin F., et al. Graphene-based liquid crystal device. *Nano Lett.* 2008, Vol. 8(6), pp. 1704 – 1708.
- 11 Nordendorf G., Kasdorf O., Kitzerow H-S., Liang Y., Feng X., et al. Liquid Crystal Addressing by Graphene Electrodes Made from Graphene Oxide. *Jpn. J. Appl. Phys.* 2010; Vol. 49(10), pp. 100206.
- 12 Basua J., Basub J.K., Bhattacharyya T.K. The evolution of graphene-based electronic devices. *Intern. J. Smart and Nano Mater.* 2010, Vol. 1(1), pp. 201–223.
- 13 Li Z., Zheng L., Saini V., Bourdo S., Dervishi E., Biris A.S. Solar cells with graphene and carbon nanotubes on silicon. *J. Exper. Nanoscience* 2012; Vol. 1(1), pp. 1 – 8.
- 14 Park J-H., Seo S-W., Kim J-H., Choi C-J., Kim H., Lee D.K., et al. Improved Efficiency of Dye-Sensitized Solar Cell Using Graphene-Coated Al₂O₃-TiO₂ Nanocomposite Photoanode. *Mol. Cryst. Liq. Cryst.* 2011, Vol. 538 (1), pp. 285-291.
- 15 Xiang H., Zhang K., Ji G., Lee J.Y., Zou C., Chen X., et al. Graphene /nanosized silicon composites for lithium battery anodes with improved cycling stability. *Carbon*, 2011, Vol. 49(2), pp. 1787-1796.
- 16 Wahle M, Kasdorf O, Kitzerow H-S, Liang Y, Feng X, Müllen K. Electrooptic Switching in Graphene-Based Liquid Crystal Cells. *Mol. Cryst. Liq. Cryst.* 2011; Vol. 543(1), pp. 187–193.
- 17 Divari P.C., Kliros G.S. Modeling the thermopower of ballistic graphene ribbons. *Physica E.* 2010, Vol. 42(9), pp. 2431–2435.
- 18 Agelmenev M.E., Muldakhmetov Z.M., Bratukhin S.M., Polikarpov V.V. The Influence of the Nano Substrate on the Nematic Liquid Crystals Behaviour. *Mol. Cryst. Liq. Cryst.* 2011, Vol. 545(1), pp. 36-43.
- 19 Yu J-S, Kim SJ, Kim J-H. Effect of graphene layers on the alignment of nematic liquid crystal. *Proceeding of the 23rd Intern. Liq. Cryst. Confer.* Krakow, Poland, 2010, pp. 223.
- 20 Agelmenev M.E., Bazhikov K.T., Muldakhmetov Z.M., Sizykh M.Yu. Effect of the Nature of Halogen on the Acetylene Compounds. *Rus. J. Phys. Chem.* 2002, Vol. 76(10), pp. 1713 – 1714.
- 21 Van der Spoel D., Lindahl E., Hess B., van Buuren A.R., Apol E., Meulenhoff P.J., et al. GROMACS User Manual version 3.3.1 , www.GROMACS.org
- 22 Agelmenev M.E., Muldakhmetov Z.M., Bratukhin S.M., Pak V.G., Polikarpov V., Yakovleva O.A. The dynamics of some nematic liquid crystals. *Mol. Cryst. Liq. Cryst.* 2008, Vol. 494, pp. 339–352.
- 23 Agelmenev M.E., Bratukhin S.M., Muldakhmetov Z.M., Polikarpov V.V. Mesogenic System Simulation in the Liquid State of Aggregation. *Rus. J. Phys. Chem. A.* 2010, Vol. 84(7), pp. 1158–1162.
- 24 Agelmenev M.E. The modeling with free boundary. *Mol. Cryst. Liq. Cryst.* 2011, Vol. 545(1), pp.190-203.
- 25 Choi W., Lahiri I., Seelaboyina R., Kang Y.S. Synthesis of Graphene and Its Applications: A Review. *Critic. Rev. in Solid State and Materials Sciences.* 2010, Vol. 35, pp. 2–71.
- 26 Agelmenev M.E., Muldakhmetov Z.M., Bratukhin S.M., Pak V.G., et al. Computer Simulations of the Behavior of Arylpropargyl Phenol Esters. *Rus. J. Phys. Chem. A.* 2008; Vol.82(5), pp. 784–788.
- 27 Agelmenev M.E., Muldakhmetov Z.M., Bratukhin S.M., Polikarpov V., Pak V.G. Effect of “crystallization” in clusters with molecules, consisting atoms of fluoride. *Izv. Nation. Acad. Scien. of the Kazakhstan, Chem.* 2009, Vol. 4, pp. 36-39.

UDC 538.97; 539.216.2; 539.23

SURFACE ENERGY AND THE TOLMAN CONSTANT OF HALOGENIDE OF ALKALI METALS

Guchenko S.A., Zavatskaya O.N., Yurov V.M., Kasymov S.S., Laurinas V.Ch.

E.A. Buketov Karaganda State University, Karaganda, Republic of Kazakhstan, exciton@list.ru

The article reviews the existing methods for determining the surface energy of solids. Each of the methods described is practically limited to either temperature or values that are experimentally determined with low accuracy. A method is proposed for determining the surface energy of a solid on the basis of the dimensional dependence of its physical properties (magnetic permeability, luminescence intensity, thermal conductivity, etc.). The surface energy of alkaline halides is determined. Its magnitude is much larger than the surface energy of pure metals. The critical radius of these compounds is calculated, starting with which the direct Hall-Petch effect is reversed.

Keywords: surface energy, size effect, luminescence, halides, alkali metals.

Introduction

Methods for determining the surface energy of solids began to be developed in the 20s of the last century [1, 2]. In the sixties of the last century, some results of research were presented [3, 4]. The following methods for determining the surface energy of solids were proposed [3, 4]:

1. The method of "zero creep".
2. Method of destruction (splitting) of crystals.
3. The "neutral drop" method.
4. Method of dissolving the powder
5. The method of stages of growth and evaporation.
6. The method of a conical sample.
7. Method of "healing scratch".

The idea of the "zero creep" method is as follows. At a high temperature under the influence of surface tension forces, the arbitrary shape of a solid body must be transformed in the direction of decreasing the total surface energy. Thus, in particular, a freely suspended sample of a thin wire or foil should be shortened in length. On the other hand, under the influence of externally applied force (F), the foil (or filament) can be elongated due to the viscous flow. Obviously, for a certain value of $F = F^*$, the surface tension forces will be compensated and the creep rate will vanish. An experimentally determined F^* can be a source of information on the magnitude of the surface tension. This method was used to determine the surface energy of pure metals at a temperature close to the melting point, when the mobility of the atoms becomes noticeable. For other materials, this method does not apply.

The most reliable version of the method of determination, based on cleavage of the crystal, was proposed in 1930 Obreimov [2]. The idea of this work is as follows. From the crystal along the cleavage plane, plastic is split off, which under the influence of the moment of forces acting against the forces of surface tension, partially bends. This plate can be used as a dynamometer measuring the splitting force. The method was applied in [3] (Gilman J.) for various crystals at a temperature of liquid nitrogen, when the heat arising from the splitting of the crystals can be neglected. The method is suitable for crystals having a cleavage plane.

The value of σ_s can be determined from the data on the equilibrium form of the liquid droplet of another substance (B), which is located on the surface of the solid (A) under study. The measurement scheme is clear from Fig. 1.

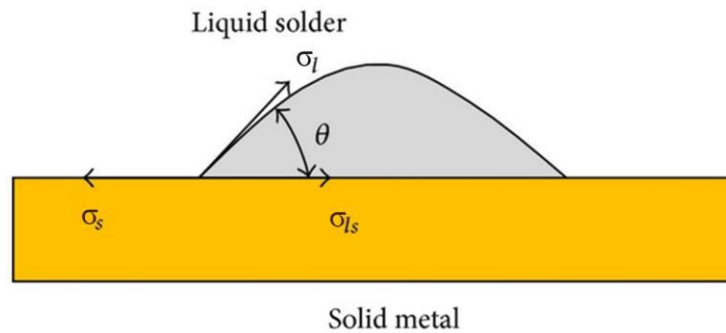


Fig.1. Diagram of the "neutral drop"

In the method for dissolving the powder, the value is found from the calorimetric determination of the dissolution heat difference of the dispersed powder and a massive crystal of the same mass ($\sigma_s = q_r - q_0/S$). The source of the significant error in the method described is the inaccuracy in the determination of the total surface of the powders. The generally accepted assumptions that the shape of the powder are spherical and all the powders are the same can lead to large errors.

To determine the amount of surface energy in the method of growth and evaporation stages, one uses the fact that on the growth surface there are often observed retarded "resting" steps whose curvature is such that the equilibrium vapor pressure near the step surface coincides with the vapor pressure in the space surrounding the crystal. The accuracy of the method is small.

Directly in the method of a conical sample, not the surface energy but the quantity (interfacial surface tension at the liquid-solid interface) is determined at the melting temperature [4]. The method is rarely used. It is known that in the case of high-temperature annealing of a crystal under equilibrium conditions, on the surface of which a scratch is applied, the latter is smoothed out. For metals, the kinetics of smoothing is determined by the mechanism of surface diffusion. This is the basis of the method of "healing scratch" [4].

As follows from the review [1-4] of experimental methods for determining the surface energy of solids, each of the methods described is practically limited to either temperature or values that are experimentally determined with low accuracy.

At present, various modifications of the "neutral drop" method have become most widespread. This method is based on Young's equation [5], which leads to the concept of the contact angle θ (Fig. 1). There are two models for describing the contact angle on a real surface. The Wenzel model and the Cassie-Baxter model. Unlike an ideal surface, a real surface can have a chemical heterogeneity and surface roughness. The Wenzel model considers a rough surface, but with chemical homogeneity [6]. The Cassie-Baxter model considers a plane surface, but with a chemical inhomogeneity [7]. These models have been widely used to the present time. However, today they have been seriously criticized [8]. More complex models of the contact angle have been developed [9-13].

In [13], the Young equation, the Wenzel equation, and the Cassie-Baxter equation were obtained from the thermodynamic point of view. From the conclusions, the behavior of the contact angle could be determined. In an ideal situation, the contact angle is determined by an infinitesimally small region near the contact line, and not by the inner surface inside the contact line. The angle of contact also does not depend on external factors that do not affect the surface energy. Thus, it is not influenced by pressure, droplet size, gravity, curvature of the substrate surface, rotation of the substrate and the presence of needles or defects. From the point of view of the hysteresis of the contact angle, it was explained why these equations are not correct for describing real common surfaces, although the Cassie-Baxter equation is widely used for a superhydrophobic surface. In addition, the limitations of the equations were discussed. It is

expected that this study will provide a deeper understanding of the correctness of the models of contact angles and the nature of the contact angle.

1. Experimental method

The foundations of the thermodynamics of curvilinear interfaces were laid by J. Gibbs [14]. Then R. Tolman and his followers reduced this problem to the account of the dimensional dependence of the surface tension. In 1949, R. Tolman derived the equation for the surface tension σ [15]

$$\sigma/\sigma_{\infty} = (1 + 2\delta/R_s)^{-1}, \quad (1)$$

Here σ_{∞} is the surface tension for a plane surface; R_s is the radius of the tension surface; $\delta > 0$ is the distance between an equimolecular separating surface and a tension surface for a plane boundary. The order of magnitude of the parameter δ , called the Tolman length or the Tolman constant, should be comparable to the effective molecular diameter a . For $R \gg \delta$ Tolman's formula can be rewritten in the form:

$$\sigma/\sigma_{\infty} = 1 - 2\delta/R, \quad (2)$$

Subsequent studies did not change the content and form of the equation (2).

On the basis of quantum statistical thermodynamics we obtained the response function of the system W to the external action in the form [16]:

$$W/W_{\infty} = 1 - d/R \quad (3)$$

The parameter d is related to the surface tension σ by the formula:

$$d = \frac{2\sigma v}{RT} \quad (4)$$

Here σ is the surface tension of a massive sample; v is the volume of one mole; R is the gas constant; T -temperature.

Equations (3) and (4) were used by us to develop a method for determining the surface tension of solids [17]. The method was used to determine the surface tension of dielectric crystals KCl, with an admixture of thallium ions as a luminescent probe ($W=I$). The intensity of X-ray luminescence I was determined by the standard photoelectric method. The grain size of the dielectric was determined using a metallographic microscope. The results are shown in Fig. 2.

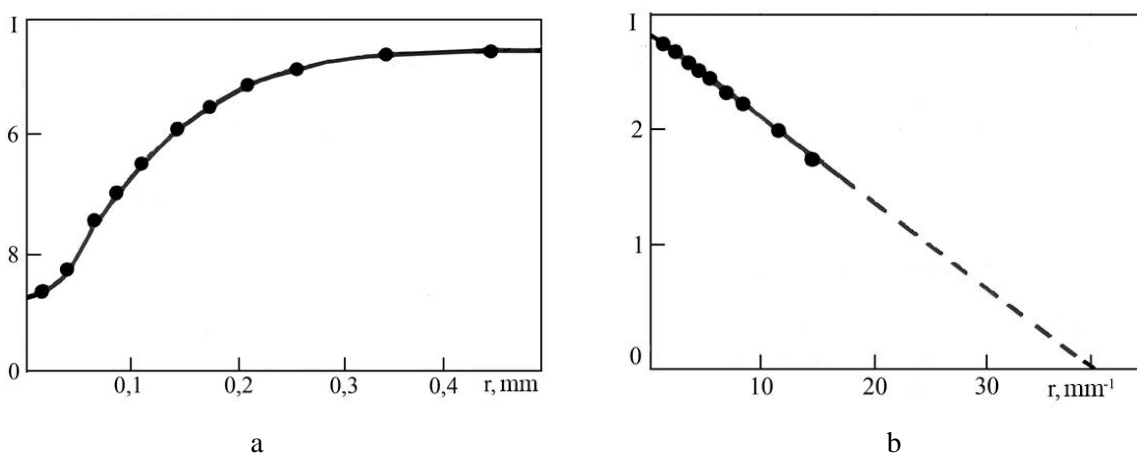


Fig. 2. Dependence of the intensity of X-ray luminescence KCl (a) on the size of the phosphor grain (b):

In the coordinates $I \sim 1/r$, the experimental curve is rectified in accordance with (3), giving a value of $d = 0.02 \mu\text{m}$. For KCl $v = 74.6 \text{ cm}^3/\text{mol}$ and from (4) for surface tension, we obtained: $\sigma = 0.730 \text{ J/m}^2$.

Note that as a function of the W response in equation (3), most physical properties that depend on the particle size or the film thickness (magnetic susceptibility, dielectric constant, thermal conductivity, etc. (can be used and determine the surface tension of a rigid body).

2. Results of the experiment and their discussion

The experimental results are shown in Fig. 3 and in Table 1.

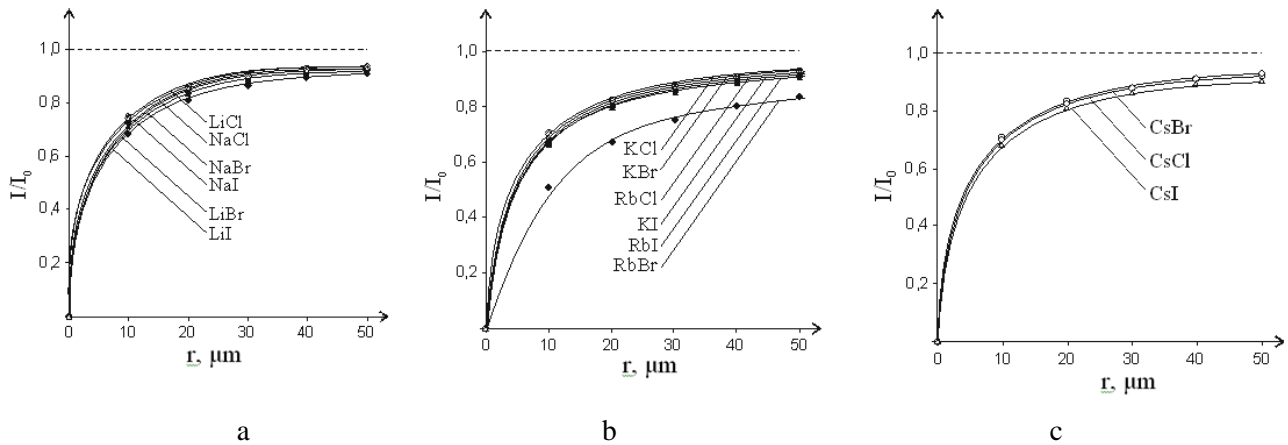


Fig.4. Surface tension of halogenide of alkali metals: a – Li, Na; b – R, Rb; c - Cs

Table 1. Surface tension and constant Tolman of alkali metal halides

| Metal | T_m, K | $\sigma_m, \text{J/m}^2$ | d, nm | $v, \text{g/mol}$ | δ, nm |
|-------|-----------------|--------------------------|----------------|-------------------|---------------------|
| LiCl | 878 | 0.615 | 20.9 | 42.4 | 10.5 |
| LiBr | 825 | 0.578 | 40.1 | 86.8 | 20.1 |
| LiI | 742 | 0.519 | 55.5 | 133.6 | 27.8 |
| NaCl | 1074 | 0.752 | 35.1 | 58.4 | 17.6 |
| NaBr | 1020 | 0.714 | 58.8 | 102.9 | 29.4 |
| NaI | 934 | 0.654 | 78.4 | 149.9 | 39.2 |
| KCl | 1043 | 0.730 | 43.6 | 74.6 | 21.8 |
| KBr | 1007 | 0.705 | 67.1 | 119.0 | 33.6 |
| KI | 954 | 0.668 | 88.7 | 166.0 | 44.4 |
| RbCl | 991 | 0.694 | 67.1 | 120.9 | 33.6 |
| RbBr | 954 | 0.668 | 88.4 | 165.4 | 44.2 |
| RbI | 920 | 0.644 | 109.4 | 212.4 | 54.7 |
| CsCl | 918 | 0.643 | 86.6 | 168.4 | 43.3 |
| CsBr | 909 | 0.636 | 108.3 | 212.8 | 54.2 |
| CsI | 894 | 0.626 | 130.1 | 259.8 | 65.1 |

For $h < d$, formula (3) loses its physical meaning ($A(h) \rightarrow \infty$), so we extend the function $A(h)$ in this region so that the function $A(h)$ vanishes at the point $h = 0$. This condition is satisfied when the function (3) is rewritten as:

$$A(r) = A_0 \cdot \left(1 - \frac{d}{d+h}\right) \quad (5)$$

The parameter d is naturally interpreted as the thickness of the surface layer (Fig. 4)

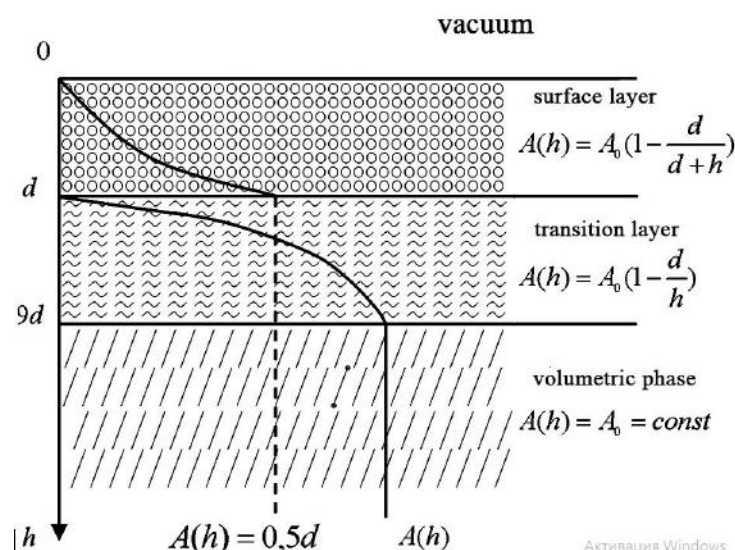


Fig.4. Schematic representation of the surface layer

Let us compare the parameter d for alkali metal halides with pure metals (Table 2).

Table 2. Parameter d of pure metals (M)

| M | d, nm |
|----|-------|----|-------|----|-------|----|-------|----|-------|----|-------|
| Li | 1.4 | Sr | 8.3 | Sn | 2.0 | Cd | 1.9 | Fe | 3.1 | Gd | 7.6 |
| Na | 2.1 | Ba | 8.9 | Pb | 2.6 | Hg | 0.8 | Co | 2.8 | Tb | 7.5 |
| K | 3.7 | Al | 2.2 | Se | 1.9 | Cr | 3.8 | Ni | 2.7 | Dy | 7.6 |
| Rb | 4.2 | Ga | 0.9 | Te | 3.5 | Mo | 6.5 | Ce | 5.4 | Ho | 7.8 |
| Cs | 5.2 | In | 1.6 | Cu | 2.3 | W | 8.4 | Pr | 6.0 | Er | 7.8 |
| Be | 1.8 | Tl | 2.4 | Ag | 3.1 | Mn | 2.8 | Nd | 6.4 | Tm | 7.4 |
| Mg | 3.1 | Si | 4.9 | Au | 3.3 | Tc | 5.1 | Sm | 6.3 | Yb | 6.5 |
| Ca | 7.0 | Ge | 4.0 | Zn | 1.5 | Re | 7.1 | Eu | 8.3 | Lu | 8.2 |

From Table 2 it is seen that the thickness of the surface layer of pure metals does not exceed 10 nm. This means that the surface layer of pure metal is a nanostructure. For halides of alkali metals, the thickness of the surface layer varies from 80 to 250 nm. This means that dimensional effects are observed even at $R \sim 10d \sim 2000$ nm. It should be noted that the Tolman constant $\delta = d/2$ has no physical meaning as the thickness of the monomolecular layer.

Experimental studies of the mechanical properties of nanomaterials and nanostructured coatings have shown that the tensile strength and hardness of many metals (Pd, Cu, Ag, Ni, etc.) are significantly higher than in the corresponding massive analogues. The increase in hardness and strength with decreasing grain size to a certain critical size is practically characteristic for all crystals. This follows from the well-known Hall-Petch equation that the yield stress σ_T depends inversely on the average grain size d [18, 19]:

$$\sigma_T = \sigma_M + kd^{-1/2}, \quad (6)$$

where σ_M is the ultimate strength of a single crystal, k is a certain dimensional coefficient.

Typically, the Hall-Petch relation (5) is satisfied for a significant part of the nanomaterials studied only up to a certain grain size, and at its lower values, reverse effects are observed: hardness (strength) decreases as the grain size decreases.

Despite the large number of works on the study of the influence of the size factor on the mechanical properties of nanostructures, the physical mechanisms of this influence remain the subject of ongoing discussions [20-25]. In [26] for the yield point we obtained the equation:

$$\sigma_T = \sigma_M + C\sigma d^{-1/2}. \quad (7)$$

Equation (7) coincides in form with the Hall-Petch equation (6). However, the proportionality coefficients in these formulas differ. In the case of equation (7), the behavior of the yield stress of small particles is also determined by the value of their surface tension σ .

For small d , A.I. Rusanov obtained an asymptotic linear dependence [27]:

$$\sigma = Kd. \quad (8)$$

Here K is the coefficient of proportionality. Formula (8) was obtained on the basis of thermodynamic considerations and should be applicable to small objects of a different nature. In this case, equation (7) takes the form:

$$\sigma_T = \sigma_M + CKd^{1/2}. \quad (9)$$

Equation (9) is the inverse Hall-Petch effect. It follows from equation (7) that the Hall-Petch equation begins to break from the moment when the dimensional dependence of the surface tension ($R < d$) begins to appear.

From Table 1 it can be seen that the strength of alkali metal halides is replaced by ductility at rather large d values. This affects many properties of these crystals.

Conclusion

The proposed method for determining the surface energy of a solid body with respect to the dimensional dependence of its physical property allows one to make a comparison with several methods. The implementation of each method does not cause any difficulties. This is illustrated by the calculation of the surface energy of alkali metal halides.

ACKNOWLEDGEMENTS

The work was carried out under the program of the Ministry of Education and Science of the Republic of Kazakhstan Grants No. 0118RK000063 and No. Φ . 0780.

REFERENCES

- 1 Tamman G., Tomke R. Die Abhangigkeit der Oberflachenspannung und die Wärme vor Glasse. *Z. anorg. Allgem. Chem.*, 1927. Bd. 162, pp. 1 – 24.
- 2 Obreimoff J.W. The splitting reigth of mica. *Proc. Roy. Soc.*, 1930, Vol. A127, pp. 290 – 293.
- 3 Gilman J. Direct Measurements of the surface energies of crystals. *J. Appl. Phys.*, 1960, Vol. 31, No.2, pp. 2208 – 2216.

- 4 Geguzin Ya.E., Ovcharenko N.N. Methods for the determination of the surface energy of solids. *Uspekhi Fizicheskikh Nauk*, 1962, V.76, No.2, pp. 283 – 305.
- 5 Young T. An essay on the cohesion of fluids. *Phil. Trans. R. Soc. Lond.* 1805, Vol. 95, pp. 65 – 87.
- 6 Wenzel R.N. Resistance of Solid Surfaces to Wetting by Water. *Industrial and Engineering Chemistry*, 1936, Vol. 28, pp. 988 – 994.
- 7 Cassie A.B.D., Baxter S. Wettability of Porous Surfaces. *Transactions of the Faraday Society*, 1944, Vol. 40, pp. 546 – 551.
- 8 Gao L., Carthy T.J. How Wenzel and Cassie were Wrong. *Langmuir*, 2007, Vol.23, pp. 3762 – 3765.
- 9 Subedi P.D. Contact Angle Measurement for the Surface Characterization of Solids. *The Himalayan Physics*. 2011, Vol. 11, pp. 1 – 4.
- 10 Zenkiewicz M. Methods for the calculation of surface free energy of solids. *Journal of Achievements in Materials and Manufacturing Engineering*, 2007, Vol. 24, No. 1, pp. 137 – 145.
- 11 Claeys M. *Determination of Surface Energy using different approaches*. Inst. Pharmazeutische Technologie und Biopharmazie, Dusseldorf, Germany, 2009, 55 p.
- 12 Erbil H.Y. The Debate on the Dependence of Apparent Contact Angles on Drop Contact Area or Three-Phase Contact Line: A Review. *Surface Science Reports*, 2014, Vol. 69, pp. 325 – 365.
- 13 Aliofkhaezrai M. (ed.) *Surface Energy*, 2015, 382 p. Available at <http://avxhome.se/blogs/exLib/>.
- 14 Gibbs J.W. Collected Works, *New Haven*: Yale University Press. 1948, Vol.1, pp. 33 – 54.
- 15 Tolman R.C. The effect of droplet size on surface tension. *J. Chem. Phys.*, 1949, Vol. 17, No.2, pp.333 – 337.
- 16 Yurov V.M. Superficial tension of pure metals. *Eurasian Physical Technical journal*, 2011, Vol. 8, No.1 (15), pp. 10 – 14.
- 17 Yurov V.M., Eshchanov A.N., Kuketayev A.T. *Method for measuring the surface tension of solids*. Patent of the Republic of Kazakhstan, No. 57691, Published on 15.12.2008, Bulletin No.12.
- 18 Hall E.O. The deformation and ageing of mild steel: III Discussion of results. *Proc. Phys. Soc.*, 1951, B 64, pp. 747 – 753.
- 19 Petch N.J. The cleavage strength of polycrystals. *J. Iron Steel Institute*, 1953, Vol. 174, pp. 25 – 28.
- 20 Saada G. Hall-Petch revisited. *Mat. Sci. Eng.*, 2005, A400-401, pp. 146 – 149.
- 21 Aghaie-Khafri M., Honarvar F., Zanganeh S. Characterisation of grain size and yield strength in AISI 301 stainless steel using ultrasonic attenuation measurements. *J. Nondestruct. Eval.*, 2012, Vol. 31, pp.191–196.
- 22 Armstrong R.W., Elban W.L. Hardness properties across multiscales of applied loads and material structures. *Mater. Sci. Technol.*, 2012, Vol. 28, pp. 1060 – 1071.
- 23 Antolovich S.D., Armstrong R.W. Plastic strain localization in metals: Origins and consequences. *Prog. Mater. Sci.*, 2014, Vol. 59, pp. 1–160.
- 24 Conrad H., Jung K. Effect of grain size from millimetres to nanometers on the flow stress and deformation kinetics of Ag. *Mater. Sci. Eng.*, 2005, A391, pp. 272 – 284.
- 25 Dunstan D.J., Bushby A.J., Grain size dependence of the strength of metals: The Hall–Petch effect does not scale as the inverse square root of grain size. *Int. J. Plasticity*, 2014, Vol. 53. – P. 56–65.
- 26 Yurov V.M., Laurinas V.C., Guchenko S.A. Some Problems of Strength Physics of Metal Nanostructures. *Physical and Chemical Aspects of Studying Clusters, Nanostructures and Nanomaterials*. Tver: Tver. state. Un-t, 2013, Issue. 5, pp. 408 – 412. [in Russian]
- 27 Rusanov A.I. *Phase equilibria and surface phenomena*. Leningrad, Chemistry, 1967, 346 p.

UDC 537.533.34

CALCULATION AND MODELING OF THE MOTION OF CHARGED PARTICLES IN THE QUADRUPOLE-CYLINDRICAL FIELD

Kambarova ZH.T.¹, Saulebekov A.O.²

¹ Ye.A. Buketov Karaganda State University, Universitetskaya Str.28, Karaganda, 100026, Kazakhstan

²Lomonosov Moscow State University, Kazakhstan branch, Kajimukana str. 11, Astana, 010010, Kazakhstan
kambarova@bk.ru

The electron-optical scheme of the electrostatic energy analyzer on the basis of the quadrupole-cylindrical field is proposed. The outer electrode of the proposed energy analyzer has a cone profile, the generatrix of which is a small angle of inclination with respect to the symmetry axis of the mirror, equal to 1.75 deg. Calculation of particle-optical parameters of the energy analyzer is carried out. Advantages of this field are shown. Initial parameters of the motion of charged particles, optimal from the point of view of the luminosity and resolution ability are given.

Keywords: energy analyzer, electrostatic field, quadrupole-cylindrical mirror, corpuscular-optical parameters, angular focusing.

Introduction

Many types of diagnostics of structures and composition of nanometer objects and nanosystems are based on an accurate analysis of energy spectrum of secondary electrons. A promising base for the required diagnostics is electron spectroscopy methods, which are characterized by a nanometer resolution in the solid depth. Energy analyzers with different geometries of fields are most often used for purposes of energy analysis.

Calculation of the structure of electrostatic quadrupole-cylindrical fields was calculated in [1]. Equipotential portraits of quadrupole-cylindrical fields with various contributions of the cylindrical field and the quadrupole are obtained. Results of the analysis of obtained equipotential portraits of quadrupole-cylindrical fields are presented.

Work [2] is devoted to the development of the mirror type energy analyzer based on the electrostatic quadrupole-cylindrical field. Focusing properties of the electron-optical scheme of the energy analyzer with “shaping parameter” $A = -0.05$ are determined. The regime of second-order “ring-ring” type angular focusing is found. Corpuscular-optical parameters of the electrostatic quadrupole-cylindrical mirror are investigated in present work. The quadrupole-cylindrical field is constructed on the basis of the superposition of the cylindrical field $\mu \ln r$ and the axially-symmetric cylindrical quadrupole:

$$U_q(r, z) = U_0(\mu + z) \ln r \quad (1)$$

where μ is the coefficient that determines the weight contribution of the cylindrical field.

The quadrupole-cylindrical field (1) at value $\mu = 1$ coincides with the well-known Wannberg field [3]. The potential of the Wannberg field in the coordinate system r, z is described by the following expression

$$U = \frac{V}{\ln \frac{r_1}{r_0}} (1 + Az) \ln \frac{r}{r_0} \quad (2)$$

where A is a small dimensionless parameter.

Wannberg numerically found that the analyzer on the basis of the proposed modified potential field (2) provides simultaneous focusing in the wide energy range and the focal surface can be approximated to the surface of the inner cylindrical electrode (at $r = r_o$) for energies within 7-16% of the central energy.

1. Calculation of corpuscular-optical parameters of the quadrupole-cylindrical mirror

Fig.1 shows the scheme of the energy analyzer with “ring-ring” type focus. The field is formed in the space between two axially-symmetric coaxial electrodes. The inner cylindrical electrode (radius r_o) is grounded. The outer electrode under the potential U creates nonuniformity of field

and has the curvilinear profile $r = r_o \exp\left[\frac{\ln(r_1/r_o)}{(1 + Az)}\right]$.

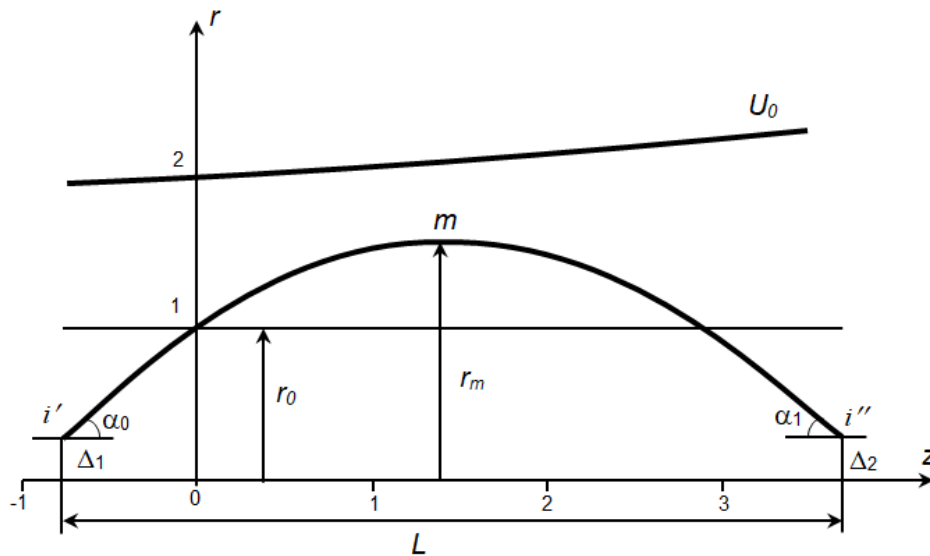


Fig.1.The scheme of the quadrupole-cylindrical energy analyzer

Schemes of quadrupole-cylindrical energy analyzers with various contributions of the dimensionless parameter $A = + 0.01$, $A = 0$, $A = - 0.01$ are studied. The “ring-ring” type focusing is considered for all schemes (the ring source of charged particles and the ring detector are located near the inner cylindrical electrode).

For analyze of parameters of the electrostatic quadrupole-cylindrical energy analyzer, first, second and third order aberration coefficients of spatial focusing were determined by the approximate-analytical method of calculation of the charged particles trajectory:

$$A_I = \frac{dl}{d\alpha} = \Delta_1 [1 + \text{ctg}^2 \alpha_0] + \frac{d\xi_i}{d\alpha} + \Delta_2 \frac{d}{d\alpha} (\text{ctg} \alpha_1), \tag{3}$$

$$A_{II} = \frac{d^2 l}{d\alpha^2} = 2\Delta \text{ctg} \alpha_0 [1 + \text{ctg}^2 \alpha_0] + \frac{d^2 \xi_i}{d\alpha^2} + \Delta \frac{d^2}{d\alpha^2} (\text{ctg} \alpha_1), \tag{4}$$

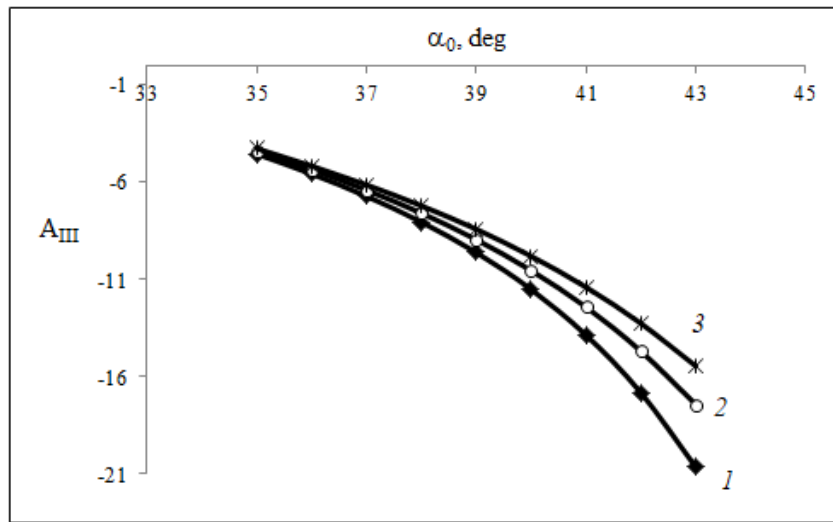
$$A_{III} = \frac{d^3 l}{d\alpha^3} = -2\Delta [1 + 4\text{ctg}^2 \alpha_0 + 3\text{ctg}^4 \alpha_0] + \frac{d^3 \xi_i}{d\alpha^3} + \Delta \frac{d^3}{d\alpha^3} (\text{ctg} \alpha_1), \tag{5}$$

where ξ is projection of the trajectory of charged particles on the symmetry axis z of the mirror in the section from i' to i'' ;

Δ_1, Δ_2 are values of the distance from the source and its image to the surface of the inner cylindrical electrode (Fig. 1), $\Delta = \frac{\Delta_1 + \Delta_2}{2}$ is the value of the average total distance;

$l = \frac{L}{r_0}$ is the total projection of the particle trajectory on the symmetry axis z of the mirror from the source to its image.

Fig. 2 allows to compare the focusing quality of schemes with different values of the “shaping parameter” A . The dependence of the cubic angular aberration coefficient A_{III} on the entrance angle α_0 of charged particles is showed here. As can be seen from Fig. 2, with increasing of the entrance angle α_0 , an increase of the cubic angular aberration coefficient is observed, which leads to a decrease of the resolution ability of the energy analyzer.



1 - scheme with $A = +0.01$, 2 - scheme with $A = 0$, 3 - scheme with $A = -0.01$.

Fig.2. The dependence of cubic angular aberration coefficient A_{III} on entrance angle α_0

Comparison of parameters of electron-optical schemes with different values of “shaping parameter” A shows that cubic angular aberrations coefficients A_{III} of schemes with $A < 0$ are smaller than for schemes with $A > 0$ and smaller than for the cylindrical mirror analyzer corresponding to schemes with $A = 0$. This means that mirror analyzers based on quadrupole-cylindrical fields with improved particle-optical parameters should be chosen among schemes with $A < 0$.

2. Results and discussion

Results of the numerical modeling of the scheme of the quadrupole-cylindrical energy analyzer with $A = -0.01$ are given below. Numerical modeling was carried out by using the “Focus” program [4] for modeling systems of electronic optics.

The profile of the outer deflecting electrode is determined from the calculation of equipotential lines of the quadrupole-cylindrical field. Fig.3 shows equipotential lines of the electrostatic quadrupole-cylindrical field with $A = -0.01$.

As can be seen from Fig. 3, for a small value of $A = -0.01$, the profile of the outer deflecting electrode is well approximated by a cone whose generatrix has a small inclination angle with respect to the symmetry axis z of the mirror, equal to ~ 1.75 deg.

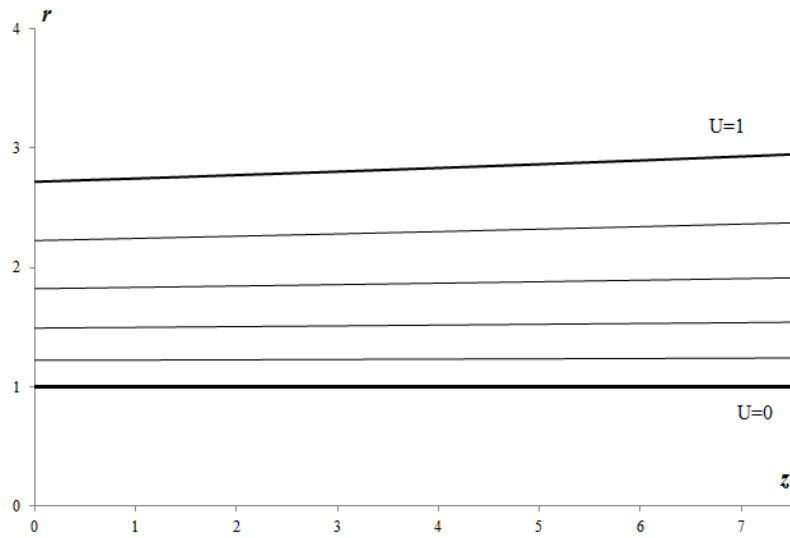


Fig.3. Equipotential lines of the quadrupole-cylindrical field with $A = -0.01$

Fig. 4 shows the dependence of the arrival point of the particle (the point i'') from the entrance angle α_0 . It follows from Fig.4 that the optimum range of entrance angles of particles is the angle interval from $35^\circ - 45^\circ$, which provides a maximum luminosity $\Omega = 8.2\%$ and the best focusing of charged particle beam.

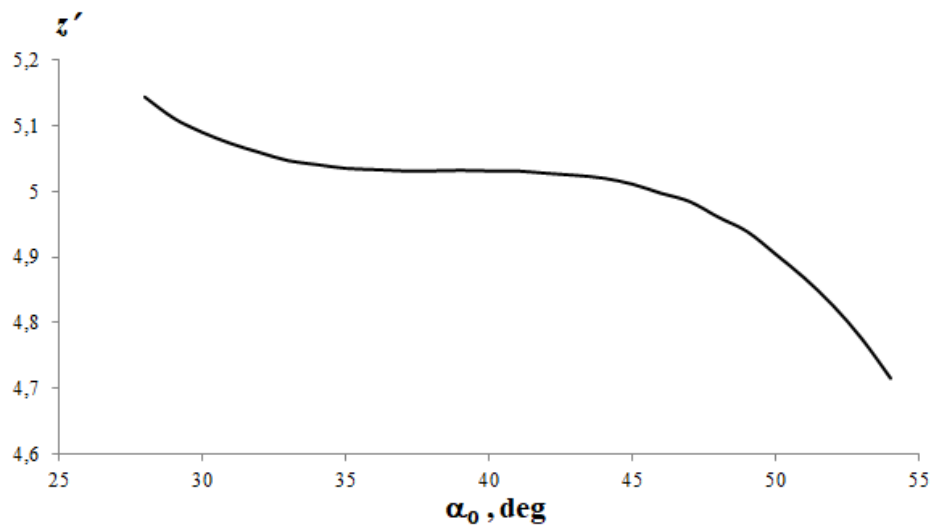
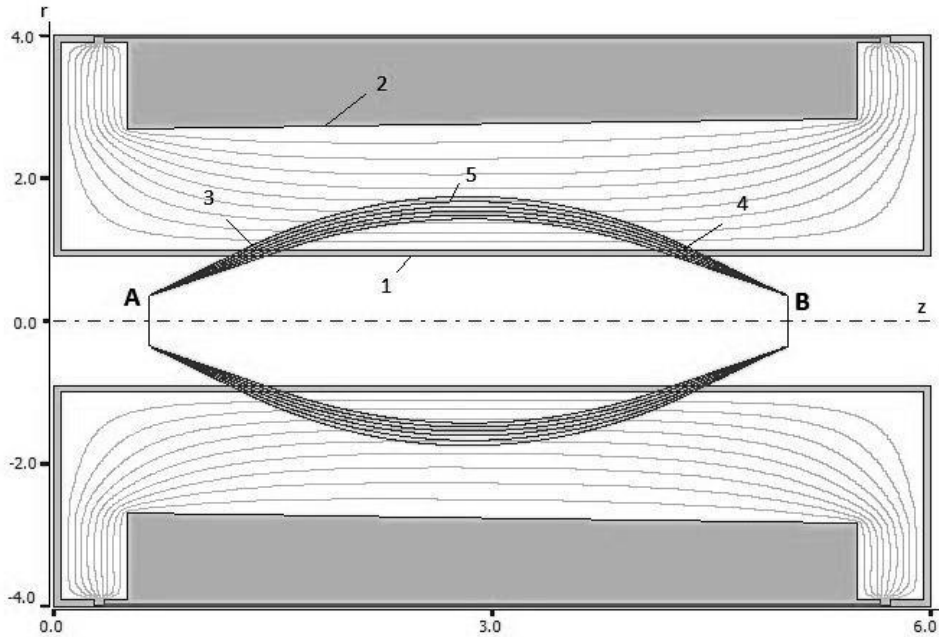


Fig. 4. The dependence of the arrival point of the particle on the entrance angle α_0

Fig.5 shows trajectories of charged particles in the energy analyzer scheme with $A = -0.01$, calculated by using the “Focus” program. According to the scheme, charged particles fly from the thin ring electron-optical source A in the range of polar angles from 35° to 45° , then get through the entrance slit in the field, and under the action of the potential of the outer electrode are deflected back, and are focused into the ring image B.



1 – the inner grounded cylindrical electrode, 2 – the outer deflecting electrode, 3 and 4 - entrance and exit slits, A - thin ring source, B - ring image, 5- charged particles beam

Fig.5. Trajectories of charged particles beam in the quadrupole-cylindrical energy analyzer with $A = -0.01$

The scheme provides the second-order “ring-ring” type angular focusing regime. The relative energy of the particles is $E/U = 1$. The position of the ring source is $x = 0.65$; $y = 0.35$. Values of the distance of the source and its image from the surface of the inner cylindrical electrode, which are considered positive inward from the radius r_0 , are equal to $\Delta_1 = \Delta_2 = 0.35$. All dimensions are expressed in conventional units. The table presents results of calculation of corpuscular – optical parameters of the energy analyzer on the basis of the quadrupole-cylindrical field at $A = -0.01$.

Table 1. Corpuscular – optical parameters of the energy analyzer on the basis of the quadrupole-cylindrical field at $A = -0.01$

| | |
|--|-------------|
| Focusing type | «ring-ring» |
| Focusing order | 2 |
| Center focusing angle | 38.3^0 |
| X coordinate of focusing | 5.03 |
| Y coordinate of focusing | 0.35 |
| The total length of the electron-optical scheme, $l = L/r_0$ | 6 |
| Reflection parameter, P | 1 |

For calculate the instrumental function of the quadrupole-cylindrical energy analyzer, particles from the ring source start in the range of the initial angles of $35^\circ - 45^\circ$ and in the range of initial energies 0.993-1.007. Fig. 6 shows the instrumental function of the proposed energy analyzer at $A = -0.01$ for the “ring-ring” type angular focusing regime. The relative energy resolution at half-height of the instrument function of the energy analyzer with a radius of the exit diaphragm $0.02 r_0$ is 0.58%.

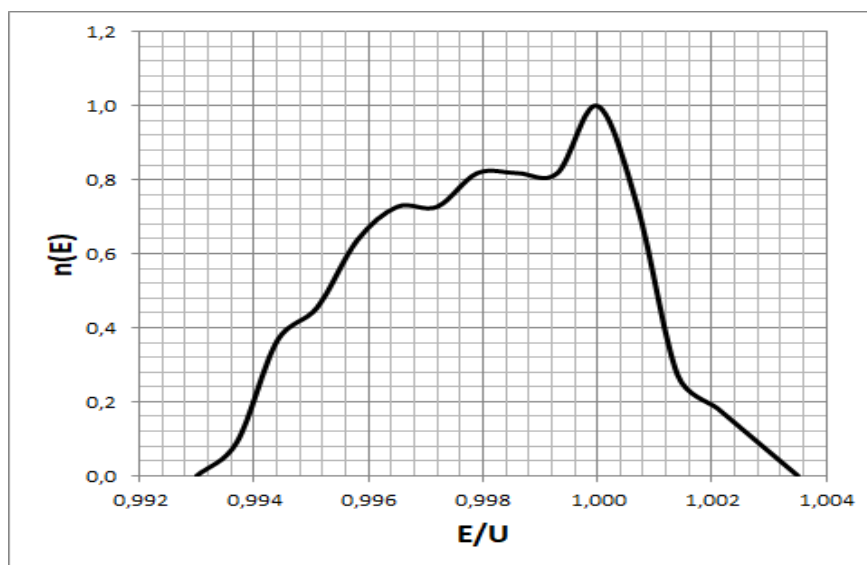


Fig. 6. The instrumental function of the quadrupole-cylindrical energy analyzer with $A=0.01$

Conclusion

Investigation of corpuscular-optical parameters of the energy analyzer on the basis the quadrupole-cylindrical field is carried out. It is shown that the best quality of focusing has the scheme with $A = -0.01$, whose the outer electrode has an increasing exponential profile at a small angle of inclination relative to the symmetry axis of the mirror, equal to 1.75° . For ensure maximum luminosity, the range of entrance angles of particle of start should be from 35° to 45° (in this case luminosity is 8.2%).

REFERENCES

- 1 Kambarova Zh.T., Saulebekov A.O. Calculation of the structure of electrostatic quadrupole-cylindrical fields. *Bulletin of the Karaganda University. «Physics» series*. 2018, No. 1 (89), pp. 66 – 71.
- 2 Kambarova Zh.T., Saulebekov A.O. Development of mirror energy analyzer based on electrostatic quadrupole-cylindrical field. *Eurasian Physical Technical Journal*. 2017, Vol.14, No 2 (28), pp. 42 – 47.
- 3 Wannberg B. An electrostatic mirror spectrometer with coaxial electrodes for multi-detector operation. *Nuclear Instruments and Methods*.1973, Vol.107, pp. 549 – 556.
- 4 Trubitsyn A., Grachev E., Gurov V., Bochkov I., Bochkov V. *Proceedings of SPIE*. 2017, Vol.10250, pp. 0V-1 – 0V-7.

UDC 699.871

PHOTOCATALYTIC PROPERTIES OF TiO₂/Ag NANOSTRUCTURES

Serikov T.M., Ibrayev N.Kh., Zeinidenov A.K.

Institute of Molecular Nanophotonics, Ye.A. Buketov Karaganda State University,
Universitetskaya Str.28, Karaganda, 100026, Kazakhstan, a.k.zeinidenov@gmail.com

In this paper the size and shape of the core-shell nanoparticles were determined with the help of electron microscopic studies. The process of photodegradation of the dye of methyl blue was studied. Dependence from the time of UV irradiation with films of titanium dioxide nanoparticles and without their presence was studied, as well as with the "core-shell" structure of Ag / TiO₂ composition, where the core is silver nanoparticles and shell is the titanium dioxide nanoparticles. In the result of the research the action of the photocatalyst on the basis of core-shell Ag / TiO₂ significantly accelerates the oxidation of the methylene blue dye.

Keywords: photocatalysis, core-shell, plasmonics, nanoparticle, titanium dioxide, methylene blue dye.

Introduction

One of the most advanced and environmentally friendly methods of hydrogen generation is the method of photocatalytic decomposition of water by means of semiconducting materials [1, 2]. A promising material for these purposes is titanium dioxide. Compared with other photoactive materials for hydrogen production titanium dioxide attracts increasing attention of researchers because of its relative cheapness, availability, stability and functionality as well as the possibility to obtain various nanostructures, such as nanoparticles, nanotubes, nanorods and nanowires. Physico-chemical properties of films based on nanostructures depend on the method of their production and are determined by the size and shape of the particles, imperfection, phase composition, structure and size of the film far [3].

In 1987 Anpo co-authored [4] published a paper on the effect of TiO₂ colloidal particles sizes on their photocatalytic activity. In the paper the nanoparticles of titanium dioxide of anatase and rutile modification with different particle diameters were obtained. It was shown that with decreasing size of the titanium dioxide nanoparticles photocatalytic activity increases for both anatase and rutile. It should be noted that the reactivity of the anatase modification is higher than with the rutile. The investigation of the influence of geometric characteristics on the photocatalytic properties was discussed extensively and was proved in many studies.

One of the main drawbacks of nanostructures based on titanium dioxide is a wide band gap. As it is known, the proportion of ultraviolet radiation in the solar spectrum is about 10% [5]. This fact limits the use of titanium dioxide in various applications. To solve this problem ones resort to various modifications of TiO₂ structures. Doping of titanium dioxide nanostructures by ions of Mo, Ru, Cu, Fe and N which leads to an increase in their photocatalytic activity [6]. It is believed that doping by anions, in contrast to the doping by metal cations creates less recombination centers and, therefore, is more effective for increasing the photocatalytic properties of titanium dioxide.

There are other methods of increasing the spectral sensitivity of nanostructures based on titanium dioxide, the creation of composite systems with the addition of CuO, CdS, ZnS Fe₂O₃ [7]. The proposed modification techniques have several drawbacks, foremost of which is that doping takes place during the synthesis or by thermal annealing. Upon doping during synthesis, doping elements are incorporated in the crystal structure of titanium dioxide. Tampering into the crystal lattice will change the entire structure, as a result electrical and photovoltaic properties of titanium dioxide will change too.

A promising direction of increasing the photocatalytic activity of titanium dioxide nanostructures is the use of surface plasmon resonance, which nanoparticles of a number of noble metals have (Au, Ag, Pt, Pd). Basically it is suggested to use NP of silver which have maximum plasmon effect in the visible spectral region [8]. However, the problem of oxidation of the silver nanoparticles is still unsolved. One solution to this is to use the "core-shell" structures, the core of which serves NP of metal and the shell is a semiconductor oxide metal (TiO_2). It is expected that the use of such geometrical design will protect the NP of metal from oxidation by electrolyte and significantly will increase the photocatalytic activity.

This paper presents the results of studies of the effect of silver nanoparticles on the photocatalytic properties of TiO_2 films on the basis of the "core-shell" structures.

1. Experiment. Obtaining of TiO_2 nanoparticles films.

For obtaining films of titanium dioxide nanoparticles a solution containing powder of colloidal TiO_2 (Sigma Aldrich) was prepared. The solution was prepared as follows: colloidal TiO_2 powder was ground in a porcelain mortar with a small amount of deionized water and acetone taken in a volume ratio of 10:1. Acetone was added to prevent clumping of the particles. After the formation of a homogeneous viscous paste solution of titanium dioxide nanoparticles was deposited on the FTO surface (glass coated with tin oxide doped with fluorine) by doctor-bleeding method. The resulting film was subjected to heat treatment at a temperature of $500\text{ }^\circ\text{C}$ during 2 hours.

Synthesis of the "core-shell" structures.

Sodium borohydride weighing 0,001 g was dissolved in 25 ml of ethanol. Silver nitrate solution in a ratio of 0.0045 g was dissolved in 10 ml of ethanol. The resulting AgNO_3 solution with constant stirring was added to a cooled to -2°C solution of sodium borohydride in several steps with 50 microliters. For obtaining the "core-shell" structures ethanol solution of silver nanoparticles and titanium tetraisopropoxide TIPT ($\text{Ti}(\text{OCH}(\text{CH}_3)_2)_4$) was used. 1 ml of TIPT solution was added into 10 ml of silver nanoparticles solution.

For the synthesis of TiO_2 shell ethanol solutions TIPT and silver NP were mixed with vigorous stirring. The resulting mixture was stirred during 12 hours on a multi-functional rotator PTR-35 at a room temperature in the dark. From these structures the films were made.

For comparison of the photocatalytic activity of nanostructured TiO_2 films the reaction of photocatalytic decomposition of methylene blue dye (MB) was used by irradiation of UV light of a mercury lamp PRK-2. Sorption of dye molecules of MB into the films was carried out by keeping TiO_2 films in ethanol solution of luminophore with an initial concentration of $C^0=10^{-5}$ mol/l during 5 hours, followed by drying the film in an oven during 1 hour.

The photocatalytic efficiency of TiO_2 nanostructured films in the model reaction of photodegradation of the methylene blue dye was determined by the equation:

$$\eta = \frac{A_0 - A}{A_0} * 100\% \quad (1)$$

where A_0 - optical density of the dye without photocatalyst, A - optical density of the dye with the photocatalyst.

The absorption spectra of the films by methylene blue dye were prepared by a double-beam spectrophotometer Cary 300 UV-Vis.

The morphology of the obtained samples was investigated by using scanning electron microscopy (SEM) on a microscope MIRA 3LMU (Tescan, Czech Republic). The voltage on the accelerating electrode was from 20 to 30 kV.

2. Results and discussion

The morphology of the film surface of the nanoparticles and the "core-shell" structures are shown in Figure 1. From Figure 1, a it is evident that the film of titanium dioxide nanoparticles has a distinct granular structure. The particle size is about 25-30 nm. The thickness of the semiconductor layer is 8.3 microns.

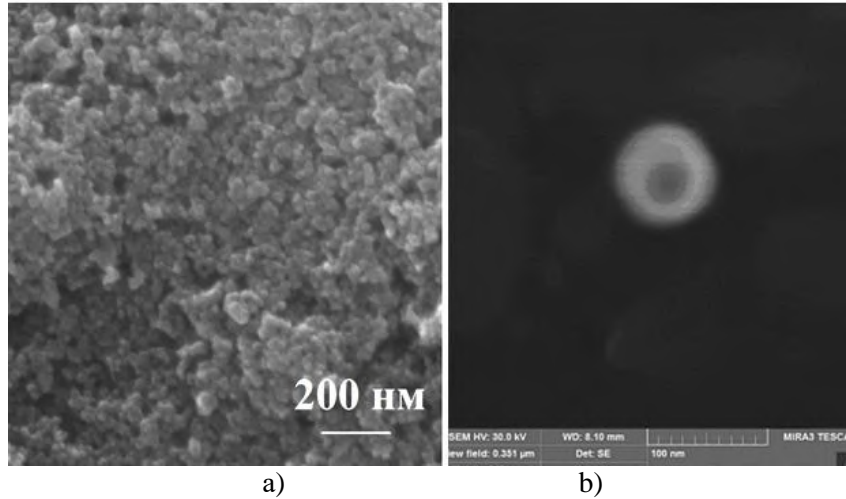


Fig. 1. SEM image of the film surface of titanium dioxide (a) and the "core-shell" structure (b).

Addition of silver nanoparticles of titanium tetraisopropoxide (TIPT) into solution the "core-shell" structure of a spherical shape is formed, which is shown in Figure 1, b. From the figure it is evident that in the center of the structure there is silver nanoparticle and the shell is formed by titanium dioxide.

Effect of silver nanoparticles on the photocatalytic activity of nanostructured TiO₂ films was investigated by the degradation of methylene blue dye molecules by the action of light.

The process of degradation of methylene blue dye can be described as follows. Irradiation with UV light leads to the generation of electron-hole (e⁻ - h⁺) pairs in TiO₂ nanostructure due to the absorption of the photon (process 2). Photogenerated electrons in the conduction band of TiO₂ react with oxygen molecules adsorbed on the TiO₂, as a result superoxide radicals (O₂⁻) are formed (process 3). In this case the holes in the valence TiO₂ zone react with water molecules and contribute to the formation of hydroxyl radicals (OH[•]) (process 4). Highly reactive hydroxyl radicals (OH[•]) and superoxide radicals (O₂⁻) react with a dye molecule adsorbed on the TiO₂ nanostructures and cause its degradation. During this reaction, there is discoloration of the dye solution (processes 5 and 6).



Figure 2 shows the absorption spectra of the methylene blue dye in aqueous solution.

As it is evident from the figure the absorption band of MB dye has a maximum $\lambda_1^{\text{max}} = 664 \text{ nm}$ at a wavelength and a half width $\Delta\lambda_{1/2}^{\text{absorp}} = 71 \text{ nm}$. UV irradiation of MB solution decreases the optical density of the dye molecules in ~1.1 times (Figure 2, a). When measuring the absorption

spectra of the MB dye at the presence of TiO_2 films the decrease of optical density at a wavelength of 664 nm in $\sim 1,7$ times is observed (Figure 2, b). The criterion for complete destruction of MB in the photocatalytic oxidation process is the lack of optical activity of MB solution in the range of 200 - 900 nm, which indicates the destruction of the MB molecule and its destruction products to the mineral compounds.

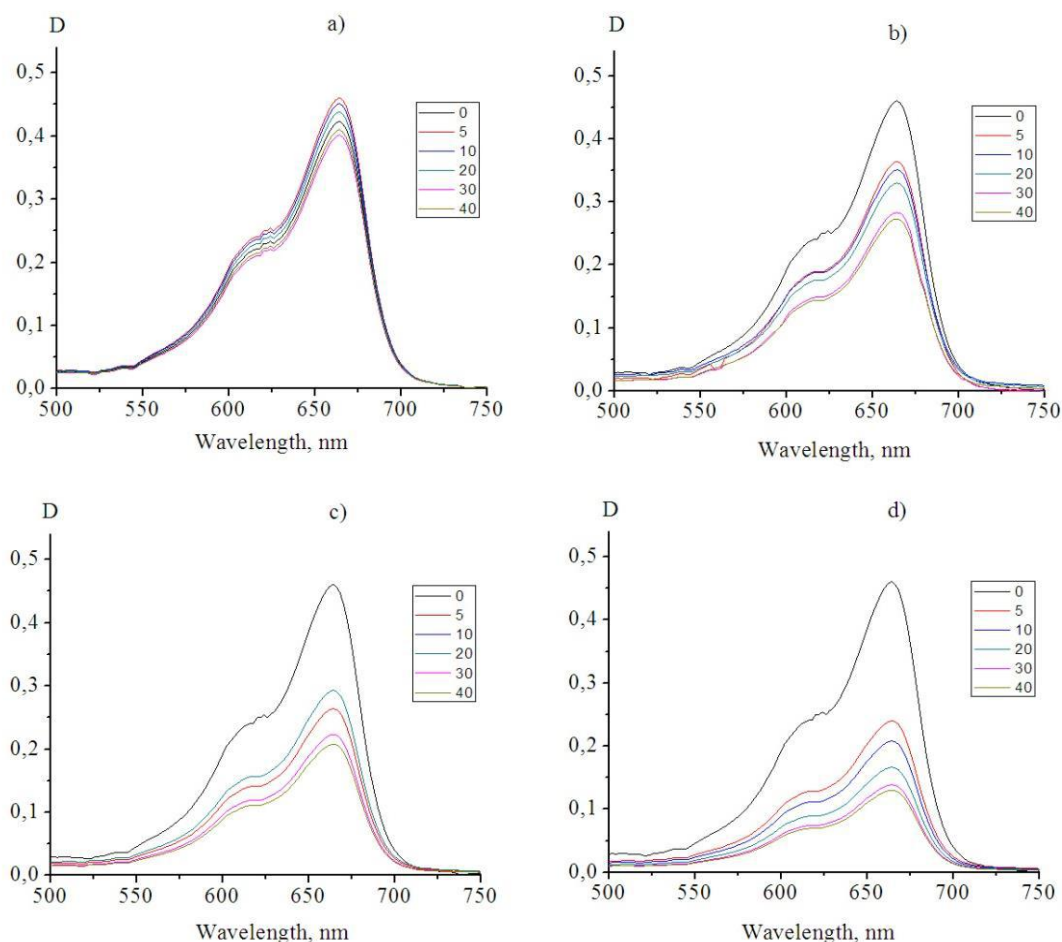


Fig. 2. The absorption spectra of the methylene blue dye in aqueous solution

When silver nanoparticles are added to the TiO_2 films the value of optical density in the MB absorption band is reduced in 2, 3 times (Figure 2, c). The presence in the solution of film dye of titanium dioxide with the "core-shell" structure leads to a decrease in the optical density in the absorption band of the dye in $\sim 3,8$ times (Figure 2, d). Wherein the position of the maximum of the absorption band and its half-width does not change.

The photocatalytic activity of the nanostructures was determined from the measurement of the optical density of the methylene blue dye on the spectrophotometer Agilent Cary 300. The dependence of the optical density D of the solution of methylene blue on oxidation time is shown in Figure 3. A comparative analysis of the impact of silver nanoparticles and the "core-shell" structure on the photocatalytic activity showed that doping of the "core-shell" structure affects more than the introduction to the system of silver nanoparticles. The calculations showed that at the dye photodecomposition without catalyst the oxidation state is $\eta=6.25\%$. When using TiO_2 films on the basis of the spherical nanoparticles oxidation degree was 35.4%, and for the "core-shell" structure was 76.6%.

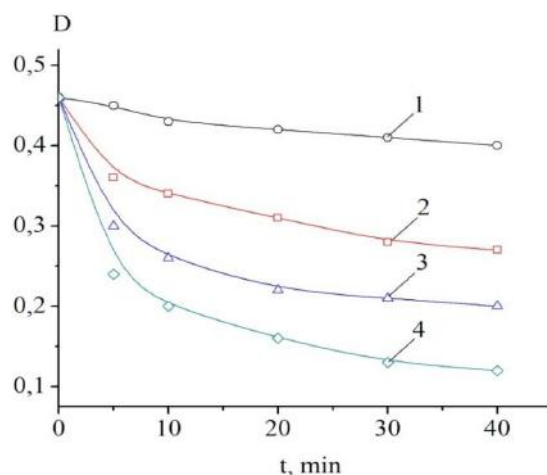


Fig.3. The dependence of the optical density of methylene blue on the irradiation time:
 1 - an aqueous solution of methylene blue; 2 - a solution with TiO₂ film;
 3 - solution with a film based on the "core-shell" structures of Ag/TiO₂ structure.

Conclusion

Thus, in the paper the photocatalytic activity of nanostructured films of titanium dioxide from nanoparticles and the "core-shell" structure was investigated. As a result of sensibilization of nanostructured films by the dye molecules of methylene blue and their UV radiation a decrease of its optical density associated with the photodegradation of the dye is observed with the lapse of time. The calculations showed that at the dye photodecomposition without catalyst the efficiency was 6,25%. The efficiency of the dye photodecomposition using films based on spherical , that the film based on the "core-shell" structure has the best photocatalytic properties.

Acknowledgments

This study was financially supported by the Committee of Science of the Ministry of Education of the Republic of Kazakhstan (General information BR05236691).

REFERENCES

- 1 Eason G., Noble B., Sneddon I.N. On certain integrals of Lipschitz-Hankel type involving products of Bessel functions. *Phil. Trans. Roy. Soc. London*, 1995, Vol. A247, pp. 529 - 551.
- 2 Clerk Maxwell J. *A Treatise on Electricity and Magnetism*, 3rd ed., Oxford: Clarendon. 1892, Vol. 2, pp. 68 – 73.
- 3 Jacobs I.S., Bean C.P. Fine particles, thin films and exchange anisotropy, in *Magnetism*. New York, Academic, 1963, Vol. III, , pp. 271 - 350.
- 4 Anpo M., Shima T., Kodama S., Kubokawa Y. Photocatalytic hydrogenation of propyne with water on small-particle titania: size quantization effects and reaction. *J. Phys. Chem. USA*. 1987, Vol. 91, pp. 4305–4310.
- 5 Goswami D.Y., Zhao Y. *Solar Energy and Human Settlement. Proceedings of ISES World Congress Springer Science & Business Media*. 2009. Vol. 1, pp. 3115–3120.
- 6 Zhang Z., Wang C., Zakaria R., Ying Y. Role of Particle Size in Nanocrystalline TiO₂-Based Photocatalysts *J. Phys. Chem.* 1998. Vol. 102, pp. 10871–10878.
- 7 Hung W.H., Chien T.M., Tseng Ch.M. Enhanced photocatalytic water splitting by plasmonic TiO₂-Fe₂O₃ cocatalyst under visible light irradiation *J. Phys. Chem.* 2014. Vol. 118, №24, pp 12676–12681.
- 8 Catchpole K.R., Polman A. Plasmonic solar cells *Optics Express*. 2008. Vol. 16 , pp. 21793–21800.

UDC (535.34+535.37):577.164.12

THE NATURE OF ELECTRONIC SPECTRA OF SELF-COMBINED RIBOFLAVIN MOLECULES

Astanov S.Kh., Kasimova G.K.

Bukhara Engineering-Technologies Institute, Bukhara, Uzbekistan, s.h.ostonov@rambler.ru

The self-assembly of riboflavin molecules in aqueous and binary mixtures of solvents was studied by a spectroscopic method. It is shown that the self-assembly of vitamin B2 molecules occurs as a dipole-dipole and strong inductive-inductive interaction, as a result of which a resonant splitting occurs by excitation of electronic levels of riboflavin molecules. For self-aggregated molecules in the spectra of linear dichroism, hidden adsorption bands are identified, on the basis of which schemes of electronic transitions to absorption are constructed.

Keywords: riboflavin, self-aggregation, luminescence, fluorescence, spectrum, absorption, structure, hydrogen bonds, electronic transitions.

Introduction

Self-assembly is a process in which only components of the final structure participate [1, 2]. The main condition for the self-assembly of nano particles is the formation of a high-molecular local volume [3]. One of the methods for the formation of a local volume with high concentrations is by thermal evaporation of the solvent from a drop of a solution of the dissolved test compound. The authors [4, 5] obtained ring structures of nano particles on the surface of the glass substrate. Self-assembly of molecules can also be carried out in concentrated solutions and binary mixtures of solvents. The choice of the technique for obtaining self-assembled molecules is one of the topical issues of this direction. The process of the formation of aggregates is accompanied by a significant deformation of the electronic spectra in the form of a hypochromic effect [1-4].

1. Objects and methods of research.

Riboflavin powders of the brand "ChDA" are used in the work. Electronic absorption spectra were measured on an EMC-30PC-UV spectrophotometer, which allows measurements of optical density values with an accuracy of 0.3% and a high resolution in the range of 190-1100 nm. Measurement of the fluorescence and luminescence excitation spectra was carried out using an apparatus assembled on the basis of two monochromators of the MDR-76 type with photoelectron registration. For the convenience of comparing the absorption and fluorescence spectra, they are normalized to unity. The optical rotation dispersion and the linear dichroism spectra were recorded on a Jasko circular dichrograph using the Fresnel double parallelepiped optical attachment calculated for the visible and UV portions of the spectral region.

As solvents, we used: bidistilled water, ethyl alcohol, acetone, chloroform purified according to the procedure [6]. Binary solvents were also used: alcohol + acetone, alcohol + chloroform. Self-assembly of riboflavin molecules was carried out in binary mixtures of solvents: alcohol + acetone, alcohol + chloroform. Quantum-chemical calculation of the electronic structure of the charge distribution and dipole moment, mainly of the excited state of the electrons, was carried out using the MORAS 2009[7], software package, by the semiempirical AM1 method for standard elections parameters [8]. Preliminary optimization of the geometry of molecules using the limited Hartree-Fock method and the Polak-Ribier algorithm with an accuracy of 0.001kcal / (A⁰mol) and taking into account various versions of the initial confirmations was preliminarily carried out.

2. Experimental results and their discussion of the influence of the concentration and composition of solvent binary.

In our early works, the concentration dependence of the electronic spectra of riboflavin in water was studied. It is shown that in the highly concentrated aqueous solutions ($10^{-5} \text{ m} \div 2 \cdot 10^{-3} \text{ m}$) there is a decrease in the absorbing and luminescent capacity of the solution, i.e., a hypochromic effect is observed. These phenomena are explained that at a concentration of $10^{-5} \div 10^{-6} \text{ m}$, riboflavin molecules are in the monomeric state. The observed hypochromic effect in the high-concentration range refers to the self-aggregates of the riboflavin molecules. We observed significant deformations of the electronic spectra in binary mixtures of solvents [7-9].

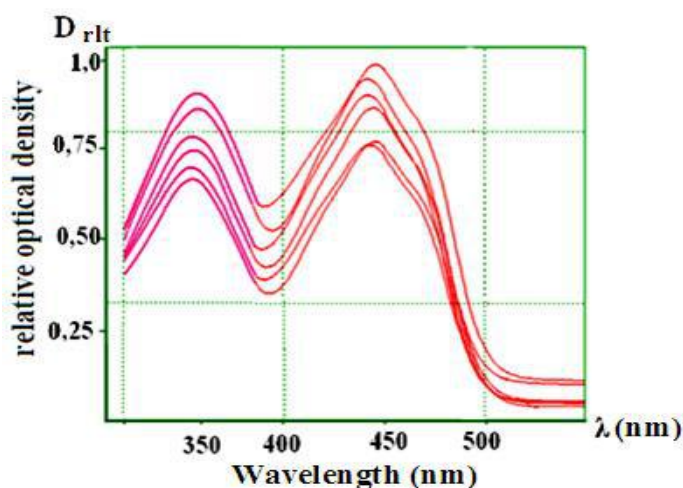


Fig.1a. Absorption spectrum of riboflavin ($C 10^{-4} \text{ M}$) in a binary mixture of alcohol + acetone solvents depending on the fraction of acetone added (0-1, 20-2, 30-3, 50-4, 70- 5) in% by volume ratio.

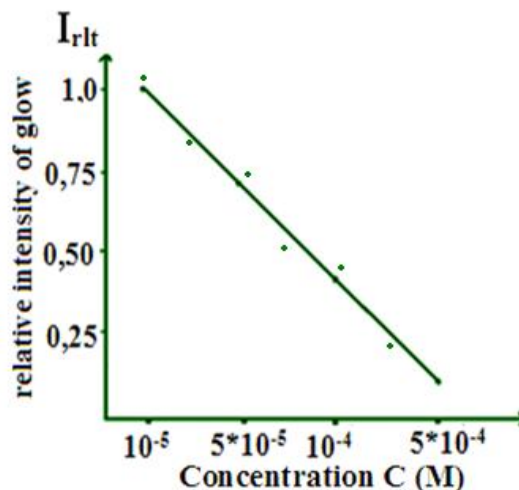


Fig.1b. Dependence of the relative yield of luminescence on the concentration of riboflavin molecules in a binary solvent mixture of alcohol + acetone (0.35 + 0.65)

Binary solvents were chosen in such a way that the concentration of the test compound remained constant, the binary ratios of the solvent mixtures varied. In the second case, the composition of binary mixtures of solvents remained constant, the concentration of vitamin B₂ changed. Other conditions for the use of binary solvents were that solvents were infinitely dissolved among themselves. As an example, Fig. 1 shows the absorption spectra of riboflavin at a constant concentration ($C 10^{-4} \text{ M}$) in binary mixtures of alcohol + acetone solvents as a function of the fraction of acetone added.

As can be seen from Fig. 1, the absorption spectrum of riboflavin in pure alcohol practically coincides with the band of vitamin obtained in dilute aqueous solutions. However, with an increase in the fraction of acetone in binary mixtures, the fall of the integral absorption bands of riboflavin is observed. In these cases, the relative intensity of the luminescence of the vitamin molecules is also observed. Similar changes in the electronic spectra, as well as in the relative yield of luminescence at a constant ratio of binary mixtures of solvents, are observed with an increase in riboflavin concentration. Fig. 1, b shows the dependence of the luminescence yield on the concentration of riboflavin molecules with constant mixtures of binary solvents alcohol + acetone (0.35-0.65). As can be seen from Fig. 1b, at a constant ratio of binary mixtures of solvents, concentration quenching of the luminescence is observed. Such concentration quenching of luminescence was observed by us in binary mixtures of solvents for arylethylene molecules and food dyes. These phenomena are explained by the manifestation of aggregation of the molecules under study in binary mixtures of solvents [12-14]. The observed phenomena in binary mixtures of alcohol + CHCl_3 alcohol solvents

and alcohol + acetone are also possibly associated with the process of self-aggregation of vitamin molecules.

The process of aggregation in binary mixtures of solvents for riboflavin molecules can be explained on the basis of the following reasoning. When dissolving riboflavin in alcohol, each molecule of riboflavin will appear in the solvate of an alcoholic solvent. In this case, the MMVs are eliminated directly between the molecules of the dissolved compound, and they will be in the monomeric state.

The addition of an insoluble component of solvents, whereby these components are combined by a hydrogen bond, $ROH \dots OR$, $Ror OH \dots ClR_2$, where $R, R_1 \text{ и } R_2$ respectively, the lagging part of the molecules of alcohol, acetone and chloroform, respectively. As a result, the MMW solvate around the dissolved substance weakens. An increase in the fraction of the second component of the binary solvent leads to a further weakening of the solvate around each molecule of riboflavin. In these cases, the molecules of the test compound come out of the solvate and there is the possibility of interaction between the molecules of the dissolved molecules. These processes lead to the formation of a local volume with a high concentration, which lead to self-aggregates of the vitamin. Self-assembly of riboflavin molecules is carried out. At the first stage of aggregation, dimers are formed. As the fraction of insoluble component $CHCl_3$, acetone increases, the process of aggregation of the medication molecules intensifies and complex or more complex aggregates of the vitamin B_2 are formed. To confirm this assumption, we conducted a temperature study of the electronic spectra of solutions of riboflavin, where a hypochromic effect is observed in the absorption and emission bands.

3. Temperature studies.

It was experimentally established that an increase in the temperature of the solution, where a hypochromic effect occurs, an increase in the absorbing and luminescent capacity of the solution was observed. At a temperature of 75-80⁰C, the absorption and emission spectra of the monomeric molecules of the test compound are restored. From the temperature experiments, the binding energy of self-aggregates of riboflavin molecules was determined. This energy corresponds to a value of 16-20 KJ / mol, which corresponds to the energy of the hydrogen bond. On the basis of the obtained experimental results, it can be assumed that a certain binding energy refers to the alcohol + acetone, alcohol + chloroform system, and the riboflavin molecules combine under the action of van der Waals forces. To find out which of the Van der Waals forces lead to the very aggregation of riboflavin molecules, it is definitely the distribution of charges on the atoms of vitamin B2. Also, dipole moments in the main μ and $\mu, *$ electronic states of the test compound were determined [9]. The calculated values of the dipole moment are $\mu = 7.222 \text{ Db}$ $\mu = 23.538 \text{ Db}$. These values show, when self-aggregating riboflavin molecules, a strong dipole-dipole interaction occurs. For the nature of electronic states, we determined the frequencies of the 0-0 transition and the most probable transitions to absorption and luminescence were calculated for monomeric and self-aggregates of riboflavin molecules. For this purpose, the electron spectra were translated in the frequency scale and normalized to unity by the intensity (Fig. 2).

As can be seen from Fig. 2, the frequencies corresponding to the intersection point normalized absorption and emission spectra, i.e. for dilute solutions correspond to the values of the frequencies of the purely electronic transition $\nu_{00} = 20.200 \text{ sm}^{-1}$. The most probable frequency transitions in the absorption (ν_p^a) (from left to right on the frequency scale) for dilute solutions of aqueous and binary solvent mixtures correspond to:

$$\begin{aligned} \nu_p^{a1} = 22300 \text{ sm}^{-1} & \quad \sigma_p^{a1} = 4530 \text{ sm}^{-1}; & \nu_p^{a2} = 26800 \text{ sm}^{-1} & \quad \sigma_p^{a2} = 8580 \text{ sm}^{-1}; \\ \nu_p^{a3} = 37450 \text{ sm}^{-1} & \quad \sigma_p^{a3} = 4660 \text{ sm}^{-1}; & \nu_p^{a4} = 44840 \text{ sm}^{-1} & \quad \sigma_p^{a1} = 5730 \text{ sm}^{-1}; \end{aligned}$$

Where σ_p^{a1} is the values of the half-width of the corresponding absorption bands. For a dilute aqueous solution of riboflavin, the maximum intensity of the glow corresponds to the frequency $\nu_p^f = 19050 \text{ sm}^{-1}$ and the half-width of this band is significant $\sigma_p^f = 2500 \text{ sm}^{-1}$.

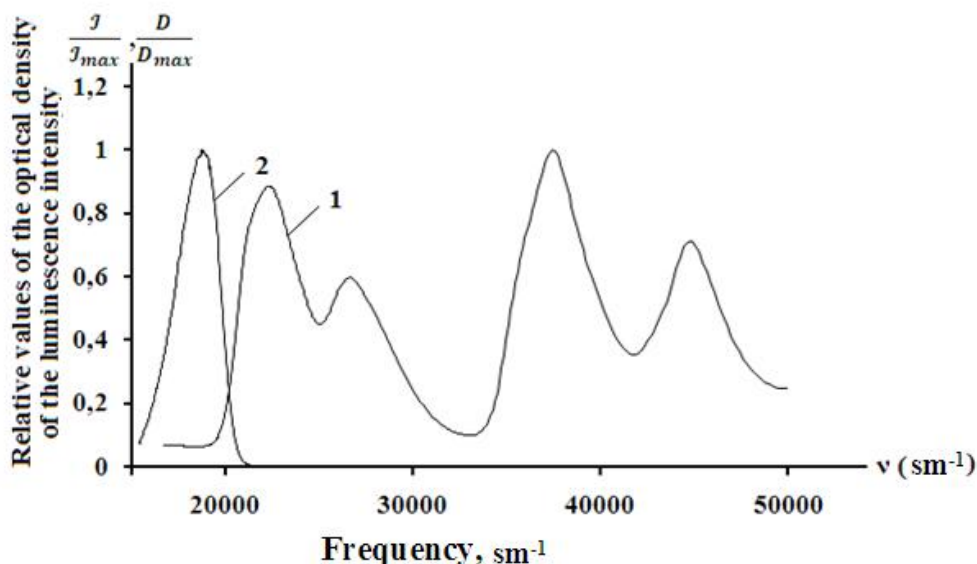


Fig.2. Normalized absorption spectra (1) and fluorescence (2) diluted solutions of riboflavin.

Similarly, it would be desirable to obtain normalized absorption and emission spectra for concentrated aqueous and binary mixtures of riboflavin solvents. However, in aqueous and binary mixtures of solvents of the medication, the absorption spectra will be structureless. Against the background of structurelessness in normalized spectra, electronic absorption and emission bands appear with the following frequencies:

$$\nu^a = 22120 \text{ sm}^{-1}, 37450 \text{ sm}^{-1}, 4500 \text{ sm}^{-1}, 19050 \text{ sm}^{-1}.$$

These electronic bands, according to their maxima and in shape, correspond to dilute solutions of riboflavin. These results show that concentrated solutions of the vitamin B₂ have absorption bands of much lower intensity with respect to the electron bands of dilute solutions. Those sweep bands are hidden against the background of an unstructured adsorption solution.

4. Studies on the spectra of linear dichroism

It is noted in [10] that the spectra of linear dichroism are more informative with respect to absorption spectra. To obtain the relevant information on the position of the bands for concentrated solutions of the preparation, the possibility of measuring the spectra of linear dichroism was investigated. We realized one of these possibilities using the Jasco-20 circular dichrograph, using the optical prefix designed and manufactured for the visible and UV part of the spectrum, the Fresnel double parallelepiped. In practice, the measure of circular dichroism is the magnitude of ellipticity, determined by the ratio of the small and major axis of the ellipse [8-9].

It was experimentally established that when a solution of self-assembled molecules is pumped through a flow cell, they become optically active. Such a flow cell is developed and patented by the authors, and also used to remove the linear dichroism of food dyes and vitamins [11]. Only in this case dichrograph registers a curve of the linear dichroism spectrum that is different from the zero line. To accurately remove the spectrum of linear dichroism, the rate of passage of the solution through a flow cell (2 mm / h) was determined experimentally. Such a speed value was

chosen in order to ensure laminarity of the hydrodynamic molasses. In this case, linearly polarized light falls at an angle of 45° to the measuring cuvette. It has been experimentally established that when pumping solutions of self-assembled molecules through a flow cell, they become optically active. In Fig. 3 shows the spectrum of linear dichroism of self-assembled riboflavin molecules obtained in a laminar hydrodynamic flow in the frequency scale.

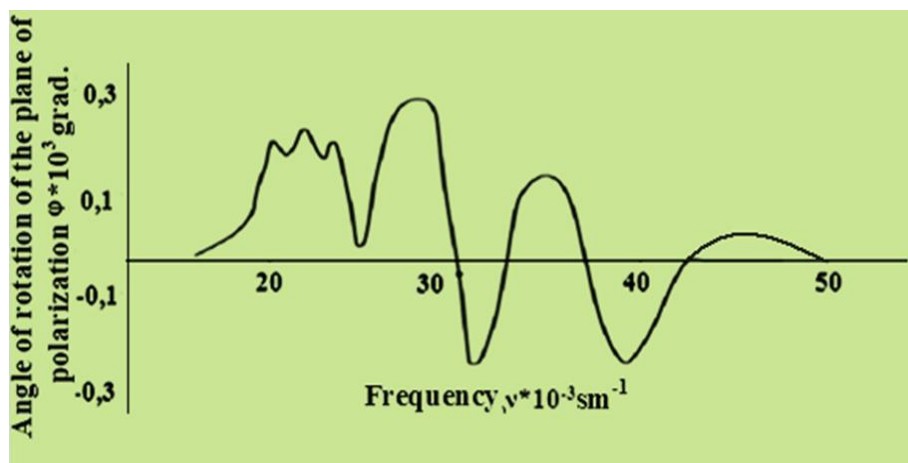


Fig.3. The spectrum of linear dichroism of self-assembled riboflavin molecules in a laminar hydrodynamic flow

As can be seen from Fig. 3, the spectrum of linear dichroism is quite informative. In this case, both long-wavelength and short-wave bands with positive and negative values of the rotation angle of the plane of polarization appear in the spectrum. The observed bands differ greatly in spectral characteristics from the parameters of the main bands of the absorption spectra of riboflavin monomers obtained in dilute solutions. Only in this case does the dichrograph register a curve of the linear dichroism spectrum that is different from the zero line. The parameters of the observed bands are given in Table 1.

Table 1. Energy parameters and angles of rotation of the plane of polarization of electronic bands, self-assembled molecules of complex riboflavin self-aggregates, obtained from the spectrum of linear dichroism.

| Legend of new bands | ν_{Max} | σ_c | φ_+ | φ_- |
|---------------------|-------------|------------------|---------------------------|---------------------------|
| | sm^{-1} | $\pm 100sm^{-1}$ | $\varphi \cdot 10^2 grad$ | $\varphi \cdot 10^2 grad$ |
| ν_{c_1} | 21700 | 1700 | 0.26 | |
| ν_{c_2} | 27800 | 2000 | 0.32 | |
| ν_{c_3} | 31000 | 2000 | | 0.22 |
| ν_{c_4} | 35000 | 3400 | 0.18 | |
| ν_{c_5} | 38500 | 3400 | | 0.16 |
| ν_{c_6} | 47800 | 3800 | 0.03 | |

Here ν_c is the numbering of electronic strips; ν_{max} is frequency corresponding to the maximum for concentrated solutions of riboflavin; σ_c is the half-width of the band $\varphi(+)$, $\varphi(-)$ and the positive and negative rotation angle of the plane of polarization, respectively.

The fact of the presence of "positive" and "negative" directions of the angle of rotation of the plane of polarization shows that the observed spectrum is the result of MMW in the form of exciton interaction, which manifests itself in the self-assembly of riboflavin molecules in concentrated aqueous solutions. In favor of this assumption, one can attribute the fact of observation of both short-wave and long-wave bands in the spectrum of linear dichroism [11-13].

From the analysis of the literature data it follows that the manifestation of the exciton interaction leads to a resonant splitting of the excited electronic state. Figure 4 shows the scheme of electronic transitions between the ground and excited states of riboflavin in a dilute (a) and concentrated (b) aqueous solution.

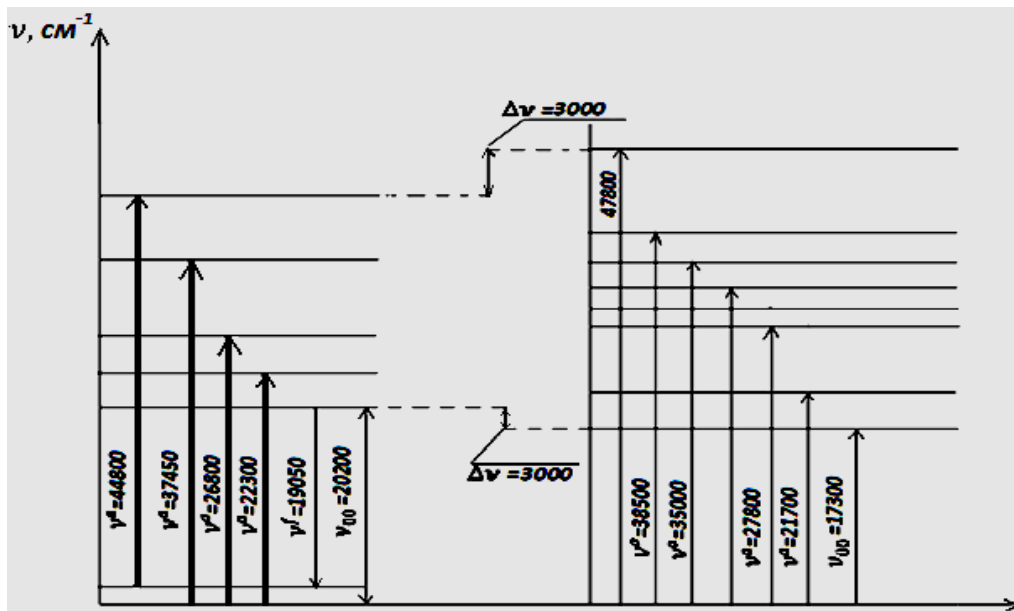


Fig.4. Scheme of frequencies of electron transitions of monomers (M) and self-aggregates ("a") of riboflavin molecules

From Fig. 4 it follows that, in fact, a resonant splitting of the excited electronic state of the vitamin preparation is observed in concentrated solutions. As can be seen from Fig. 4, the resonance expansion tips are $\Delta\nu = 3000 \text{ cm}^{-1}$ in electronic circuits, the line thickness indicates electronic transitions that appear in the absorption spectrum. In this case, the electronic transitions are correlated as a ratio of the optical densities. For the above scheme, we can write the following relations:

$$\Delta E_c = \Delta E + \Delta D + V_{1,2},$$

where ΔE_c and ΔE are the energy of the electronic transition for molecules in concentrated and dilute solutions, respectively.

ΔD is the difference between the energies of the interaction of excited and normal molecules.

$V_{1,2}$ is energy of excitonic interaction between molecules in a concentrated local volume of solvents.

The calculated values $V_{1,2}$ correspond to $\cong 1700 \text{ cm}^{-1}$, which is characteristic for inductive coupling. Apparently, under the action of this force, self-assembly of molecules is formed.

Conclusion

It is thus established that the molecules of riboflavin self-aggregates are formed under the action of Van der Waals forces and dipole-dipole interactions are most probable. It is determined that a strong inductive-inductive interaction also occurs in solutions of vitamin B₂ as a result of which the splitting of the excited electronic states of riboflavin occurs during their self-aggregation. It is shown that self-assembled molecules of the flavone derivative have a sufficiently high value of optical activity and possess linear dichroism.

Acknowledgment

This work was supported in part by a grant OT-A4-07, Uzbekistan

REFERENCES

- 1 Plato. *Selected dialogues*. - Moscow: AST, 2006, 512 p.
- 2 Lebedev-Stepanov P.V., Kadushnikov R.M., Molchanov S.P., Rubin N.I., Shturkin N.A., Alfimov M.V. Self-assembly of nanoparticles in the microvolume of colloidal solution: physics, modeling, and experiment. *Russian nanotechnologies*. 2011, No. 1-2, pp. 83.
- 3 Lebedev-Stepanov P.V., Kadushnikov R.M., Molchanov S.P., et al. Self-assembly of nanoparticles in a microvolume of a colloidal solution: physics, modeling, experiment. *Russian Nanotechnologies*. 2013, Vol. 8, No. 3-4, pp. 5 – 23.
- 4 Kakhharov A.M., Bakhrarov S.A., Makhmanov U.K., Ismailova O.B., Gafurov Sh.P., Kokkharova M.U. Study of the process of self-assembly of fullerene C₆₀ molecules in the binary mixture ETHANOL + BENZENE. *Proceeding of the Intern. Conference*. Samarkand, September 22-24, 2016, pp. 58.
- 5 Makhmanov U.K., Ismailova O.B., Kakhharov A.M., Bakhrarov S.A., Gafurov Sh.P., Kokkharova M.U. Self-organization of fullerene C₆₀ molecules in a binary mixture of ETHANOL + BENZENE". *Proceeding of the Intern. Conference*. Samarkand, September 22-24, 2016, pp. 59.
- 6 Gordon A., Ford R. *Sputnik chemist*. Moscow, Mir, 1976, 54 p. [in Russian]
- 7 Astanov S., Sharipov M.Z., Fayzullayev A.R., Kurtaliyev E.N., Nizomov N.N., et al. Spectroscopic study of photo and thermal destruction of riboflavin. *Journal of Structure*, 2014, Issue 1071, pp. 133 – 138.
- 8 Stewert J.J.P. Molecular structure matching by simulated annealing. I. A comparison between different cooling schedules. *Journal of Computer-Aided Molecular Design*. 1990, Vol. 4, pp. 295-330
- 9 Astanov S., Turdiyev M.R., Sharipov M.Z., Kurtaliyev E.N., Nizomov N.N. Effect of acidity of a medium on riboflavin photo destruction. *J. Russian Physics*, 2015, Vol. 58, 1 November
- 10 Astanov S., Prischepov A.S.. Optical-spectral characteristics of the associates, adsorbed on a vertical surface of colloidal solutions in terms of orienting action of the Earth gravity. *Opt.pectre.*, 1999, Vol. 71, No. 2, pp. 279 – 281.
- 11 Astanov S. *Photonics of molecules of food colorings*. Thesis for the degree of Doctor of Physical and Mathematical Sciences. Tashkent 2003, 53-55p.
- 12 Astanov S.Kh., Sharipov M.Sh., Fayzullaev A.R., Kurtaliyev E.N., Nizomov N.N. Thermal destruction of riboflavin in various aggregate states. *J. Applied Spectroscopy*, 2014, No. 1, p. 81.
- 13 Astanov S.Kh., Kosimova G.K., Turdiev M.R. Spectroscopic manifestations of the self-assembly of the food coloring of tartrazine. *Development of science and technology*. 2017, No. 3, pp. 93.

UDC 65.011.56

THE SAFETY ON A RAILWAY CROSSING BY MEANS OF SYSTEM OF VIDEO ANALYTICS

Amochaeva G.P., Seisenbaeva G.S., Mussina G.I.

E.A. Buketov Karaganda State University, Karaganda, Kazakhstan, gulsaya-19@mail.ru

In this article we describe the development of technical requirements and software for video analytics used at railway crossings in order to determine the stopped vehicles. The work describes the scheme of the video analytics system, working observing zones, graphical illustrations of the video analytics system and its components. The program described in the work defines the stopped vehicles at the crossing and gives a signal to obstructing traffic lights to stop the locomotive. There are times when the program gives out the raw data. The program defines vehicles, but the fight against false positives implies the use of additional technical means.

Keywords: system of video analytics, railway crossing, working zone of the crossing, technological zone, zone of floor inventory

Introduction

Today there are a lot of unprotected railway crossings. On these crossings there are a large number of road accidents, happening because of collision of the train with motor transport. Also there are no such technical means which would fix existence of hindrances for train driving and in case of detection automatically countercurrent traffic lights were switched on, thereby they would stop the train in advance. Development of such system is very actually. In our opinion, the system of video analytics can perform this function.

Proceeding from above, the purpose of the research is development of logic of a program shell for definition the hindrances to train driving.

For achievement of the set purpose it is necessary to solve the following problems which characterize the requirement to this system:

- a) detection of the stopped (blocked) motor transport in a working zone of traffic;
- b) detection of large-size fixed foreign objects in a working zone of traffic;
- c) detection of motor transport moving, ignoring the warning alarm system in a working zone of the crossing.

3. Object of the research

The main problem of the research was consideration the questions of construction the space-distributed hardware-software and algorithmically decentralized structure capable to process video images gradually, and calculation of the route for efficient data transmission on the network.

Object of the research of this work was creation of a security system which would trace the situation in a zone of monitoring the railway crossing.

The video system is intended for the automated definition of existence of hindrances to driving of railway transport in a working zone of the experienced zone of the operated railway crossing.

The video system is intended for functioning as a part of automated control system of the experienced zone of the operated railway crossing as a source of information on current state of a railway crossing [1]. The object is the experienced zone of the operated railway crossing including the crossing itself, the room of the person on duty on crossing and the adjacent territory (figure 1).

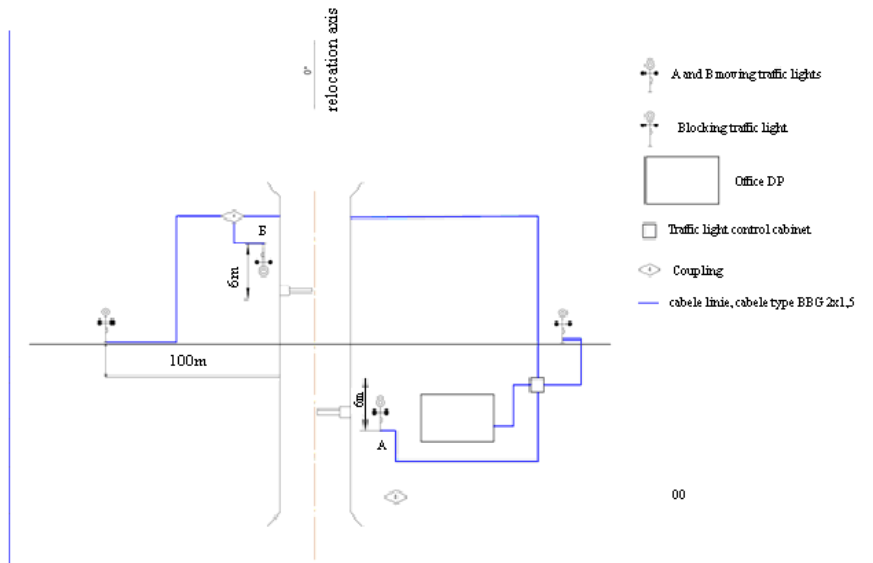


Fig.1. Cable scheme of system of video analytics on the crossing of 840 km

According to this scheme the system of video analytics traces motor transport passing through the railway crossing [2]. In case of motor transport stop on the crossing more than 180s, the system switches on countercurrent traffic lights for braking of the locomotive.

The system of video analytics consists of two server cases:

- server case 1, in this case power supply units of IP cameras and servers are installed (fig. 2);
- video server in complex with the automated workplace.

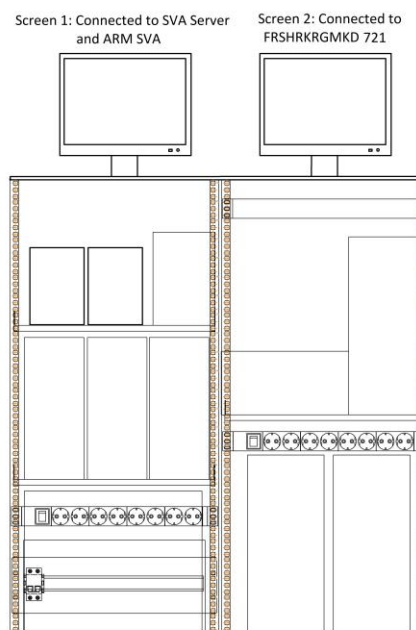


Fig. 2. Server cases

For the video system the following zones on the object are essential:

- a) working zone of the crossing – the open space limited by the lines going parallel to railway tracks from outer side on both sides of the crossing at the distance of 1 m from them and the lines

going parallel to the roadbed crossing railway tracks, also from outer side, on both sides at the distance of 1 m from roadbed;

b) zone of floor inventory of the existing system – the area before working zone including the barrier established at the moment and crossing traffic lights;

c) zone of floor inventory of experiment operation that is the open space located away from the working zone of the crossing and a zone of floor inventory of the existing system behind the room of the person on duty on crossing in which the inventory of the experienced zone is located;

d) technological zone that is a case with processing equipment of the control system of crossing and the territory, adjacent to it.

Data on the operation conditions and environment characteristics

Components of the video system are operated on the object in the following conditions:

a) the technical means which are external sources of data on the condition of railway crossing that are operated in the conditions of TBR1;

b) the technical means intended for the analysis of the entering data and also providing informational exchange that are operated in the class U4.1.

c) low illuminating intensity at night. Mainly, takes place on the sites remote from large settlements.

d) the number of the processed digital television video signals - not less than 4;

e) depth of storage of video series archive – not less than 300 hours of the continuous record on the canal;

e) quantity of alarm entrances – not less than 2;

g) quantity of alarm exits – not less than 3.

2. Requirements to characteristics of interrelations of the video system with interfacing systems and ways of information exchange.

The video system has to interact with dispatching remote workplace in automatic (sending messages and video data on the basis of logic of processing of video analytical events) and automated (sending results of inquiries, change of the condition of output signals according to the decision made by the dispatcher) the modes with use of network protocols of TCP/IP family [3].

For realization of the task it is offered to use the Bellman-Ford algorithm on finding of the shortest way in the column. The choice was made in its advantage since the Dijkstra algorithm though is more perfect, but is more difficult in realization and possesses huge disadvantage that is much more larger consumption of hardware at realization. Thus, the program will allow to use efficiently network resources, reducing the load of a network and to transfer information more quickly and efficiently [4, 5]. The logic of work of SVA is given in figure 3.

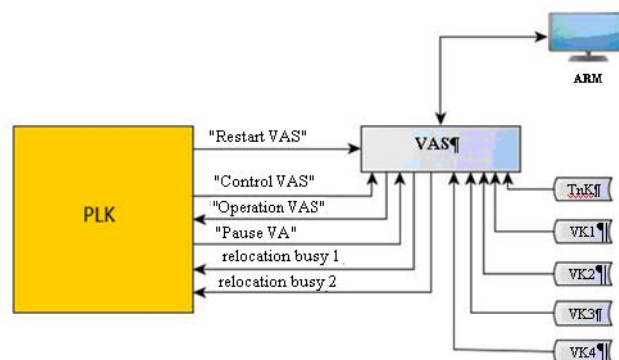


Fig. 3. Logic of VAS work

Results of definition the stopped motor transport on the crossing are given by video analytics in figure 4.

| Source | Event | Part | Additional information | Date | Time |
|---------------|-------------|------|------------------------|------------|----------|
| Pause BA | Closed | | | 21.02.2017 | 19:06:27 |
| Moving busv | Relay is on | | | 21.02.2017 | 19:06:27 |
| Pause BA | Open | | | 21.02.2017 | 19:06:42 |
| Pause BA | Closed | | | 21.02.2017 | 19:06:43 |
| Moving busv | Relay is on | | | 21.02.2017 | 19:06:43 |
| Pause BA | Open | | | 21.02.2017 | 19:07:56 |
| * Stop camera | Stopped car | | | 21.02.2017 | 19:15:08 |
| Pause BA | Closed | | | 21.02.2017 | 19:15:19 |
| Moving busv | Relay is on | | | 21.02.2017 | 19:15:20 |
| Pause BA | Open | | | 21.02.2017 | 19:16:59 |
| * Stop camera | Stopped car | | | 21.02.2017 | 19:18:40 |
| Moving busv | Relay is on | | | 21.02.2017 | 19:19:05 |
| Pause BA | Closed | | | 21.02.2017 | 19:19:45 |
| Moving busv | Relay is on | | | 21.02.2017 | 19:19:46 |
| Pause BA | Open | | | 21.02.2017 | 19:19:55 |
| Pause BA | Closed | | | 21.02.2017 | 19:30:08 |
| Moving busv | Relay is on | | | 21.02.2017 | 19:30:09 |
| Pause BA | Open | | | 21.02.2017 | 19:30:24 |
| Moving busv | Closed | | | 21.02.2017 | 19:37:12 |
| Pause BA | Relay is on | | | 21.02.2017 | 19:37:12 |
| Pause BA | open | | | 21.02.2017 | 19:38:04 |



Fig.4. Fixing motor transport video analytics

Conclusion

This article researched hardware and software tools for analyzing video objects and made their selection from the DSSL nomenclature for organizing an adaptive decentralized complex of visual identification of vehicles at the crossing and their movements with the functions of autonomous intellectual image processing. The created program can be integrated into existing video monitoring systems for the most optimal use and speed of data transmission, as well as reducing the load from

networks. Methods are proposed, an algorithm and software implementation of the mechanism of dynamic tuning (adaptation) of the structure of the complex optimizing it in terms of the number of computing resources used and an effective way of transmitting information for solving the current task of identification are developed.

By results of work it is possible to draw conclusions that the offered approach and the created program of formation of a complex of means of the video analysis, can be used in practice when the organization and functioning the composite distributed systems of the video analysis of objects since the program allows to use most efficiently resources of the network and to considerably reduce the loading level.

REFERENCES

- 1 Grib S. M. *Model of thinking*. Moscow, Neuron, 2003, 175 p. [in Russian]
- 2 Official site of the ISS company. Available at: <http://www.iss.ru> [in Russian]
- 3 Skorokhodov A.P. "*Face-Intellect*" - *identification of the person on image*. Moscow, ITV, 2006, 75 p. [in Russian]
- 4 Maklakov S. V. *BPWin and ERWin. CASE development tools of intelligence systems*. Moscow, Dialogue MIFI, 1999, 255 p. [in Russian]
- 5 Reference book on SKUD. Available at: <http://www.kardmaster.ru> [in Russian]

Article accepted for publication 24.01.2018

UDC 621.039.533.6, 621.351

OBTAINING OF POROUS NICKEL ANODE BY HOT PRESSING AND ETCHING METHODS FOR SOLID OXIDE FUEL CELL APPLICATION

Umirzakov A.G., Mereke A.L., Rakmetov B.A., Beisenov R.E., Muratov D.A.

Laboratory of electron paramagnetic resonance spectroscopy after Y.V. Gorelkin, LLP 'Institute of Physics and Technology', 11 Ibragimova str., Almaty, Kazakhstan, info@sci.kz

The work represents a simple fabrication method of a porous nickel anode for thin film solid oxide fuel cells. The porous nickel anode is fabricated using a metal/pore-former mixing method with different ratios of powder followed by pressing and heat treatment. The process of obtaining a porous nickel anode by pressing of nickel and aluminum powders is shown. Further sintering of the samples and etching of aluminum from the obtained anode structure. The electrolyte layer was sputtered by pulsed laser deposition. Scanning electron microscope and energy-dispersive X-ray spectroscopy analysis are represented in article.

Keywords: thin-film solid oxide fuel cells, porous anode, electrochemical etching, electrolyte, pulsed laser deposition.

Introduction

Solid oxide fuel cells (SOFCs) have the potential to be one of the cleanest and most efficient energy technologies for direct conversion of chemical fuels to electricity. Economically competitive SOFC systems appear poised for commercialization, but widespread market penetration will require continuous innovation of materials and fabrication processes to enhance system lifetime and reduce cost [1].

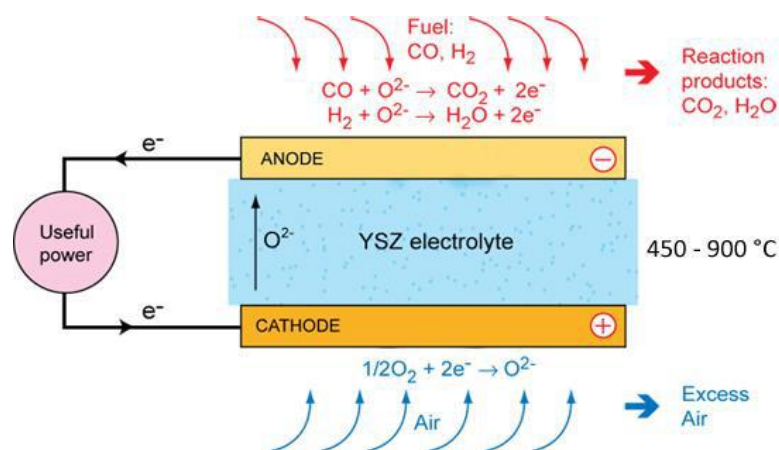


Fig.1. Scheme of an SOFC illustrating also the working principle

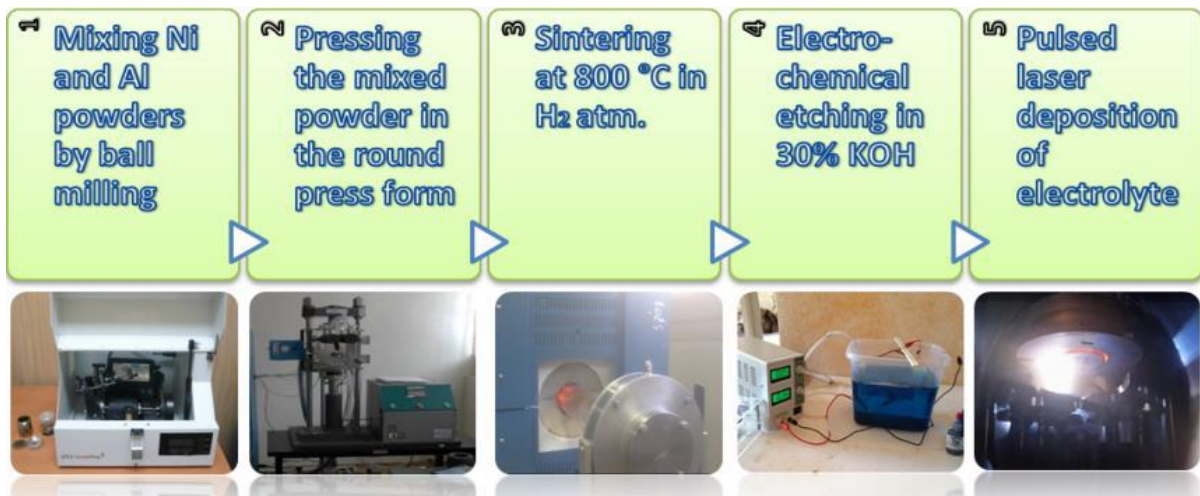
SOFCs convert chemical energy with high efficiency directly into electricity and heat. It can operate on a variety of fuels such as natural gas or hydrogen [2]. As shown in figure 1, the fuel supplying H_2 is fed into the anode compartment where it is oxidized, and the electrons released as a result are conducted to an external circuit [3, 7]. The reaction products on the anode side of an SOFC are mainly water and CO_2 . Air enters on the cathode side and oxygen is reduced here to O^{2-} by reaction with electrons from the external circuit. The O^{2-} ions can travel through the ion-conducting and gas-tight electrolyte, which separates the anode compartment from the cathode compartment [4]. Once on the anode side the O^{2-} joins with hydrogen to form water. Open circuit

voltage (OCV) is the voltage obtained at zero current that ranges from about 0.8–1.1V and is a measure for the gas leakage or electronic leakage through the electrolyte [5, 6].

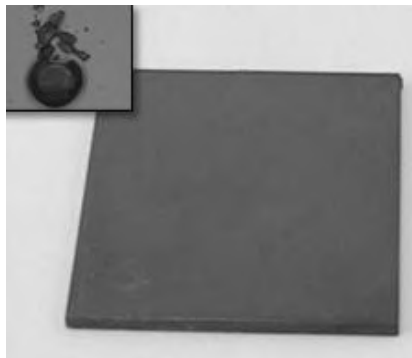
1. Experimental technique

The porous nickel anode is fabricated using a Ni and Al powders mixing method followed by pressing and heat treatment. Very pure Ni and Al powders of 99.99% purity were used in the work. The percentage of Ni and Al components is 60: 40%. The anode basis possesses a high porosity which is required for efficient delivery of fuel to the cell. Hot pressing method was used for obtaining tablet from nickel and aluminum powders. Next two steps was sintering of the sample and etching out aluminum from the anode structure. The mixing and grinding of the smallest powder with uniform dispersion is achieved by means of a grinding process in a SPEX Sample Pre 8000M ball mill with carbide tungsten cylinders with a 5 mm ball diameter.

Full experimental process of fabrication a porous nickel anode with a flat nanoporous surface shown in figure 2a, by thoroughly mixing commercial nickel powder (particle size between 0,5-1 μ m) with an aluminum (particle size of from 100 to 300 nm) proppant. The mixing of the two components must be thorough; therefore, it is typically performed by mechanical mixing and ball milling procedures. The resulting mixture (nickel powder and proppant) is then pressed into a parallel faced \approx 1 mm thick square tablet at 5000 psi (see figure 2b). The tablets pressed into round shape form as shown in insert of figure 2b. The tablet of pressed nickel powder/proppant is then loaded into a high temperature tubular furnace and sintered at 800 °C for 2 h in an ambient hydrogen atmosphere.



a)



(b)

Fig.2. Schematic diagram for the porous nickel anode fabrication process (a);
The fabricated porous nickel anode 10x10 mm (b).

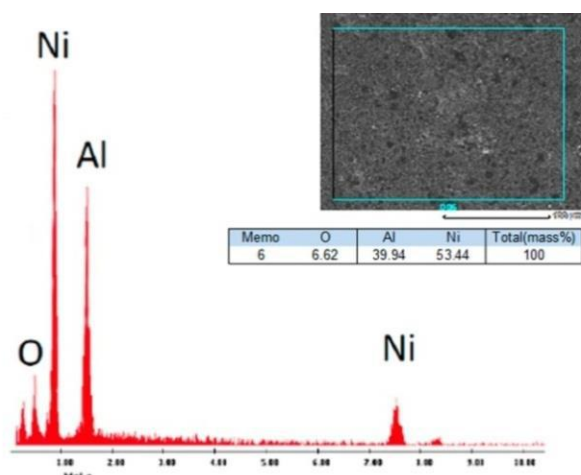


Fig.3. EDS analysis of anode after sintering

Next step of research was electrochemical dealloying of aluminum from the alloy of Ni-Al powders, as the potential increased, the amount of etched Al also increased. Passivation of nickel occurs with an increase in time, which contributes to the formation of NiO. The etching was carried out in a 30% KOH solution at room temperature. The process was carried out in two electrode cells, and under the action of ultrasound. A sample of Ni-Al alloy is used as a working electrode.

2. Results and discussion

Surface SEM images were carried out for the fabricated porous nickel anode after sintering (figure 4a, b). These images show clearly the surface and bulk porous structure of the nickel anode, with pore sizes of 100 nm – 1 μm.

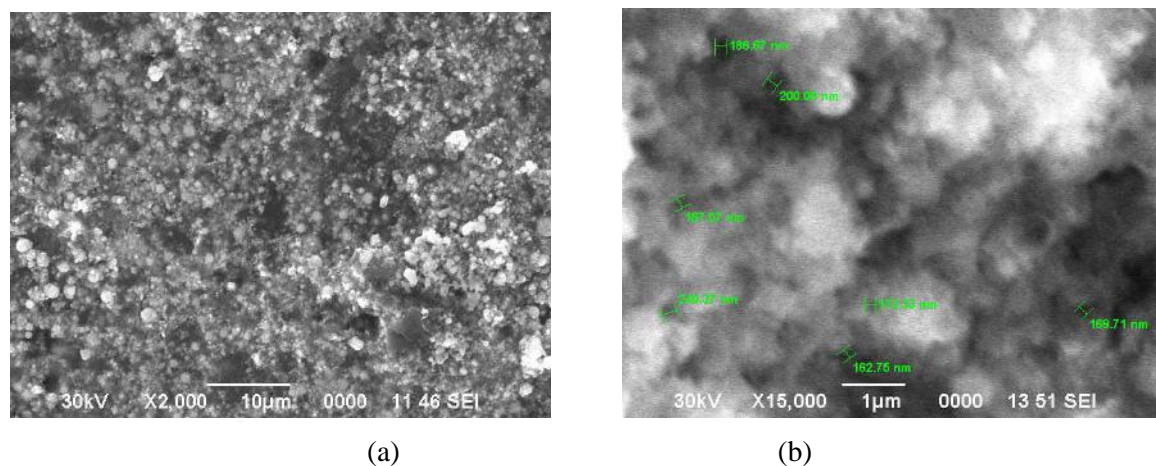


Fig.4. SEM images of the fabricated porous nickel anode: a) anode surface directly after sintering at 800 °C for 2 h.; b) anode surface after electrochemical etching.

This large pore size allows the fuel to readily reach the anode/electrolyte interface. The nickel surface treatments were applied to produce not only a flat surface, but also a surface with small pores (size < 500 nm) (see figure 5a, b) such that a continuous thin film electrolyte could be deposited and exhibit both gas and electrical hermeticity. The now smooth surface of the fabricated nickel anode will permit the deposition of a 3 μm thick smooth, continuous electrolyte yttria-stabilized zirconia (YSZ) film, which is not only an electrolyte layer, but one that effectively blocks hydrogen from reaching the SOFC cathode.

Figure 3 shows the EDS analysis of the sample immediately after the annealing process in the tubular vacuum furnace. EDX analysis shows the correct ratio of components 60:40, which was originally set for the anode material.

The content of ~ 40% of aluminum compared with nickel makes it possible to vary the porosity due to a change in the concentration of the main component of nickel, but also it is impossible to forget the strength after etching. The dimensional content of aluminum can destroy the sample during electrochemical etching.

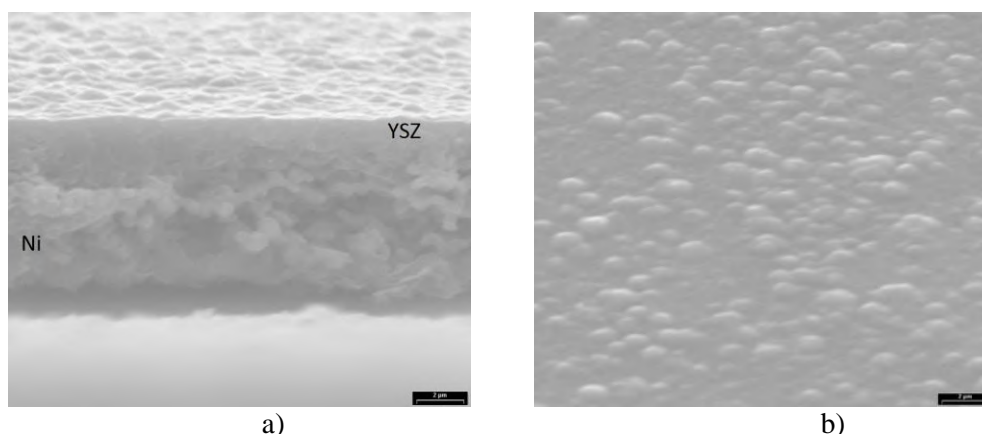


Fig.5. SEM cross-section images of the fabricated porous nickel anode with electrolyte layer, a) Anode cross-section after electrolyte deposition b) Electrolyte surface after deposition.

A 248 nm KrF Excimer laser at 7 Hz and 380 mJ was used to deposit the electrolyte layer on the porous nickel anode surface [2]. In this work, a dense YSZ electrolyte layer (about 1-2 μm thick) deposited at 150 mTorr and 650 $^{\circ}\text{C}$ in an atmosphere of 96% argon, 4% hydrogen to avoid nickel oxidation. Surface and cross-sectional SEM images were carried out for the fabricated porous nickel anode after pulsed laser deposition (figure 5a, b). As we can see from images the deposition of a thin (0.5–3 μm), smooth, and pore free electrolyte will not allow the diffusion of both fuel and air.

Conclusion

The porous nickel anode obtained by process of pressing nickel and aluminum powders, sintering and etching of aluminum from the obtained anode structure. The pore size between 100 – 500 nm, which allows for the H_2 to passage thru the anode to YSZ electrolyte layer. The thin YSZ electrolyte layer is sputtered by pulsed laser deposition. SEM and EDS analysis were obtained. Analysis shows the deposition of a thin (0.5–3 μm), smooth, and pore free electrolyte which will not allow the diffusion of both fuel and air. EDS analysis shows the correct ratio of the material after annealing in the furnace at 800 $^{\circ}\text{C}$, the presence of oxygen due to the interactions after discharge from the furnace.

Acknowledgment

The research was carried out within the framework of the grant of the Science Foundation of the Republic of Kazakhstan No.0115PK01908 in the direction “Energy & Machinery Engineering”.

REFERENCES

- 1 Singhal S.C., Kendall K. *High Temperature Solid Oxide Fuel Cells: Fundamentals, Design and Applications*. Elsevier Advanced Technology, Oxford, UK, 2003, 406p.
- 2 Ebrahim R., Yeleuov M., Ignatiev A. 3D Porous Nickel Anode for Low Temperature Thin Solid Oxide Fuel Cell Applications. *Advanced Materials Technologies*, 2017, pp. 1-5
- 3 Fergus B., Jeffrey W. Oxide anode materials for solid oxide fuel cells. *Solid State Ionics*, 2006, Vol.177 (17-18), pp. 1529 – 1541.
- 4 Agarwal M., Kumar V., Malladi S., Balasubramaniam R. and Balani K. Effect of current density on the pulsed co-electrodeposition of nanocrystalline nickel-copper alloys. *JOM*, 2010, Vol.62, No. 6, pp.88-92.
- 5 Lipilin AS, Neumin AD, Paluev SF Investigation of hydrogen electrodes made by hot pressing in circuits with oxide solid electrolyte. *IB "PPTEEE and TE"*. 1975, Issue 2 (64), pp. 69 – 81.
- 6 Korovin N.V. *Fuel cells and electrochemical power plants*. Moscow, MPEI, 2005, 280 p.
- 7 Lynd L.R., Cushman J.H., Nichols R.J., Wyman C.E. Fuel ethanol from cellulosic biomass. *Science*, 1991, Vol. 25, pp. 1318 – 1323.

UDC 638.21.4

AUTONOMOUS BIOGAS INSTALLATION WITH SOLAR HEATING SYSTEM

Komilov O.S., Sharipov M.Z., Tilloev L.I., Majidov J.A.

Bukhara Engineering - Technologies Institute, Bukhara, Uzbekistan, m.z.sharipov@rambler.ru

An experimental production biogas plant based on solar heating has been designed and built. Its structural scheme and results of calculations of parameters of a biogas plant are given based on the statistical data of Uzbekistan on the availability of biogas and solar energy potential. So, results of experimental researches on biogas production at mesophilic mode of plant operation are given. Possibilities of using biogas plants with heating fermented biomass at the expense of renewable energy sources in conditions of small consumer farms are considered.

Keywords: Biogas plant, energy saving, ecology, collector, solar heating, heat storage.

Introduction

At present, economically developed and developing countries are accelerating the development of practical use of alternative energy sources as an important factor for sustainable development and to increasing the competitiveness of economies in the face of a reduction in the world's hydrocarbon reserves [1]. In Uzbekistan, considerable experience has been accumulated in carrying out scientific and experimental research in the field of the use of alternative energy sources, primarily solar and biogas energy, for which development has been carried out for many decades [2].

Currently, a large number of biogas plants have been developed and are functioning from organic waste in various countries. However, most scientifically-based biogas plants are designed for waste treatment of large livestock complexes and provide for heating the fermented biomass by using electricity or heat from centralized networks, which hinders the efficient utilization of waste from individual and small farms dispersed in regions without a centralized power supply [3, 4].

On the other hand, the change in the structure of agricultural production in connection with the transition to market conditions has led to an increase in the number of private dehqan and farmer households. In solving energy supply problems, individual and farming enterprises in remote areas of Uzbekistan that do not have centralized electricity and gas supply are in need of imported fuel materials [5].

Therefore, the development of autonomous bioenergy plants with heating of fermented biomass at the expense of local renewable energy sources is an urgent problem, the solution of which contributes to the direction of effective utilization of waste with ensuring environmental safety in the agricultural production of hard-to-reach regions. All this dictates that for large-scale use of biogas plants in farm and individual farming, above all, given their regional and local conditions, the need to develop small energy-efficient, economical, environmentally friendly and high-performance biogas plants (BGP) [6].

4. The experimental procedure and the experimental setup

In this connection, an experimental biogas plant of industrial character with a solar heating system (Figure 1), consisting of a bioreactor (1), a solar water heater (2), a heat accumulator (3), a gas scrubber (4) and a gas storage tank (gas holder) (5). In the manufacture of these parts, we proceeded from the requirements of resource conservation, the environment and their expected effectiveness.

Solar water heating collectors (SWC) of various designs are traditionally made of metal materials. The SWC offered by us is made of alternative non-metallic materials. Solar water heater

made in the form of a "hot box", inside of which a heat collector is made of a plastic pipe of black color, a collector with inlet and outlet nozzles.

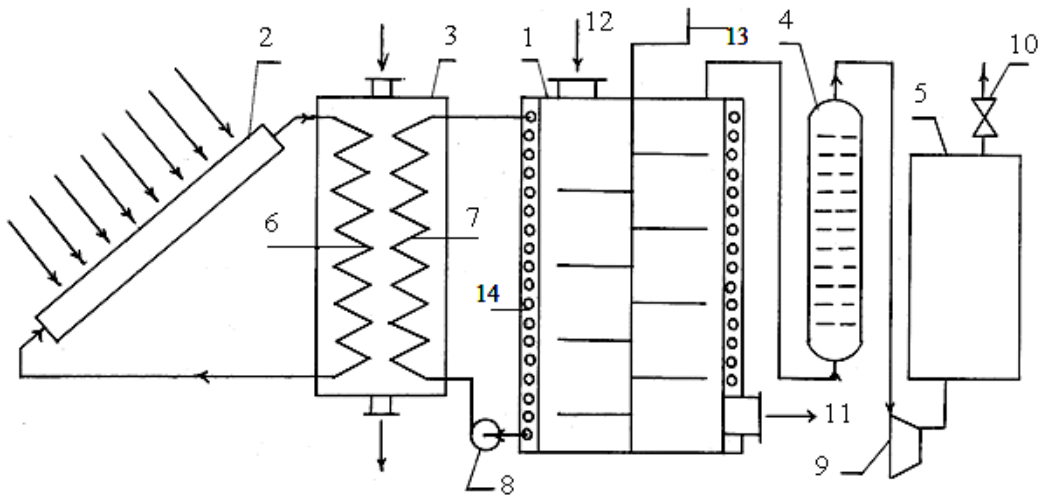


Fig.1. Schematic diagram of an experimental-production biogas plant with a solar heating system.

The heat-storage part is a well-insulated (from the outside) cylindrical container (3), inside which there are two heat exchangers - one (6) for heating the heat-storage material (HSM), and the other (7) provides heat to the bioreactor. Both heat exchangers are made of plastic pipes in the form of a coil. The capacity is filled with HSM, as which we used hexahydrate calcium chloride ($\text{CaCl}_2 \cdot 6\text{H}_2\text{O}$) with a melting point almost equal to the optimum temperature of the mesophilic regime of the fermentable substrate ($36\text{--}39^\circ\text{C}$). The heat of fusion and the density of crystalline hydrate are, respectively, 174.4 kJ / kg and 1634 kg / m^3 .

One of the main elements of the BGP is a bioreactor, which is a hermetically sealed cylindrical vessel with a diameter of 1.5 m and a height of 2 m ($V = 3.5$ cubic meters).

In the upper and lower side parts, loading (12) and unloading (11) hatches are provided. Inside the reactor, a mechanism (13) is placed in the middle for mixing the fermentable substrate. On the outside of the cylinder, the container is densely (in height) surrounded by plastic pipes serving as heating elements (14) and on which a metal wire is stretched. Further, the reactor is thermally insulated from the environment by mineral wool, the thickness of which is 10 cm.

In order to obtain the temperature necessary for the fermentation process and, if possible, to keep it constant, it is necessary first of all to heat the substrate supplied to the reactor to the desired temperature; also constant, supplying heat to compensate for heat losses.

The heating of the fermentable substrate to the temperature of the mesophilic regime ($t = 35\text{--}38^\circ\text{C}$) and the maintenance of this temperature in the bioenergetic system developed by us is carried out with the help of a helium heater. Heat production is carried out as follows: during the day, the sun's rays passing through the transparent enclosure heat the water collector. The heated water from the collector enters the heat storage reservoir and passes through the heat exchanger (6) and also gives its significant HSM potential, again it enters the collector. This happens in the daytime in clear sunny weather. And in the heat-storage part, since we chose as the HSM the $\text{CaCl}_2 \cdot 6\text{H}_2\text{O}$, thermal processes occur differently. With the arrival of heat from the solar collector, the crystalline hydrate begins to heat up, its temperature rises until it reaches the melting point, i.e. $36\text{--}39^\circ\text{C}$. Further, excess heat is accumulated due to the phase transformation of crystalline hydrate. Thus, in the heat accumulator proposed by us, the temperature is kept constant, i.e. equal to the optimum temperature of the mesophilic regime of the fermentable substrate. At night, the installation

operates due to the heat accumulated during the day (the heat of the crystal hydrate transition of $\text{CaCl}_2 \cdot 6\text{H}_2\text{O}$), thus ensuring 24-hour operation and increasing the efficiency of the bioenergy plant.

Heating of the bioreactor and, consequently, of the fermentable substrate is carried out through a sealed water heating system containing a heat exchanger (7), a water pump (8) and heat exchangers (14) in the form of spirally wound on the outside of the reactor, through which the coolant (water) circulates.

5. Experimental results

Our experiments showed that the proposed biogas plant, whose volume is 3.5 m^3 , is able to process 90 kg of manure per day in the mesophilic regime and produce about 20 m^3 of biogas and slightly less than 90 kg of liquid ecologically clean biofertilizers. The latter contain a number of organic substances that contribute to increasing the permeability and hygroscopicity of the soil, while at the same time preventing erosion and improving general soil conditions. Organic substances are also the basis for the development of microorganisms that transfer nutrients into a form that can easily be assimilated by plants. The results of parallel practical studies on growing a tomato in a helio-greenhouse showed that the yield of tomato when using biofertilizers increased by 40-50%.

To study the temperature and thermal regimes, as well as the capacity of the plant with respect to the biogas produced, we conducted a series of experiments with various substrates in various meteorological conditions. The results of such experiments are shown in Fig. 2.

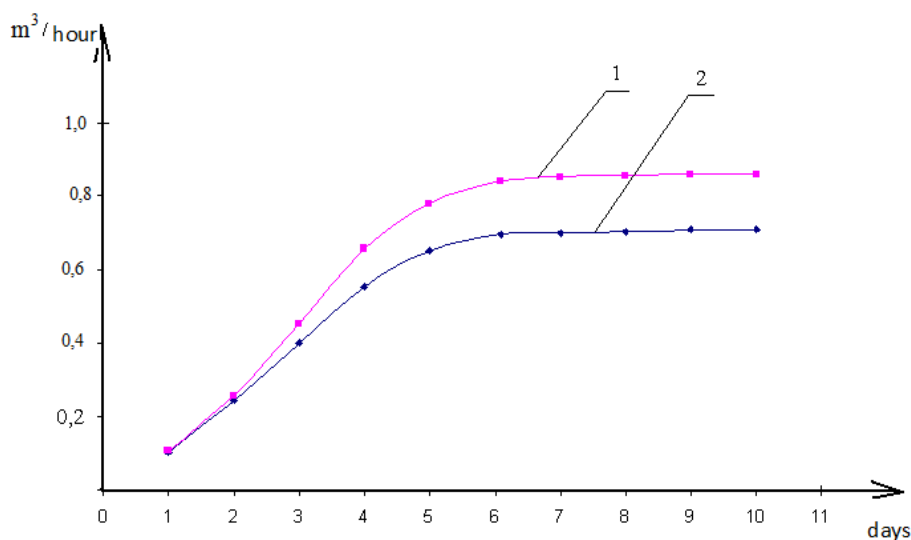


Fig.2. The results of the experimental studies on the release of biogas with various substrates:
1 - chicken litter; 2 - manure of cattle.

The experiments showed that under the mesophilic mode of operation of the bioreactor, the gas productivity practically did not decrease with a temperature deviation of $1-2 \text{ }^{\circ}\text{C}$ from the optimum and the substrate fermentation process lasted -25-30 days.

In the course of the study, it was found that the intensity of the process depends largely on the temperature and humidity in the bioreactor. It is shown that during the mesophilic regime ($36-38^{\circ}\text{C}$), the process of methane fermentation proceeds more intensively, as evidenced by a greater yield of biogas and a higher content of methane in it.

Conclusion

The conducted researches allow to develop the technology of processing chicken manure (and also other organic wastes), which is the most promising in terms of protecting the environment and the environment of non-renewable natural energy sources. The use of this technology will make it possible to make full use of the energy and raw materials potentials contained in organic waste.

The obtained results allow calculating the parameters of a biogas plant taking into account local biomass resources and using this energy to save fuel and electricity fuel, to obtain high-quality fertilizer and, thus, to exclude dependence on imported energy carriers and improve the environmental performance of the republic.

Also, long-term field trials of the proposed design of the biogas plant were conducted, as a result of which its autonomous working capacity was revealed in the climatic conditions of the Bukhara region.

REFERENCES

- 1 Martinot E. *Renewables 2015*. Global Status Report, World watch institute. 2015. Available at: http://www.ren21.net/wp-content/uploads/2015/07/REN12-GSR2015_Onlinebook_low1.pdf
- 2 Decree of the President of the Republic of Uzbekistan "On measures for the further development of alternative energy sources". *Collection of legislation of the Republic of Uzbekistan*. 2013, No. 10, 124 p.
- 3 Renewable Energy Policy Network, 2010, «Energy for Development: The Potential Role of Renewable Energy in Meeting the Millennium Development Goals» Washington, DC, World watch institute.
- 2 Birkin S.M. *Improvement of technology and technical means of utilization of cattle manure*. Abstract diss. Volgograd State University of architecture and civil engineering, Volgograd, 2009, 24 p. [in Russian]
- 4 Rakhmatov B.F. Liquid waste processing in a biogas unit. *Heliotechnics*. 2007, No. 3, pp. 101 – 105.
- 3 Osmonov O.M. *Scientific and technical foundations for the creation of autonomous bioenergy plants for krestyan farms in the mountainous regions of Kyrgyzstan*. Abstract diss. Moscow State Agroengineering University named after V.Goryachkin, Moscow. 2012, 36 p. [in Russian]

UDC 536.248

DEVELOPMENT OF ENERGY-SAVING VENTILATION SYSTEM FOR AGRICULTURAL BUILDINGS

Issakhanov M.Zh., Sakipova Sh.E., Alibek N., Dyusenbaev T.V.

Kazakh National Agrarian University, Almaty, Kazakhstan, sholpa_1@mail.ru

The article discusses the results of development of energy efficient ventilation system of sheepfold. The scheme of the experimental energy-efficient ventilation system of sheepfold is given. The differential equations of heat transfer for describing the temperature field in the soil around the duct of the ventilation system of the sheepfish are used. An example of calculation of dimensionless criteria at given initial and boundary conditions is shown. The values of the air temperature at the outlet of the channel and the value of the heat flux are determined. The results of the calculations are consistent with the test data using information and measuring system for remote recording of the thermal characteristics of ventilation systems.

Keywords: ventilation system, sheepfold, ductwork, temperature field in the soil, heat transfer, heat flux.

Introduction

Rational using of fuel and energy resources is one of the global problems. One promising solution to this problem is the use of new energy-saving technologies, using renewable energy sources. The range of renewable energy on farms is quite broad: it is heating or cooling buildings, and drying of agricultural products, and desalination and water heating, and even autonomous power supply. The advantages of the energy sources are environmental friendliness and low cost of labor and funds for the operation of facilities for their use. The solution of the problem in the energy-saving ventilation systems of agricultural buildings is the effective use of low-grade soil heat. The ground surface layers of the Earth, actually is a heat accumulator of unlimited capacity, which thermal regime is formed by the action of solar radiation. Low-grade heat of the Earth can be used in agricultural buildings for heating, hot water, air-conditioning (air-cooling). There are a number of examples of the use of soil heat for heating and cooling of livestock buildings through underground air conduits and heat exchangers. They are allowed to save from 50 to 75% of the costs for heating and cooling the buildings. [1-4]. Studying these examples allowed to develop energy-saving ventilation system for sheep premises [5, 6].

1. Ventilation system

Functional block diagram of the ventilation system (Fig. 1) contains the intake shaft 1 and 2 provided with a fan motor 3 and water spray 4, exhaust shaft 5 with control valve 6 and air supply ducts 7,8 with control valves 9, outlets in air 10-ventilated room with a 11-coil temperature of 12 linked via the intake 13 air shutter shaft 1 and placed in the soil below the freezing and the latter program controller 14 microclimate temperature sensors 16, 17, 19, 20 and 15 velocity, humidity 18 connected to the fan motor 3 control valve 6 2 9 exhaust shafts and air intakes to 7, 8 and 4, and the atomizer coil units 12 temperature.

The device contains two air-supply ducts 7, 8 to ensure continuity of supply of heated air into the room 11 during charging one of them. Assembly and manufacture of air handling unit is made from prefabricated modular elements, designed to suit the required volume of ventilation air and the type of agricultural premises. In a cold season the heavy gravity fresh air enters the intake shaft 1 and through air shutter 13 enters the outdoor air duct 7 contacts with the surface of the walls, is heated with the warmth of a soil and moves up, goes through 10 outlets in room 11, flowing

temperature closer 12. Air shutter 13 threshold, which is located below the bottom of the duct 7, 8 does not allow exit easily of the heated air from the air in the intake shaft 1. Thereby it provides a strictly unilateral movement gravity flow of fresh air. Exit from the ventilated room of the exhaust air through the exhaust shaft 5 with a control valve 6, which is controlled by software regulator microclimate 14. Program controller 14 controls operation of the electric motor 3 of the fan 2 which supports the set speed of a self-flowing stream and adjusting valves 9, stitched air ducts 7, 8, providing the set threshold of temperature of a self-flowing stream, and also temperature closer.

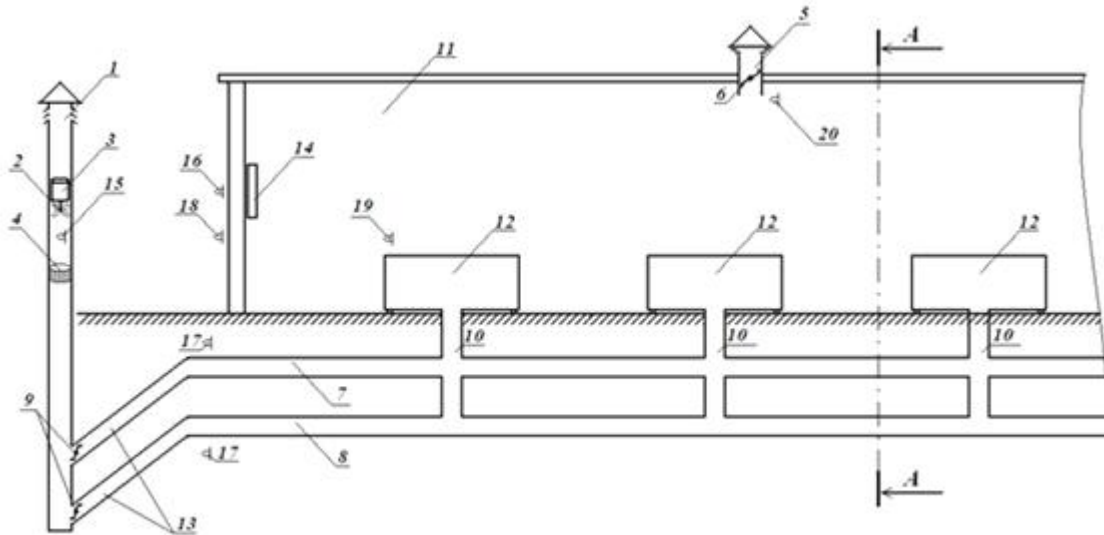


Fig.1. Scheme of ventilation device.

As the temperature of the walls of the duct 7 or soil mass reduces the intensity of heat removal and at a certain temperature the threshold exceeds a specified value. At this point, the temperature sensor signal ground 17 climate control 14 closes the control valve air supply duct 7 and opens the valve 8. An array of ground round duct 7 after a while restores its natural temperature, i.e. recharges, and the array of soil around the duct 8 is cooled, i.e. discharges. Upon reaching the ground temperature values are normalized by the sensor 17, the controller 14 closes the valve 9 microclimate supply duct 8 and 9 opens the valve duct 7. Thus, blowing ducts alternately operate in the mode of charging and discharging, provides normalized stable supply air temperature, i.e. stabilizing the temperature of the supply air. Enter the room heated inlet air temperature 12 wraps closer, increases its temperature to the rated value. Enable or disable the controller 14 performs closers microclimate by temperature sensor 19. 12 closers provide radiant and convective heat transfer in the process of creating a local microclimate. Valve 6 of exhaust shaft 5 regulates the exit of the exhaust air; its work is controlled by the regulator of microclimate 14 through the temperature sensor 20.

As the internal temperature rises gravity flow velocity decreases and at a certain temperature, the flow rate will be insufficient to provide the rated air. At this point, the signal sensor 16, the outdoor temperature sensor 15 and a flow rate regulator 14 connects the electric motor 3 microclimate fan 2.

In a warm season, heated fresh air by fan (2) is injected at the intake shaft (1) to the duct (7), from where (10) through off takes air enters the ventilated room. When passing through the air duct (7) the heated fresh air is cooled by transferring heat to ground through its walls. Ducts (7, 8) will also run in both the charging and discharging as during a cold season. Depending on the desired humidity parameters of ventilated fresh air moisturize with water through the gun (4). Sprayer (4) is operated by the regulator (14) of microclimate through the humidity sensor (18) outside air and provides the required humidity of supplied air. Under this scheme, designed and built experimental

energy-saving ventilation system for the sheepfold and conducted production tests during the lambing.

Within the framework of the problem statement, an experimental energy-saving ventilation system for the sheep-dog was developed and constructed and production tests for the time of lambs litter were carried out and its calculations were performed.

2. Calculation parameters of sheepfold ventilation system

For designing the energy saving ventilation system, was viewed the differential equation of the temperature field of soil around the ductwork of ventilation system

$$\frac{\partial t}{\partial \tau} = a \left(\frac{\partial^2 t}{\partial R^2} + \frac{1}{R} \frac{\partial t}{\partial R} \right) \quad (1)$$

where a - temperature conductivity of the soil.

The boundary conditions for equation (1):

$$t = t_{soil} \quad \text{at} \quad \tau = 0; \quad R \rightarrow \infty, \quad \tau \geq 0; \quad -\lambda \frac{\partial t}{\partial R} = \alpha [t(R_o, \tau) - t_{aver}(\tau)] = 0 \quad (2)$$

where λ is the temperature conductivity of the soil;

α - heat transfer coefficient of the channel walls.

The value of integral air temperature along the channel length with the total area of heat transfer F :

$$t_{aver}(\tau) = \frac{1}{F} \int_0^F t(x, \tau) dF \quad (3)$$

where $t(x, \tau)$ -is local temperatures determined from the heat balance equation duct area dF :

$$cGdt = \alpha [t(R_o, \tau) - t(x, \tau)] dF \quad (4)$$

The solution of the equation (2) has the form:

$$\varphi_x = \frac{t(x, \tau) - t(R_o, \tau)}{t_0 - t(R_o, \tau)} = \exp\left(\frac{-\alpha F_x}{cG}\right) \quad (5)$$

where $t(R_o, \tau)$ - is the average temperature over the length of the channel walls at a given moment of time; F_x - the area of heat exchange of channel through section x .

The solution of the differential equation (5) allows calculate the thermal technical parameters of the energy-saving system [1, 2].

Let's calculate the thermal engineering parameters of the ventilation system at the following initial data:

$D_o = 0.22m$, $L = 12m$ - are the diameter and the length of the air duct;

$t_{soil} = +10^\circ C$ - is the initial uniform temperature of the soil;

$a_{soil} = 5.2 \cdot 10^{-7} m^2 / s$ - is the coefficient of soil temperature-conductivity;

$\lambda_{soil} = 1.3 W / (m^2 \cdot ^\circ C)$ - is the coefficient of thermal conductivity of the soil;

$\rho_{soil} = 1700 kg / m^3$ and $c_{soil} = 1.47 kJ / (kg \cdot ^\circ C)$ -are the density and the specific heat of soil;

$t_{out-air} = t_o = -16^\circ C$ - is the estimated ventilation or the temperature of the incoming outside air;

$t_{aver} = -5^\circ C$ - is the average temperature of the heating period;

$n = 198 days$ - is the duration of the heating season;

$\mathcal{G} = 2m / s$ - is the speed of air flow;

$\nu_{air} = 12.42 \cdot 10^{-6} m^2 / s$ - is the kinematic viscosity of air;

$\lambda_{air} = 0.0253 W / (m^2 \cdot ^\circ C)$ - is the coefficient of kinematic heat conductivity of air;

$a_{air} = 17.44 \cdot 10^{-6} m^2 / s$ - is the coefficient of kinematic air temperature-conductivity;

Then the Prandtl criterion equals $Pr = \frac{\nu_{air}}{a_{air}} = \frac{12.42 \cdot 10^{-6}}{17.44 \cdot 10^{-6}} = 0.71$

It is possible to calculate the length of the air duct based on condition: $St' = 2$.

We have from the next formula:

$$L = \frac{R_0 \cdot Re \cdot Pr}{Nu} \quad \text{that} \quad L = \frac{R_0 \cdot Re \cdot Pr}{Nu} = \frac{0.11 \cdot 35427 \cdot 0.71}{78.48} = 35.35m$$

The maximum operating time of the air duct is determined from the next condition $Bi'' \sqrt{Fo} = 1$:

$$Bi'' = Bi' + 0.375 \quad \text{and} \quad Bi' = \bar{\varphi} \cdot Bi$$

$$\bar{\varphi} = \frac{1 - \exp(-St')}{St'} = \frac{1 - e^{-2}}{2} = 0.43$$

$$Bi = \frac{\alpha \cdot R_0}{\lambda_{soil}} = \frac{9.02 \cdot 0.11}{1.3} = 0.76$$

$$Bi' = \bar{\varphi} \cdot Bi = 0.43 \cdot 0.76 = 0.33$$

$$Bi'' = Bi' + 0.375 = 0.33 + 0.375 = 0.705$$

$$\tau = \frac{R_0^2}{(Bi'')^2 \cdot a_{ep}} = \frac{(0.11)^2}{(0.705)^2 \cdot 5.2 \cdot 10^{-7}} = 46817 = 13 \text{hours}$$

The air temperature at the outlet of the duct is equal to

$$t_L = t_0 + \bar{\varphi} \cdot St' \cdot \theta_w \cdot (t_{soil} - t_0)$$

$$\varphi_L = \frac{t(L, t) - t_0}{t_{soil} - t_0} = \bar{\varphi} \cdot St' \cdot \theta_w$$

$$\theta_w = 1 - \frac{Bi'}{Bi''} f_1(x)$$

Where

$$f_1(x) = 1 - \exp(Bi'' \sqrt{Fo})^2 \operatorname{erfc}(Bi'' \sqrt{Fo}) = 1 - \exp(1)^2 \cdot \operatorname{erfc}(1) = 1 - 2.72 \cdot 0.157 = 0.572$$

$$\theta_w = 1 - \frac{Bi'}{Bi''} f_1(x) = 1 - \frac{0.33}{0.71} \cdot 0.57 = 0.73$$

$$\varphi_L = \bar{\varphi} \cdot St' \cdot \theta_w = 0.43 \cdot 2 \cdot 0.73 = 0.63$$

$$t_L = t_0 + \bar{\varphi} \cdot St' \cdot \theta_w \cdot (t_{soil} - t_0) = -16 + 0.63 \cdot (10 + 16) = +0.44^\circ C$$

The amount of heat removal in a time τ is equal:

$$\Delta Q = 2 \cdot Po' \cdot c \cdot \rho \cdot V \cdot (t_{soil} - t_0) \cdot Bi' \cdot Fo$$

$$Fo = \frac{a_{soil} \tau}{R_0^2} = \frac{5.2 \cdot 10^{-7} \cdot 46817}{0.11^2} = 2$$

$$Po' = 1 - \frac{Bi'}{Bi''} f_3(x),$$

where

$$f_3(x) = 1 - \frac{2}{\sqrt{\pi} \cdot Bi'' \cdot \sqrt{Fo}} + \frac{f_1(x)}{(Bi'' \cdot \sqrt{Fo})^2} = 1 - \frac{2}{\sqrt{3.14} \cdot 1} + \frac{0.57}{1^2} = 0.44$$

$$Po' = 1 - \frac{Bi'}{Bi''} f_3(x) = 1 - \frac{0.33}{0.705} \cdot 0.44 = 0.79$$

$$\Delta Q = 2 \cdot Po' \cdot c \cdot \rho \cdot V \cdot (t_{soil} - t_0) \cdot Bi' \cdot Fo = 2 \cdot 0.79 \cdot 1.47 \cdot 1700 \cdot 1.9 \cdot (10 + 16) \cdot 0.33 \cdot 2 = 129092 \text{ kJ}$$

The average capacity of the air ventilation system is

$$P_{aver} = \frac{\Delta Q}{\tau} = \frac{129092}{46817} = 2.75 \text{ kW}$$

The air duct feeding zone:

$$\bar{R}_z = 4\sqrt{Fo} + 1 = 4\sqrt{2} + 1 = 6.6, \quad R_z = R_0 \cdot \bar{R}_z = 0.11 \cdot 6.6 = 0.726 \text{ m}$$

Then Stanton's criterion is equal:

$$St' = \frac{Nu}{Re \cdot Pr} \times \frac{2L}{R_o}, \quad St' = \frac{Nu}{Re \cdot Pr} \times \frac{2L}{R_o} = \frac{78.48}{35427 \cdot 0.712} \times \frac{2 \cdot 12}{0.11} = 0.68$$

The Bio criterion is equal:

$$Bi = \frac{\alpha \cdot R_o}{\lambda_{soil}} = \frac{9.02 \cdot 0.11}{1.3} = 0.76$$

$$Bi' = \bar{\varphi} \cdot Bi; \quad \bar{\varphi} = \frac{1 - \exp(-St')}{St'} = \frac{1 - \exp(-0.6788)}{0.68} = 0.73,$$

$$Bi' = 0.73 \cdot 0.375 = 0.554, \quad Bi'' = Bi' + 0.375 = 0.554 + 0.375 = 0.929$$

3. Discussion of results

The experimental energy saving ventilation system was built in the sheepfold for lambing in Almaty region. The registration of thermo technical parameters of ventilation system (temperature of the outer, inside air, soil and humidity external and internal air) was made using the information-measuring system [3, 4]. To transfer data to the computer modem operator is connected working in master mode after the signals are transmitted to the processing and visualization.

Underground heat exchangers - air conduits are made of corrugated plastic pipe of LLP "EPA Almaty" production. Pipes are made from high density polyethylene, the nominal inner diameter from 110 mm to 630 mm. GOST18599-2001. Pipes are produced with socket and muff joints. Specially designed outer surface of the pipe has a high ring stiffness and makes them more resistant to compressive loads (transport, soil water, frost and soil compaction), and elastic structure pipe protects them from damage when exposed to overload. As the material of high density polyethylene has: a high tensile strength, have higher thermal stability and is not subject to corrosion.

The pipe is produced in the segments of standard length of 6 m and 12 m and is designed for underground lying to a depth of 15 m. For registration of thermo technical parameters of ventilation system, that is temperature of the outer, inside air, soil and humidity external and internal air have been developed information-measuring system. During tests energy saving ventilation system during the winter period found that the room temperature of the sheepfold ranged from +5.4⁰C to +6.0⁰C, on average +5.6⁰C, with the number of measurements $n=72$.

The relative humidity of the room of the sheepfold was in average 79.2%. The maximum and minimum value of relative humidity was respectively 93.4% and 64.1%. At the lowest outdoor temperature -18°C (04.02.2014) supply air temperature reached 6°C . Supply flow rate fluctuate depending on the outdoor temperature within $70\text{-}140\text{ m}^3/\text{h}$. The maximum heat output of installation was 2.2 kW.

During tests energy saving ventilation system in summer found that the room temperature of sheepfold ranged from $+16.6^{\circ}\text{C}$ to $+27.29^{\circ}\text{C}$ on average $+22.3^{\circ}\text{C}$, with the number of measurements $n = 820$. The relative humidity of the room of sheepfold averaged 30.5%. Maximum and minimum value of relative humidity was respectively 58.88% and 10.37%. At the highest temperature of the outside air $+33.4^{\circ}\text{C}$ supply air temperature reached $+19.6^{\circ}\text{C}$ and humidity increased from 12% to 23%. Air flow rate was $140\text{ m}^3/\text{h}$. The cooling capacity of the installation was 2.6 kW.

Conclusion

In times of testing energy saving ventilation system provided the required power saving mode and zootechnical parameters of the microclimate in the maternity ward of the sheepfold. Energy saving ventilation system has been adopted for economic use and recommended for implementation in the sheep farms.

REFERENCES

- 1 Stepanov V.E. *Renewable energy on farms*. Moscow, Agropromizdat, 1989, 112 p. [in Russian]
- 2 Hodchenko N.K. Using the heat of the earth for heating and cooling of livestock buildings. *Mechanization and Electrification v selskom hozyaistve*, 1982, No.11, pp. 16 – 17. [in Russian]
- 3 Issakhanov M.J., Alibek N., Dyusenbayev T. etc. *The ventilation device*. Innovative Patent of Republic Kazakhstan KZ 26930, Bull. 5, Published 15.07.2016.
- 4 Issakhanov M.Zh., Alibek N., Dyusenbayev T. Energy saving ventilation systems for sheep premises. *Journal International scientific, applied and informational journal mechanization in agriculture*, Sofia, Bulgaria. 2014, Vol.7, pp. 20 – 21.
- 5 Issakhanov M.Zh., Alibek N., Dyusenbayev T. Research results of energy efficient ventilation system of sheepfold. *International journal for science, technics and innovations for the industry. Machines Technologies Materials*. 2015, Issue 9, Sofia, Bulgaria, pp. 43 – 45.
- 6 Issakhanov M.Zh., Sakipova Sh.E., Alibek N., Dyusenbayev T. On the simulation of energy-saving ventilating system. *Science and World*, 2017, Vol.1, No. 10 (50), pp. 59 – 61.

UDC 44.35.31

INVESTIGATION OF THE MAIN CHARACTERISTICS OF THE STRAIGHT FLOW HYDRO TURBINE

Kazakbay G.B., Turalina D.E.

Farabi Kazakh National University, Faculty of Mechanics and Mathematics, 050040,
Al-Farabi 71, Almaty, Kazakhstan, ggauharkb@gmail.com

In this paper the results of the research conducted with the aim to determine the effective version of hydro wheel blades of straight flow hydro turbine are presented. The increasing of energy efficiency of hydro turbine is directly related to the configuration of blades. Investigation is performed in the COMSOL Multiphysics application program with numerical method. Navier-Stokes equations describe motion of water flow. Numerical research of flow is performed using Reynolds Averaged Navier-Stokes method. The optimal attack angle of water on hydro turbine blades is determined, optimal location of the blades, changing of velocity and pressure distribution of water through hydro turbine blades are investigated. Lift and drag forces, coefficients acting on the blades are defined. Based on the results of the research, the optimal configurations of the hydro turbine blades with high energy efficiency are determined.

Keywords: hydro turbine, blade, COMSOL Multiphysics, lift force, drag force, lift coefficient, drag coefficient.

Introduction

Scientific research work is related to improving the energy efficiency of hydro turbine by changing the stream flow to hydro wheel. Hydropower plants use energy of water flow as the source of energy. Hydro turbine is the hydro engine that turn coming flow energy to mechanical energy.

Today, the whole world pays great attention to water flow energy as the effective source of energy. Investigated hydro turbine for small hydroelectric power station does not require a dam. Instead, it works in scheme as a part of the water given to head tube, after flowing through hydro turbine again dumped into the river. This straight flow hydro turbine size is small, so to construct it need less material accordingly it cost cheaper.

It is significant to correctly choosing of the structure of the turbine, the size and location of the blades, the parameters of the guide vane, the head of water, the structure of the hydro wheels when installing a hydro turbine on a water stream to generating sufficient energy and effective working. Scientific research working is aimed to improving low head hydro turbine efficiency by changing the stream flow to hydro wheel. The optimal version of the attack angle on guide vane and hydro wheel blades is for improving efficiency of hydro turbine. Investigated low head hydro turbine can be used in the small and medium rivers of the Central Asian countries and Kazakhstan. This low head hydro turbine for small hydroelectric power station is for using for seasonal agriculture to farmers and for using in small settlements and remote villages [1, 2].

1. Computational experiment

The method of research is a numerical experiment. A theoretical study was carried out, a mathematical model of a hydro turbine blade was performed in the COMSOL Multiphysics application package. The COMSOL Multiphysics examines the distribution of velocity and pressure of water along the turbine blades [3]. External construction of 3D model of hydro turbine in the interactive of COMSOL Multiphysics application package is shown in Figure 1.

Water enters through inlet tube, guide vane, rotating hydro wheel and pass through turbine then exit through outlet tube.

To take more energy is needed to rotate the hydro wheel as more. Therefore, there is a guide vane with the aim to regulate impact and direction of water flow to the hydro wheel blades. When water flow through hydro turbine passing through guide vane and hit blades with pressure, then they rotate [4, 5].

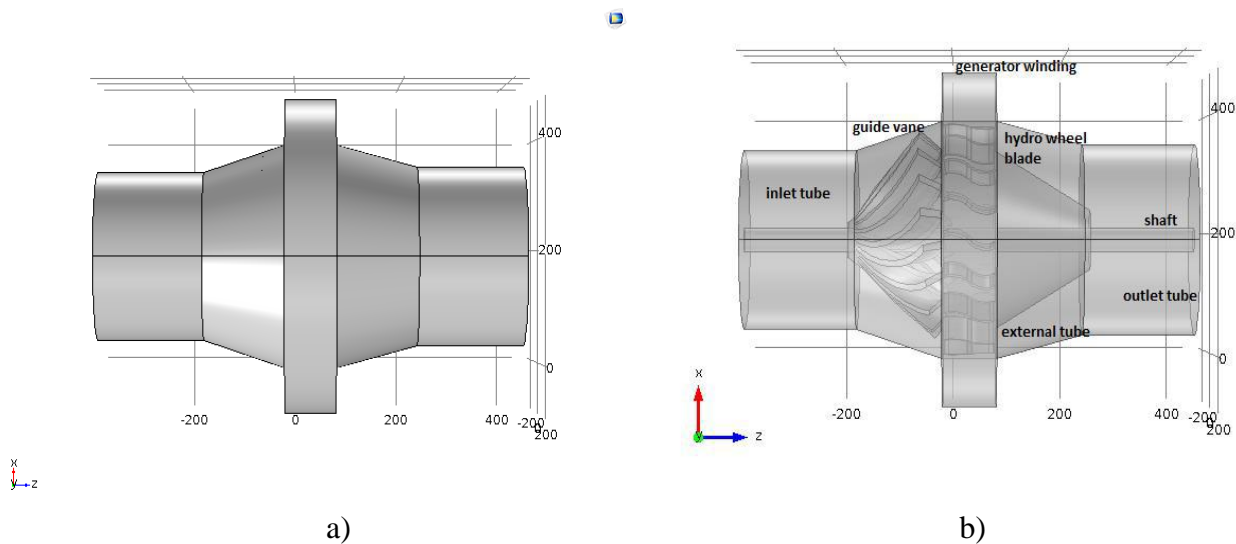


Fig.1. Model of hydro turbine: a) external construction, b) internal construction.

Guide vane and hydro wheel of the hydro turbine are shown in Figure 2. Front part as cone, blade located at part as cylinder.

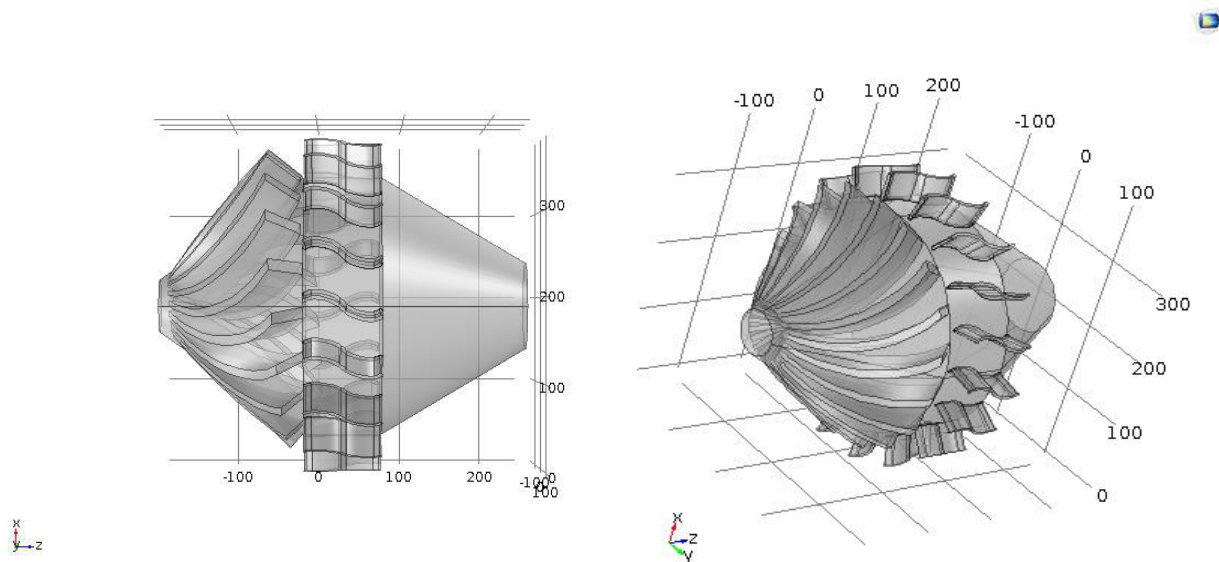


Fig.2. Guide vane and hydro wheel.

The energy efficiency of the hydro turbine is influenced by the number, shape, location, and attack angle of the guide vane and blades [6]. Therefore, the results of the research of the attack angle to the hydro wheel blades are presented. Attack angle is the angle between coming flow direction and chord line of the blade. Research was conducted with the purpose of improving the energy efficiency of hydro turbine.

Numerical calculation was performed by COMSOL Multiphysics application package. The results were obtained by changing the attack angle of water flow on blades of hydro wheel in two dimensional domain. Three different angles were obtained to show the improving in energy efficiency and to compare. The distribution of velocity and pressure of water flow in COMSOL Multiphysics application package during 10 seconds was analyzed, with suggesting that the initial velocity 1 m/sec.

Distribution of water flow velocity and pressure was calculated with using Reynolds Averaged Navier Stokes (RANS) method to Navier-Stokes equation for incompressible fluid. For incompressible fluid the Navier-Stokes equations consists of motion and continuity equations [7]:

$$\rho \frac{\partial u}{\partial t} + \rho(u \cdot \nabla)u = \nabla \cdot [-pI + (\mu + \mu_r)(\nabla u + (\nabla u)^T)] + F$$

$$\rho \nabla \cdot (u) = 0 \tag{1}$$

where u is the fluid flow velocity, ρ is the fluid density, p is the fluid pressure, μ is the fluid dynamic viscosity, ∇ is nabla operator, I is the identity matrix, T is stress tensor, F is the applied body force on the fluid.

2. Computational experiment Defining optimal attack angle of the blades

There are two ways to changing the attack angle of the model. It is possible to turn the blade itself or to fixed the blade but change the flow direction at the inlet. Second way is more simple to adjust the velocity field at the inlet boundary condition and there is no need to remesh the model for every attack angle. Scheme of attack angle on the hydro wheel blade α is illustrated in Figure 3.

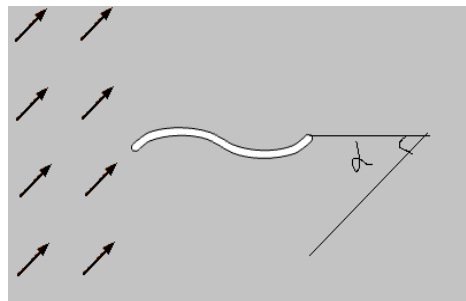


Fig.3. Attack angle.

In Figure 3 arrows show the direction of the flow velocity. There α means attack angle. Attack angle is the angle between coming flow direction and chord line of the blade. The initial velocity of the water flow are determined as $U \cdot \cos(\alpha \cdot \pi / 180)$ in x direction and as $U \cdot \sin(\alpha \cdot \pi / 180)$ in y direction. Here $U = 1$ m/s. Considered three various location of blades with changing the attack angle [8]. Values of attack angle α are $40^\circ, 45^\circ, 60^\circ$.

Results of velocity changing and pressure distribution along blade changing the attack angle during 10 second are demonstrated in Figure 4.

Changing of colour from blue to red shows the increasing of velocity and pressure. Arrows show water flow direction. In the first case the maximum value of velocity is reached to 1.32 m/s and pressure 565 Pa. Pressure increase in the bottom side of the blade as a result of the appearing the lift force. Changing attack angle to 45° the maximum value of velocity is reached to 1.31 m/s and maximum value of pressure is reached to 587 Pa. So we see that the attack angle has affect.

Changing attack angle to 60° angle degree the maximum value of velocity is reached to 1.26 m/s and pressure is reached to 595 Pa. Changing the attack angle is affected to previous results.

Results of numerical experiment by COMSOL Multiphysics of the changing of velocity and pressure distribution of flow with changing attack angle of the blades are shown in Table 1.

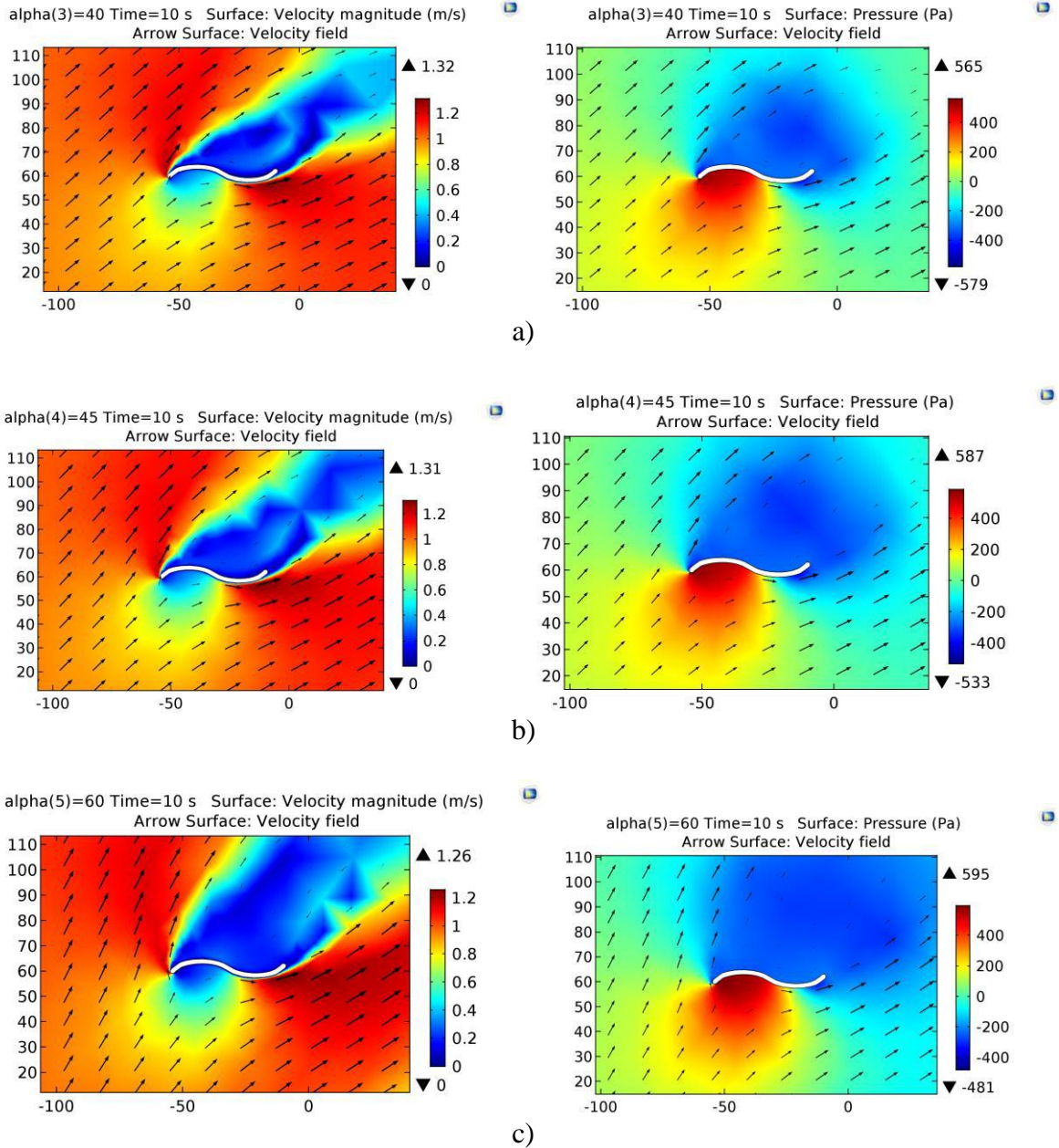


Fig.4. Distribution of velocity and pressure at different attack angle: a) 40°, b) 45°, c) 60°.

Table 1. Velocity and pressure changing with changing attack angle

| Name | Attack angle of flow, degree | Maximum value of velocity of flow, m/s | Maximum value of pressure of flow, Pa |
|------|------------------------------|--|---------------------------------------|
| 1 | 40 | 1.32 | 565 |
| 2 | 45 | 1.31 | 587 |
| 3 | 60 | 1.26 | 595 |

In version when attack angle 40° the maximum value of velocity is reached. Maximum value of pressure is reached when attack angle 60°.

3. Defining lift and drag forces

When fluid flow passes a body, it exerts a force on the surface. The force component that perpendicular to the flow direction is called lift force F_L . The force component that parallel to the flow direction is called drag force F_D [9]. There are two distinct contributors to lift and drag forces — pressure force and viscous force. The pressure force is the force appearing due to the pressure difference across the surface. The viscous force is the force deriving from friction that acts in the opposite direction of the flow.

The lift and drag forces at different angle attack of the blade at tenth second is shown in Fig. 5. Was chosen as various angle attack as 0°, 15°, 40°, 45°, 60°, 90°.

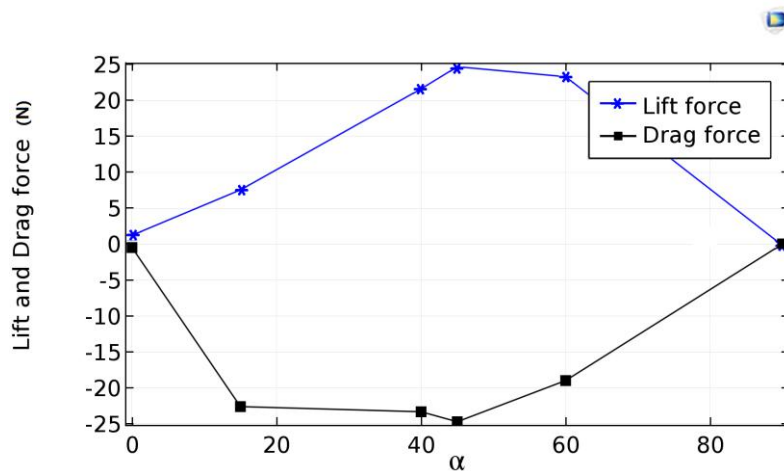


Fig.5. Lift force and drag force at tenth second.

The values of the drag force are decreasing from 0 angle degrees to 45 angle degrees, then values are increasing. The lift force values are increasing from 0 to 45 angle degrees, then started to decreasing. So at 45 angle degree the lift force takes maximum value and the drag force takes minimum value.

4. Defining lift and drag coefficients

Lift coefficient is defined as:

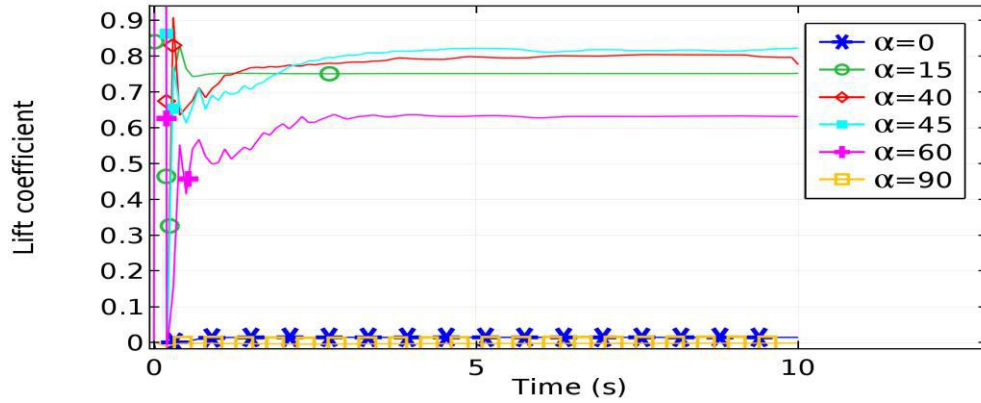
$$C_L = \frac{F_L}{\frac{1}{2} \rho U^2 c} \tag{2}$$

Drag coefficient is defined as:

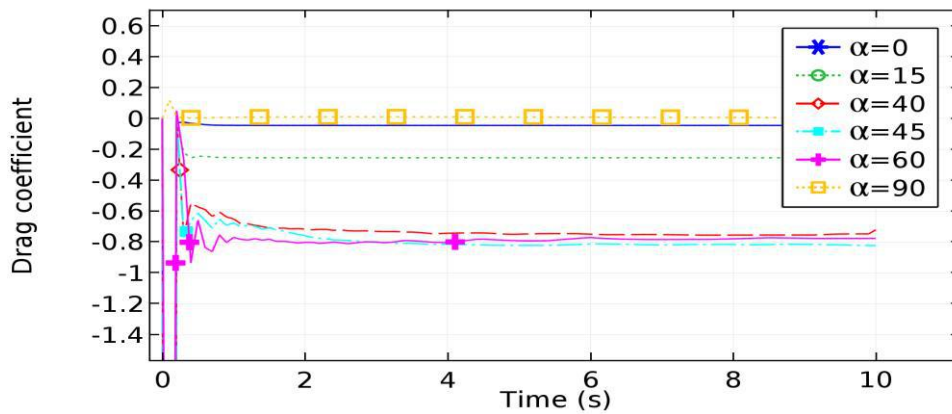
$$C_D = \frac{F_D}{\frac{1}{2} \rho U^2 c} \tag{3}$$

Here C_L is the dimensionless lift coefficient, C_D is the dimensionless drag coefficient, U is the mean velocity, c is the blade length.

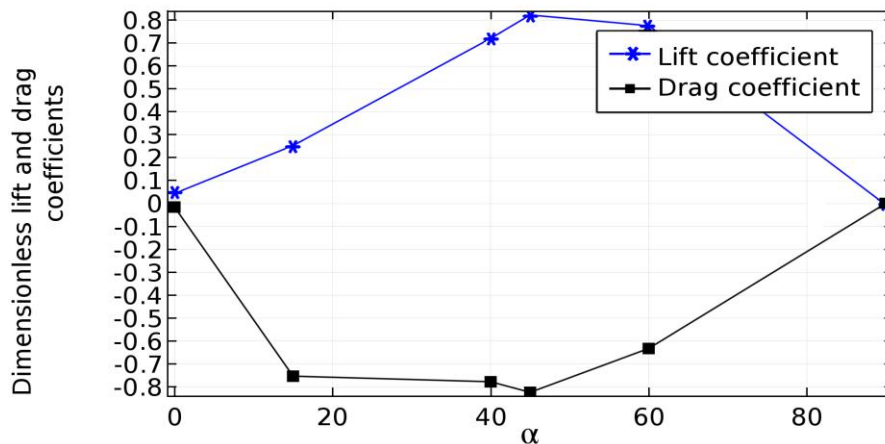
In Figure 6 showed calculation results of lift and drag coefficients at different angle attack. Drag coefficient magnitudes are decreasing from 0 angle degrees to 45 angle degrees, then started to increasing. Lift coefficient magnitudes are increasing from 0 to 45 angle degrees, then it is decreasing. So at 45 angle degree the lift coefficient takes maximum value and the drag coefficient takes minimum value.



a)



b)



c)

Fig. 6. Lift and drag coefficients: a) Lift coefficient during ten seconds, b) drag coefficient during ten seconds, c) lift and drag coefficients at tenth second.

Conclusion

The effective version of hydro wheel blades of straight flow hydro turbine was determined. Research with the aim of improving efficiency of low head hydro turbine was performed. Three various locations of the blades with changing attack angle were investigated in the COMSOL Multiphysics application package. Based on the results of the research, it was determined the optimal configurations of the hydro wheel blades of the hydro turbine. As optimal configuration was chosen hydro wheel blade with the attack angle 45 angle degrees, where maximum value of velocity reached to 1.31 m/s and maximum value of pressure reached to 587 Pa. The lift and drag forces, lift and drag coefficients at different attack angle were defined. Maximum value of lift force and coefficient, minimum value of drag force and coefficient were defined and was taken 45 angle degree as optimal at attack angle.

REFERENCES

- 1 Koshumbayev M., Yerzhan A. The innovative design of free-flow hydraulic turbine small hpp. *Proceeding of the 2nd International conference on Innovative trends in multidisiplinary academic research*, Istanbul, Turkey, 2015, pp.55.
- 2 Turalina D. E., Bossinov D. Zh. Theoretical and experimental investigations to define optimal parameters of straight-flow turbine for non-dam hydro power station. *KazNU Bulletin. Series Mathematics, Mechanics, Informatics*, 2015, Vol. 84, pp. 124 – 131.
- 3 COMSOL Multiphysics *User's Guide*. 2012, 1292 p.
- 4 Bystritskiy G.F., Gasangadzhiev G.G., Kozhichenkov V.S. *Obshchaya energetika. Proizvodstvo teplovoiy i elektricheskoy energii*: Uchebnik. 2017, Moscow, Knorus, 410 p. [in Russian]
- 5 Stesina S.P. *Gidravlika, gidromashini i gidropnevmoprivod*: Ucheb. posobie dlya vyzov. 2007, Moscow, Akademiya, 336 p. [in Russian]
- 6 Bashta T.M., Rydnev S.S., Nekrasov B.B. *Gidravlika, gidromashini i gidroprivodi*: Ycheb. dlya vyzov. 2010, Moscow, Alyans, 423 p. [in Russian]
- 7 Loytsyanskii L.G. *Mechanics of liquids and gases*. 1987, Moscow, Science, 840 p. [in Russian]
- 8 Kazakbay G.B., Turalina D.E. Research of the influence of lift force in accordance with the attack angle of water flow on the hydro wheel blades. *Proceeding of the V International Farabi readings. International scientific conference of students and young scientist*, Almaty, Kazakhstan, 2018, pp.60.
- 9 [Peter Lyu](http://www.comsol.com/blogs/how-do-i-compute-lift-and-drag). How Do I Compute Lift and Drag. Available at: <http://www.comsol.com/blogs/how-do-i-compute-lift-and-drag>

UDC 669.152.005

UNBURNED WASTE COAL FLOTATION AGGLOMERATION

Ibraev E.K., Ibraeva O.T., Sakipov K.E.

Eurasian National University named after L.N. Gumilyov, Astana, sakamer2100@gmail.com

The article presents the results of a study of high-agglomeration unburned waste coal flotation with the development coal-mineral briquette. The technology is that the process of removing moisture is carried out without external supply of heat or coolant and heat generated due to stirring with a dehydrating component (lime dust - waste from the production of burnt lime CaO not less than 70%) due to the exothermic reaction, and heating binder, which is used as the prepared coal resin by heat generated by the implementation of the chemical dehydration. Combining chemical processes of dehydration hydration of lime materials, curing mixture molding processes allow to obtain chemically bonded agglomerated material strength, satisfying the requirements of metallurgical production. The optimum temperature and time parameters of the process and the equity ratio of lime dust, coal tar and dissected initial moisture content of waste coal flotation in achieving their high strength.

Keywords: waste flotation coal, coal-mineral briquette, dehydration, chemical dehydration, coal tar, a binder.

INTRODUCTION

Waste coal flotation is highly dispersed, soaking, swelling ability, etc. In general, flotation waste is represented by particles with a particle size $<74 \mu\text{m}$. Complex mineralogical and petrographic analyzes show that the main mineralizing component of flotation waste is a clay substance (up to 92%), in smaller quantities quartz and carbonates are contained. The content of combustible mass (carbon) in waste is 35-50%. The sulfur content is much lower than in the breed of large classes. The predominant amount of clay substance in flotation tailings, compared to other carbonaceous wastes, makes them a plastic material.

These properties of the waste make it difficult to separate the phases during the flotation process and then dehydrate the resulting products to a transportable state that allows them to be removed from the enterprise by belt conveyors, by road or rail. Therefore, dewatering of flotation residues at coal preparation plants, near which there are opportunities to seize unused or low-value agricultural lands, is carried out in tailing dumps. A small concentration of solids in the pulp and poor sedimentation require a long service life of these facilities to a full concentration of waste and the possibility of cleaning them for reuse.

All the complexity in the disposal of liquid wastes of metallurgical production, which include flotation waste, in wet coal enrichment processes lies in the fineness and their high humidity, which requires the use of expensive and complex systems of preliminary dehydration and preparation technologies. At present, a number of technological processes for the processing of dusts and sludges into the conditioning materials of ferrous metallurgy, often with simultaneous separation of non-ferrous metals, have been proposed, tested and introduced into industrial practice [1-7]. With the disposal of these technogenic products, non-firing agglomeration methods are increasingly used, the application of which increases the efficiency of waste processing. A number of such methods have been introduced into industrial practice [1-5].

At the same time, with regard to non-burning agglomeration, its cardinal advantages in comparison with high-temperature methods (agglomeration and roasting of pellets) in the main technical and economic (prime cost, capital and current costs, energy consumption, technological fuel numbers, etc.) and environmental indicators (3-5 fold decrease in the degree of environmental pollution) are shown repeatedly, for example in [4-7], and are not disputed by anyone. With a moisture content of 25-30%, the water separation in flotation waste is almost stopped, the waste acquires flowability. The studies were based on the conditions for obtaining in flotation waste or

their mixtures the moisture required for normal briquetting and utilization in metallurgical production.

1. Theory of dewatering of flotation waste coal

The hardening of the sludge-limestone mixture is a consequence of the physico-chemical processes taking place in the salt-water system, of which the components CaO, SiO₂, Al₂O₃, Fe₂O₃, H₂O, etc. are compounds contained in man-made production waste. According to the colloid-chemical theory of hardening of hydraulic binders AA. Baikova chemical transformations occurring when mixing lime with a slurry of high humidity can be expressed by the following reaction:



However, calcium hydrosilicate in water is very slightly soluble and remains in the colloidal state for a long time, gradually recrystallized, and then compacted and hardened. Phenomena as a result of which the cement dough acquires coherence and strength and turns into a solid monolithic body, is, according to A.A. Baikov, a purely physico-mechanical character. Chemical processes are completed within a few hours (not more than a day) after the interaction of the binder, in our case of pulverized lime, with the water of the slurry with the formation of a fragile loose mass. Turning it into a stone-like body occurs mainly during the next few hours or days due to the formation of a crystalline splice of hydroxide and calcium hydro-silicates. The crystallization period is the longest and is characterized by a negligible release of heat.

When the binder interacts, in our case of pulverized lime, with slurry water, there is a so-called preparatory period in which a saturated solution forms. The heating of the mixture at this point is insignificant, since the dissolution process is endothermic. Only when saturation is achieved, the cement dough is quickly heated by the hydration reaction. Depending on the conditions (mineralogical and disperse composition, initial slurry moisture and mixing speed), the intensity and speed of hydration varies.

The process of chemical dewatering of flotation waste flows in the kinetic region and is characterized by exothermic reaction of the dehydrating component with water with formation of calcium hydroxide by reaction (1) and is accompanied by an increase in temperature and the rate of dehydration.

2. The experimental part

The heat released in the process of phase interaction goes to the evaporation of moisture. There is a removal of the bulk of moisture, accompanied by a rapid dehydration rate and ending when the maximum temperature of the mixture is reached. Similar results were established in the works conducted by the NGO "Tulachepet" [6,7]. Experiments on dewatering were carried out in sequence with a change in the main parameter of the process-the initial moisture content of the flotation waste.

The maximum temperature was observed during the first 5 minutes after the mixing and reached 100-108 ° C in mixtures with a volume ratio of 1: 1.5, 1: 2 (66.88%). The dynamics of temperature change in mixtures shows that the main part of moisture evaporates during the first 5-10 minutes and cooling to room temperature was fixed in the middle 1.5 - 2 hours after the mixing. This is due to the flow of the process in the diffusion region, the essence of which is as follows. The process of binding residual moisture is controlled by diffusion transfer of water molecules through a thin diffusion pore layer that forms on the surface of the dehydrating material particles at this time point. The fine surface, permeate layer consists of crystallized hydroxide and calcium carbonate

formed as a result of the flow of the reaction of calcium hydroxide absorption of carbon dioxide from the surrounding atmosphere by reaction:



From the results of experiments it follows that the highest rates of dehydration were observed when preparing mixtures with a volume ratio of 1: 1.5, 1: 2, which is explained by the rapid flow of exothermic reaction between active CaO and water of the coal-dressing slurry. The intensity of the process of chemical dehydration depends on the type of dehydrating materials used, the activity of CaO, MgO, their fractional composition, and the degree of mixing of the main components determined by the maximum region of contact between the reacting phases.

The chemical compositions of some mixtures, which are presented in Table 1, have been selected selectively. The chemical composition data determine the possibility of using float-lime mixtures in the metallurgical range, in particular in agglomeration and steelmaking industries.

Table 1. Chemical Composition of Flotation and Limestone Mixtures

| Ratio of flotation and lime waste | The initial moisture content of the flotation waste | C _{обм} | CaO | SiO ₂ | FeO | MgO | Al ₂ O ₃ | P ₂ O ₅ | Lossonignition |
|-----------------------------------|---|------------------|-------|------------------|------|------|--------------------------------|-------------------------------|----------------|
| 1:0.5 | 20 | 32.85 | 22.59 | 16.99 | 1.50 | 0.56 | 6.96 | 0.085 | 49.62 |
| 1:1.0 | 20 | 25.67 | 32.12 | 12.84 | 1.06 | 0.58 | 5.29 | 0.080 | 46.03 |
| 1:1.5 | 20 | 22.50 | 42.70 | 11.19 | 1.03 | 0.50 | 4.48 | 0.073 | 43.06 |
| 1:2.0 | 20 | 17.30 | 44.15 | 7.83 | 0.81 | 0.52 | 3.08 | 0.066 | 39.95 |
| 1:0.5 | 25 | 30.35 | 23.05 | 18.66 | 1.63 | 0.74 | 6.70 | 0.096 | 46.86 |
| 1:1.0 | 25 | 25.90 | 33.22 | 14.38 | 1.16 | 0.62 | 5.60 | 0.082 | 44.55 |
| 1:1.5 | 25 | 22.67 | 41.14 | 12.74 | 1.28 | 0.66 | 4.98 | 0.082 | 41.86 |
| 1:2.0 | 25 | 21.39 | 37.22 | 12.13 | 0.63 | 0.89 | 4.54 | 0.080 | 40.78 |
| 1:0.5 | 30 | 32.94 | 19.20 | 17.62 | 1.60 | 0.72 | 7.21 | 0.105 | 49.44 |
| 1:1.0 | 30 | 23.99 | 39.03 | 12.98 | 1.19 | 0.51 | 4.70 | 0.076 | 43.55 |
| 1:1.5 | 30 | 22.84 | 34.68 | 11.96 | 1.11 | 0.61 | 4.89 | 0.105 | 42.83 |
| 1:2.0 | 30 | 21.25 | 46.37 | 10.52 | 1.02 | 0.43 | 4.14 | 0.071 | 42.17 |

The optimal ratio for mixing the original components were 1: 1.5; 1: 2, in which self-depositing pulverized mixtures of the "fine sand" type were obtained. According to the results of work at the Dnipro Metallurgical Combine, a mixture with such a ratio of carbon-bearing and lime-containing materials can be successfully applied in convection melting [8]. In a 1: 1 ratio, mixtures with more coarse particles, such as "fine sand", were obtained. In mixtures with a ratio of 1: 0.5, a large "lump" formed about 10 mm in size (especially in mixtures with an increased initial moisture content of the flotation waste), which were easily broken by mechanical action. All mixtures did not have a tendency to dust. This is due to the presence of clay components: Al₂O₃, SiO₂, which form CaO and MgO silicates, aluminates and calcium and magnesium in calcareous dust, in addition to active oxides of CaO and MgO. These compounds, when in contact with water, are rapidly solidified in the air.

The heat released during the reaction of calcium and magnesium oxides with water is consumed by the evaporation of water, which accelerates the drying of the mass. The established

characteristics of the process of chemical dewatering of waste flotation by pulverized lime served as a basis for the technology of their preparation for disposal at JSC "ArcelorMittal Temirtau", in particular, for the production of coal mineral beets from them.

3. Energy-saving way of processing of coal slimes

Analysis of the known methods of agglomeration of coal enrichment wastes [9, 10] showed that the production of a solid agglomerated material (briquettes) from high-moisture coal slimes is achieved when the sludge is pre-dried to a residual moisture of about 10%, binding binders mainly in the form of coal tar and their derivatives and preheating the batch to the melting temperature of the binder component. Therefore, we set the task of developing a method that has low energy consumption and a simplified technology for processing coal slurries of high humidity during the disposal of pulverized lime production waste.

As the results of the research have shown, the best results are achieved by using chemical dewatering (drying) of high-moisture coal flotation waste using pulverized calcined lime (pulverized lime) waste and as a binder of a small amount of coal tar (3-5%).

The essence of the proposed method consists in combining the processes of chemical dewatering of coal slurry with shaping, and as a chemical dewatering agent, dust-like lime, which is trapped from the waste gases during calcination of limestone in lime kilns by dry dust-gauging apparatus, is used as a binder pre-dispersed to 0-1 mm prepared coal tar at a rate of 3-6% and kept for 15 minutes at a temperature of 100 - 110 ° C and then pressed with a or 250-350 kg / cm². In the proposed method, the drying of coal slurry (flotation waste coal) of high humidity is carried out at the expense of the heat released during hydration of pulverized lime, and the heat released during chemical dehydration is also used to heat the coal tar at a temperature of 100-110 0C. To obtain strong, well-formed briquettes, a mixture of 3 components is mixed in the mixer for 5-6 minutes and held for 15-20 minutes and then without cooling the mass is pressed (molded) on a roller press at a pressure of 250-350 kg / cm².

The essence of the method is based on the established new regularities of the process of moisture removal by chemical bonding it with the dewatering component (hydration) and hardening of the mixture that were established by our studies [6, 11,12]. In addition, lime performs the functions of the binder as it relates to air binding materials and facilitates the cementation of the crystallized particles of flotation waste into the conglomerate and the conditions for obtaining strong coal-mineral briquettes are improved.

To ensure better compressibility, the mass is held at these temperatures for 15-20 minutes. With these parameters, the resin passes into a plastic state, in which its astringent properties are improved. In addition, as the temperature increases, the plasticity of the coal enrichment waste increases, which increases the strength of the briquettes. On the other hand, as the temperature is raised, the viscosity of water decreases and it is easier to leave it from the capillaries to the surface of the particles. The increase in the strength of briquettes from heated materials is also explained by the fact that during pressing, stronger covalent bonds arise between the functional groups of the macromolecules of coal. At the same time, the optimal ratio between the mass fraction of calcareous dust and coal tar (mass, %) from the moisture content of flotation was established (Tabl.2).

The novelty of the proposed technical solution lies in combining the hardening processes of the slurry-limestone mixture with the shaping processes, which is achieved in accordance with the proposed method for mass pressing in molds. To obtain strong briquettes that are stable to atmospheric precipitation and transportation, a binder in the form of a prepared coal-tar mixture in an amount of 3-6% is introduced into the lime-mud mix with stirring, which is heated by the internal heat released during chemical dehydration by reaction (1) with pulverized lime with the content of CaO (more than 70%), i.e. without supply of heat from outside.

Table 2. Ratio between the components mass fraction from the moisture content of flotation

| Humidity of flotation waste, % | Mass fraction of resin, % | Mass fraction of calcareous dust, % |
|--------------------------------|---------------------------|-------------------------------------|
| 20 | 4.5-6 | 15-25 |
| 15 | 3-6 | 10-20 |
| 10 | 3-6 | 10-15 |

4. Discussion of results

The results of pilot studies at these optimal temperature and time parameters of the process and the proportional ratios of pulverized lime, prepared coal tar and the initial moisture content of flotation waste of coal have shown that high strength of coal-mineral briquettes is achieved in the absence of weight loss of the mass during pressing. Moreover, the content of calcium oxide in the dewatering component (pulverized lime) should be at least 70%.

When the duration of the temperature holding of the mixture is less than 15 and more than 20 minutes, with the remaining parameters within the optimal limits, a low strength of the briquettes, which tend to spill, is obtained. With a mass fraction of coal tar in a mixture of less than 3%, the required strength of the briquettes is also not ensured. With a mass lime dust content of less than 10%, and with a calcium oxide content in pulverized lime of less than 70%, the complete chemical dewatering and hardening of the mixture is not ensured, which also leads to insufficient strength of the coal-mineral briquettes produced and mass losses of the mixture during compression are observed. The mass fraction of calcareous dust in a mixture of more than 25% is undesirable, since this leads to a reduction in the heating value of the briquette.

Studies have shown that the strength of beets is affected by the granulometric composition of the initial components. In the presence of increased content of large particles in them, the number and dimensions of the voids in the mass to be massed increase, and the part of the processing energy is stopped for the dissolution of a certain fraction of large grains and the filling of voids. Therefore, the strength of the purchased beets will be lowered. On the basis of the experiments performed, it is possible to distinguish the most optimal ratios of components in the mixture to be processed at a temperature of 110 ° C and a discharge time of 15 minutes.

The innovative method of the patent of the Republic of Kazakhstan No. 21583 for the invention "Method for processing coal slime" was obtained on the developed method [13]. Based on the study of the smolomagnesite shop of JSC "ArcelorMittal Temirtau", which has press equipment, an industrial technological scheme for production of coal-minerals briquettes for steelmaking production was developed (Fig. 1). Coal minerals can be used as deoxidizing, refining and fuel materials.

Conclusion

The proposed method is characterized by a new set of characteristics:

- the process of moisture removal is carried out without external supply of heat or coolant;
- The heat necessary to remove excess moisture from the coal slurry is released when it is mixed with the dewatering component as a result of the exothermic reaction;
- as a dewatering component, waste from the production of calcined lime in the form of pulverized lime, trapped from dusty process gases when calcining limestone in lime kilns in dust-gas-cleaning devices with a high content of calcium oxide (CaO at least 70%) is used;

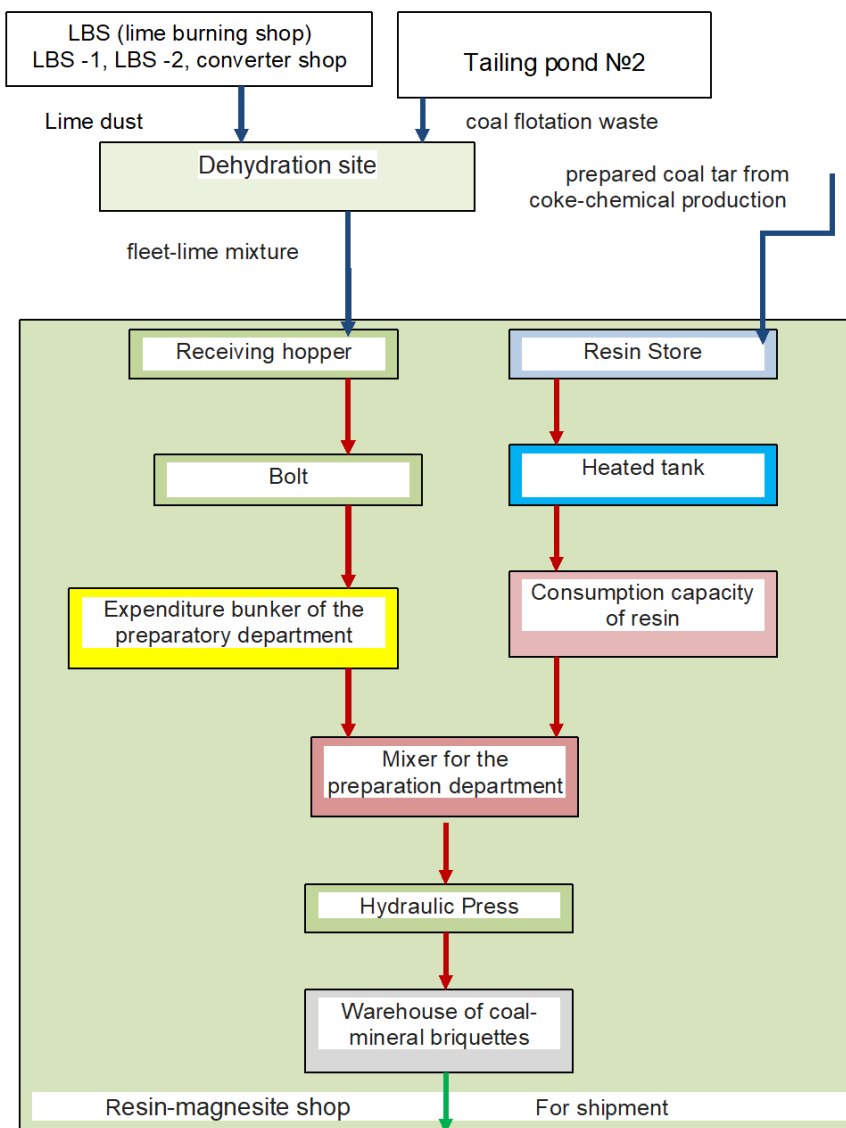


Fig.1.Technological scheme of processing of coal slimes .

- the heating of the binder, in which quality the prepared resin is used, is produced with mixing due to the heat of chemical dehydration released during the process and its flow in the kinetic region; Fifth, the prepared coal tar is pre-dispersed to 0-1 mm.

The following optimal process parameters were established: the preheating temperature before pressing 100-110 °C, the holding time 15-20 min, as well as the ratio of the consumption of pulverized lime, prepared coal tar, depending on the initial moisture content of coal flotation waste.

REFERENCES

1. Ibraev I.K., Targinova G.B., Kulishkin S.N., Ibraeva O.T. Technology of utilization of oil-iron-containing waste of rolling production. *Proceeding of the Intern. Scientific and practical conference "Energy-saving technologies of Irtysh"*. Pavlodar, 2001, pp. 289 - 293. [in Russian]
2. Ibraeva O.T., Torgovets A.K., Ibraev I.K. Technology of utilization of oil-and-iron waste of metallurgical production. *Proceeding of the Intern. Scientific and practical conference "The quality of education: Management, credit system of education, achievements, problems"*. Ekibastuz, 2006, pp. 272 - 275. [in Russian]

3. Ibraeva O.T., Ibraev I.K. *Modern technologies of preparation for utilization of slurries of metallurgical production*. Pavlodar, 2006, 27 p. [in Russian]
4. Ibraeva O.T., Ibraev I.K., Chernetsov V.I., Lekhtmetts V.I. *Problems of resources and ways of their solution in the metallurgical and mining industries. Scientific and technical progress in metallurgy*. Almaty, 2007, pp.11 - 19. [in Russian]
5. Ibraev I.K., IchevaYu.B., Maksimov E.V., Makhmetov E.Kh., Molchanova E.S. Dehydration of metallurgical slimes. *Proceeding of the Intern. conference "Improving the quality of education and scientific research" in the framework of the VII Satpaev Readings*. Ekibastuz, 2008, pp. 302- 305.
6. Borysov V.M., Kuzmin A.A., Boyko M.G. Kinetics of sludge dewatering with lime. *Izv. HIGH SCHOOLS: Ferrous metallurgy*, 1984, No. 3, pp. 128 - 129.
7. Ibraev I.K., Kulishkin S.N., Ibraeva O.T. Dehydration of converter sludge with waste from lime production. *Proceedings of the 3rd Congress of Steel Makers*. Moscow, 1996, pp. 121-124.
8. Aizatulov R.S., Protopopov E.V., Verevkin G.I., Volynkina E.P. Use of carbon-containing bracelets for convection melting. *Proceeding of the 2nd congress of steel smelters*. Moscow, 1994, pp. 86 - 88.
9. Marian Rutkowski, Jadwiga Węczkowska. *Method for obtaining shaped products from coal slurries*. A.S.558934 NDP. M. cl. 2 C 10 L 5/14. No. 1621306/26., 987 p.
10. Elishevich and others. *Method of processing coal waste*. A. with. 1171510. USSR cl. C 10 L 5/48. 1123 p.
11. Ibraev I.K., Golovkin V.K., Kulishkin S.N., Sadovsky V.G., Ibraeva O.T. Research of processes of dehydration and preparation of iron-containing sludges for utilization. *Steel*, 1996, No.1, pp. 71-74.
12. Ibraev I.K., Kulishkin S.N. Use of dolomite dust to prepare oily scale for disposal. *Ferrous metallurgy*. 1997, Issue 5-6, pp. 56 - 58. [in Russian]
13. Ibraeva O.T., Ibraev I.K., Chernetsov V.I., Lekhtmetts V.I. *Method of processing of coal sludge*. Innovative patent of the Republic of Kazakhstan № 21583 for invention. Bulletin Industrial Property, No. 8, publ. 08/14/2009, 1324 p. [in Russian]

SUMMARIES

ТҮСІНІКТЕМЕЛЕР

АННОТАЦИИ

Жумаев М.Р., Шарипов М.З., Миржонова Н.Н.

Бозе-Эйнштейндік конденсация солитондарының орташаланған Лагранжианы.

Жұмыста Бозе-Эйнштейндік конденсация солитондарына конденсатты түзетін атомдардың флуктуациялық өзараәрекеттесудің әсері қарастырылған. Гросса-Питаевский деңгейінің қысқаша қорытындысы келтірілген. Бозе-Эйнштейндік конденсация солитондарының орташаланған Лагранжианы анықталған. Алынған нәтижелер солитондарға әр түрлі козулар әсерлерін динамикасын зерттеуге мүмкіндік береді.

Жумаев М.Р., Шарипов М.З., Миржонова Н.Н.

Усредненный Лагранжиан солитонов Бозе-Эйнштейновской конденсации.

В работе рассмотрено влияние флуктуационного взаимодействия атомов, образующих конденсат, на солитоны Бозе-Эйнштейновской конденсации. Приведён краткий вывод уровня Гросса-Питаевского. Определён усреднённый Лагранжиан солитонов Бозе-Эйнштейновской конденсации. Полученные результаты дают возможность исследовать динамику солитонов под действием различных возмущений.

Гученко С.А., Завацкая О.Н., Юров В.М., Касымов С.С., Лауринас В.Ч.

Көп элементті жабындылардың фракталдық құрылымы.

Мақалада иондық-плазмалық жабындылардың фракталдық құрылымы және физикалық қасиеттері қарастырылған. Қысқаша және толық емес шолудан анықталғаны, фракталдар материалтануда, трибологияда, гидрологияда, биологияда және т.б. салаларда қолданылады. Зерттеулер үшін индукциялық балқыту әдісімен алынған көп элементті Cr-Mn-Si-Cu-Fe-Al, Zn-Al, Mn-Fe-Cu-Al катодтар және Ti катодтары қолданылды. Жабындар ННВ-6.6И1 вакуумдық қондырғыда иондық-плазмалық әдіспен болат үлгілерге түсірілді. Электронды-микроскопиялық зерттеу Tescan фирмасының MIRA 3 растрлық электрондық микроскопта жүргізілді. Оптикалық микроқұрылымы Ериксант металлографиялық микроскопта, ал наномасштабты деңгейде NT-206 атомдық-күштік микроскопта зерттелді. Жабындылардың микроқаттылықты зерттеу HVS-1000A құралмен жүргізілді Жабындылардың фракталдық өлшемділігі есептелді. Фракталдық өлшемділіктің азаюымен беттік керілу, микроқаттылық пен үйкеліс коэффициенті кемиді. Бұл ұсынылған формулалармен жақсы үйлеседі. Алынған эксперименттік мәліметтер барлық қарастырылған модельдермен үйлеседі, бұл келесі модельдер: титан нитридінің қоспалар шоғырларының радиалды градиентінің болуымен байланысты концентрациялық аса салқындау; түзілуі температураның вертикаль градиентінің болуымен шартталған Бенар ұяшықтары; жабындыдағы пластикалық деформацияның болуымен байланысты ұялы дислокациялық құрылым.

Гученко С.А., Завацкая О.Н., Юров В.М., Касымов С.С., Лауринас В.Ч.

Фрактальная структура многоэлементных покрытий.

В настоящей работе рассмотрена фрактальная структура и физические свойства ионно-плазменных покрытий. Как следует из краткого и неполного обзора, фракталы используются в материаловедении, трибологии, гидрологии, биологии и т.д. Для исследования использовались многоэлементные катоды Cr-Mn-Si-Cu-Fe-Al, Zn-Al, Mn-Fe-Cu-Al, полученные методом индукционного плавления, и катоды Ti. Покрытия наносились на стальные образцы ионно-плазменным методом на вакуумной установке ННВ-6.6И1. Электронно-микроскопическое исследование проведено на растровом электронном микроскопе MIRA 3 фирмы TESCAN. Оптическая микроструктура исследовалась на металлографическом микроскопе Эпиквант, а в наномасштабе - на атомно-силовом микроскопе NT-206. Исследование микротвердости покрытий проводилось на микротвердомере HVS-1000A. Рассчитана фрактальная размерность покрытий. С уменьшением фрактальной размерности уменьшаются поверхностное натяжение, микротвердость и коэффициент трения. Это согласуется с предложенными формулами. Полученные экспериментальные данные в принципе укладываются во все рассмотренные нами модели: концентрационного переохлаждения, связанного с наличием радиального градиента концентрации примеси нитрида титана; ячеек Бенара, возникновение которых обусловлено наличием вертикального градиента температуры; ячеистой дислокационной структуры, связанной с наличием пластических деформаций в покрытии.

Бақтыбеков Қ.С.

Қатты денелердегі бейсызықты радиациялық процестер.

Қатты денеге радиациялық әсерлерінің механизмдерін зерттегенде кезде бұл процестердің түсінуін және мөлшерлік сипатталуын қиындататын ерекшеліктер бар. Біріншіден, «зат + радиациялық әсер» ашық жүйе.

Ашық жүйеде термодинамикалық параметрлерінің тепе-теңдік мәндерінен ауытқуы энергия және зат тасымалдау процестеріне әкелуі мүмкін. Екіншіден, материалдардың радиациялық әсермен өзараәрекеттесуі нәтижесіндегі процестер бейсызықты болып табылады. Қоршаған ортамен зат мен энергияның үздіксіз алмасуы жүйеде термодинамикалық тепе-теңдік күйінен алыс болатын орнықты динамикалық күйлерге әкеледі. Бұл диссипативтік құрылым деп аталатын анықталған кеңістік немесе уақыттық реттіліктің құрылуына әкеледі.

Бактыбеков К.С.

Нелинейные радиационные процессы в твердых телах.

В исследовании механизмов радиационного воздействия на твердые тела существуют особенности, которые усложняют понимание и количественное описание таких процессов. Во-первых, система «вещество + радиационное воздействие» является открытой. В открытой системе отклонения термодинамических параметров от их равновесных значений приводят к процессам переноса энергии и вещества. Во-вторых, процессы, происходящие в результате взаимодействия материалов с радиационным воздействием, являются нелинейными. Непрерывный обмен веществом и энергией с окружающей средой приводит к тому, что в системе реализуются устойчивые динамические равновесные состояния, далекие от состояния термодинамического равновесия. Это приводит к появлению определенной пространственной или временной упорядоченности дефектов называемые диссипативной структурой.

Ашуров Ә.Е.

Ғарыштық аппаратты квазигеостационарлық орбитадан шығару.

Белсенді жұмыс мерзімін атқарып болған немесе оқыс жағдай нәтижесінде сәтсіздікке ұшыраған ғарыштық аппаратты квазигеостационарлық орбитадан шығаруды модельдеу нәтижелері келтірілген. Орбитаны 300 км биіктікке көтеру үшін қажет болатын импульс, маневр жасауға қажет жанармай мөлшері, соған тиісті қажет уақыт, мұнда үлкен жарты ось пен эксцентриситеттің өзгеруі және аппараттың бойлық бойынша дрейфі есептелген. Орбитаны көтеру үдерісі газ қозғалтқыштарды (ГК) тізбектеп қосу нәтижесі және соған сәйкес орбита параметрлерінің өзгерісі ретінде қарастырылған. Ғарыштық аппараттың дрейфі және бойлығының түрлі эксцентриситет мәндеріндегі тәуелділіктері берілген. ГК-тардың жалпы жұмыс уақыты аясында олардың дербес қосылу уақытының ұзақтығы орбитадан шығару нәтижелеріне әсер етпейтіндігі көрсетілген.

Ашуров А.Е.

Увод космического аппарата с квазигеостационарной орбиты.

Приведены результаты моделирования процесса увода космического аппарата с квазигеостационарной орбиты после отработки им срока активного существования или после выхода из строя в результате нештатной ситуации. Рассчитаны необходимые импульсы, расход топлива при маневрах, требуемое время для поднятия орбиты на 300 км, изменения большой полуоси и эксцентриситета орбиты и дрейф спутника по долготе. Процесс поднятия орбиты рассматривается как результат последовательных включений газовых двигателей (ГД) и соответствующие изменения указанных параметров орбиты. Представлены зависимость дрейфа спутника и долготы при различных значениях эксцентриситета. Показано, что в пределах максимальной длительности включения ГД, продолжительность их отдельных включений существенно не влияют на конечные результаты увода с орбиты.

Купчишин А.И., Тілебаев Қ.Б.

Политетрафторэтиленнің рентгенқұрылымдық зерттеулері.

Политетрафторэтилен (ПТФЭ)-нің өзгерген түріне және спираль құрылыммен жасалған өндірістік (F-4) ультрадисперсті ұнтағына түрлі рентген қондырғылардың көмегімен әр түрлі шартты жағдайларда рентген құрылымдық зерттеулер жүргізілді. Алынған рентгенграммалардың бір-бірімен үйлеспейтіндігі байқалды. Мысалы, ультрадисперсті ұнтақтың рентгенграммасында екі рефлекс байқалса, ал ПТФЭ-нің өзгерген түрінде бір рефлекс байқалды. Сондай-ақ фторпласт-4-тің рентгенграммасында политетрафторэтиленге тән сызықтардан басқа дифракциялық қосымша пиктердің болуы фторпластының бірнеше фазасының бар болуын немесе оның құрылымдық өзгеріске ұшырағандығын көрсетеді. Алынған рентгенграммалардың зерттеулерден, $2\theta=18,15^\circ$ бұрышы кезінде бақылған ПТФЭ-нің стандартты сызығы барлық сынамаларға тән екенін көрсетті. Рентгенграммалардың өз арасындағы үйлеспеушілігі ПТФЭ сынамаларын алудың алғышарттармен байланысты деген қорытынды жасалды.

Купчишин А.И., Тілебаев Қ.Б.

Рентгеноструктурные исследования политетрафторэтилена.

Проведены рентгеноструктурные исследования ультрадисперсного порошка, упорядоченного со спиральной

структурой промышленного (F-4) и модифицированного политетрафторэтилена (ПТФЭ) на разных рентгеновских установках с разными условиями съемки. Полученные рентгенограммы заметно различаются между собой. В отличие от рентгенограмм ультрадисперсного порошка, у которого наблюдаются два рефлекса и модифицированного ПТФЭ с одним рефлексом, на рентгенограмме фторопласта-4 кроме линий политетрафторэтилена обнаружены дополнительные дифракционные пики (широкое диффузное гало и ряд отражений), которые свидетельствуют о присутствии нескольких фаз фторопласта или модификацией структуры. Анализ рентгенограмм показал, что стандартная линия ПТФЭ, наблюдаемая при угле ($2\theta = 18,15^\circ$) характерна для всех образцов. Установлено, что различие рентгенограмм обусловлены предисторией получения образцов ПТФЭ.

Жанабаев З.Ж., Гревцева Т.Ю., Икрамова С.Б., Филиппов Н.В.

КВАНТТЫҚ НАНОЖІПТЕРДІҢ ЭЛЕКТРЛІК ҚАСИЕТТЕРІ

Жұмыста жартылайөткізгішті наножіптердің электр өткізгіштігін сипаттайтын теңдеулер ұсынылған. Бұл теңдеулердің негізінде олардың вольт-амперлік сипаттамаларының ерекшеліктері, теріс дифференциалдық кедергіге ие аумақтың болуы, сонымен бірге қысықтардың осцилляциялану тәртібі сияқты ерекшеліктер түсіндірілген. Теңдеулерде нанокұрылымдардың масштабты-инварианттылығы, иерархиялық өзіне ұқсастық, фракталдық құрылымы ескерілген. Кванттық жіптер өзара байланысу кезінде фракталдық кластерлерді құратыны белгілі. Бұл құрылымдардың электрлік потенциалы бейсызықты фракталдық өлшемдер түрінде көрсетілген. Теориялық нәтижелер нанокластерлік жартылайөткізгіштердің электрлік қасиеттерін зерттеу бойынша арнайы тәжірибе нәтижелерімен дәлелденген.

Жанабаев З.Ж., Гревцева Т.Ю., Икрамова С.Б., Филиппов Н.В.

ЭЛЕКТРИЧЕСКИЕ СВОЙСТВА КВАНТОВЫХ НАНОНИТЕЙ

В работе представлены уравнения для описания электропроводности полупроводниковых нанонитей. На основе этих уравнений объяснены такие особенности их вольт-амперных характеристик, как наличие участков с отрицательным дифференциальным сопротивлением, а также осциллирующее поведение кривых. Уравнения учитывают масштабно-инвариантное, иерархически самоподобное, фрактальное строение наноструктур. Принято во внимание то, что квантовые нити при взаимодействии образуют фрактальные кластеры. Электрический потенциал этих структур представлен в виде нелинейных фрактальных мер. Теоретические результаты подтверждены результатами специальных экспериментов по исследованию электрических свойств нанокластерных полупроводников.

Агельменев М.Е., Братухин С.М., Поликарпов В.В.

Нанориббон графенінде орналасқан сұйық кристалдардың орналасу тәртіптілігіне әртүрлі ықпалдың әсері.

Компьютерге ынталандыру бойынша тәжірибелер графен бетінде орналасқан пара-хлор-фенолдың полярлы нематикалық фенилпропаргильді эфирлердің орналасуы заңдылықтар қатарын анықтауға мүмкіндік берді. Электр өрісі мен температура әсері кезіндегі молекулалардың динамикасы зерттелді. Зерттеу әдісі ретінде сұйық агрегаттық күй жуықтауындағы молекулалық динамика әдісі қолданылды. Модельдеу атомдық тәсілмен жүзеге асырылды. Нематикалық сұйық кристалдарға (НСК) графен түрінің азғантай әсері көрсетілген. НСК ағыстары мен өріс бағыттарының сәйкестік жағдайындағы НСК-ның үлкен тәртіптілігін атап өту қажет. Электр өрісінің кернеулігі артқан сайын кластердің орналасу тәртіптілігі сызықты түрде өсетіні анықталды. Сонымен бірге ең көп өсу жарықтану аймағында байқалады. Бұл изотропты сұйықтық саласындағы НСК-дың өздік ұйымдастыруына графен және электр өрісі басты рөл атқарады деп тұжырымдауға мүмкіндік береді.

Агельменев М.Е., Братухин С.М., Поликарпов В.В.

Влияние различных воздействий на упорядоченность жидких кристаллов, расположенных на графене нанориббоне

Эксперименты по компьютерному моделированию поведения полярных нематических фенилпропаргильных эфиров пара-хлор-фенолов, находящихся на поверхности графена, позволили выявить ряд закономерностей. Была исследована динамика молекул при воздействии электрического поля и температуры. В качестве метода исследования использован метод молекулярной динамики в приближении жидкого агрегатного состояния. Моделирование проводилось в атомистическом подходе. Показано небольшое влияние типа графена на поведение нематических жидких кристаллов (НЖК). При этом необходимо отметить большую упорядоченность НЖК в случае совпадений направлений поля и течения НЖК. Обнаружено, что с ростом напряженности электрического поля нелинейно растет упорядоченность кластера. Причем наибольший рост наблюдается в области просветления. Это позволяет утверждать о главенствующей роли графена и электрического поля на самоорганизацию НЖК в области изотропной жидкости.

Гученко С.А., Завацкая О.Н., Юров В.М., Касымов С.С., Лауринас В.Ч.

Металдардың беттік энергиясы және Толмен тұрақтысы.

Мақалада қатты денелердің беттік энергиясын анықтаудың белгілі әдістері бойынша шолу берілген. Сипатталған әдістердің әрқайсысы іс жүзінде температурамен немесе тәжірибе жүзінде төмен дәлдікпен анықталатын шамалармен шектеледі. Қатты дененің физикалық қасиеттерінің (магниттік өтімділік, люминесценция қарқындылығы, жылуөткізгіштік және т.б.) өлшемділік тәуелділігі негізіндегі беттік энергияны анықтаудың әдісі ұсынылды. Сілтілік металдардың галогендерінің беттік энергиясы анықталды. Оның шамасы таза металдардың беттік энергиясынан әлдеқайда артық. Осы қосылыстардың Холл-Петчтің тура эффектісі керегі өзгергенге дейінгі сындық радиусы есептелген.

Гученко С.А., Завацкая О.Н., Юров В.М., Касымов С.С., Лауринас В.Ч.

Поверхностная энергия и потостоянная Толмена металлов

В статье дан обзор существующих методов определения поверхностной энергии твердых тел. Каждый из описанных методов практически ограничен либо температурой, либо величинами, которые экспериментально определяются с малой точностью. Предлагается метод определения поверхностной энергии твердого тела на основе размерной зависимости его физического свойства (магнитной проницаемости, интенсивности люминесценции, теплопроводности и т.д.). Определена поверхностная энергия галогенидов щелочных металлов. Ее величина значительно больше, чем поверхностная энергия чистых металлов. Рассчитан критический радиус этих соединений, начиная с которого прямой эффект Холла-Петча меняется на обратный.

Камбарова Ж.Т., Саулебеков А.О.

Квадрупольді-цилиндрлік өрісте зарядталған бөлшектердің қозғалысын есептеу мен модельдеу.

Квадрупольді-цилиндрлік өрістен құрылған электрстатикалық энергия талдағышының электронды-оптикалық сұлбасы ұсынылған. Ұсынылған энергия талдағышының сыртқы электроды айнаның симметрия өсіне қатысты өте кіші көлбеу бұрышын құрайтын және 1,75 градусқа тең жасаушыға ие конус пішінге ие. Энергия талдағышының корпускулярлық-оптикалық параметрлерінің есептелуі жүргізілген. Жарық күші мен ажырату қабілеті тұрғысынан оптималды болатын зарядталған бөлшектердің бастапқы қозғалыс параметрлері келтірілген.

Камбарова Ж.Т., Саулебеков А.О.

Расчет и моделирование движения заряженных частиц в квадрупольно-цилиндрическом поле.

Предложена электронно-оптическая схема электростатического энергоанализатора с квадрупольно-цилиндрическим полем. Внешний электрод предложенного энергоанализатора имеет профиль конуса, образующая которого составляет малый угол наклона относительно оси симметрии зеркала, равный 1,75 град. Проведен расчет корпускулярно-оптических параметров энергоанализатора. Показаны преимущества данного поля. Приведены начальные параметры движения заряженных частиц, оптимальные с точки зрения светосилы и разрешающей способности.

Сериков Т.М., Ибраев Н.Х., Зейниденов А.К.

TiO₂/Ag нанокұрылымдарының фотокаталикалық қасиеттері

Электронды микроскопиялық зерттеулердің көмегімен «ядро-қабыршақ» нанобөлшектердің өлшемі мен пішіні анықталды. Ag / TiO₂ құрамының «ядро-қабыршақ» құрамымен, мұндағы ядро ретінде күміс нанобөлшегі алынды, ал қабыршағы титан диоксидінің нанобөлшектері болатын қабыршақтардың бар болған кезде метилен көгілдір бояғышының фототеградация процесі зерттеліп, фотокатализатордың фотокаталикалық қасиеттері анықталды. Зерттеу нәтижесінде Ag / TiO₂ құрылымды нанобөлшектердің бар болуы кезінде метилен көгілдір бояғыштарының фототеградация процесінің жылдамдығы артатыны анықталды.

Сериков Т.М., Ибраев Н.Х., Зейниденов А.К.

Фотокаталитические свойства наноструктур TiO₂/Ag

При помощи электронно-микроскопических исследований определены размер и форма наночастиц «ядро-оболочка». Исследован процесс фоторазложения красителя метилового голубого от времени облучения УФ – излучением без пленок из наночастиц диоксида титана и с их присутствием, а также со структурой «ядро-оболочка» состава Ag/TiO₂, где в качестве ядра служила наночастица серебра, а оболочкой наночастицы диоксида титана. Из полученных данных установлено, что действие фотокатализатора на основе Я-О Ag/TiO₂ значительно ускоряет процесс окисления красителя метилового голубого.

Астанов С.Х., Касимова Г.К.

Рибофлавиннің өздік жинастырылған молекулалардың электрондық спектрлер табиғаты

Ерітінділердің су мен бинарлы қоспалардағы рибофлавин молекулаларының өздік жинастырылу процесі спектроскопиялық әдіспен зерттелген. В2 дәрумен молекулаларының өздік жиналуы диполь-дипольдік және күшті индуктивті – индуктивті өзараәрекеттесулермен жүретіндігі көрсетілген. Осындай кешенді өзараәрекеттесулер нәтижесінде рибофлавин молекулаларының қозған электрондық деңгейлерінің резонанстық бөлшектенуі жүреді. Өздік агрегирленген молекулалар үшін сызықтық дихроизм спектрлерінде адсорбцияның жасырын жолақтары анықталған. Молекулалардың алынған спектрлері негізінде жұтылуға электрондық өтулердің сұлбалары құрылған.

Астанов С.Х., Касимова Г.К.

Природа электронных спектров самособранных молекул рибофлавина

Спектроскопическим методом исследован процесс самосборки молекул рибофлавина в водных и бинарных смесях растворителей. Показано, что самосборка молекул витамина В2 происходит диполь-дипольным и сильным индуктивно-индуктивным взаимодействием. В результате этого комплексного взаимодействия происходит резонансное расщепление возбужденных электронных уровней молекул рибофлавина. Для самоагрегированных молекул в спектрах линейного дихроизма определены скрытые полосы адсорбции. На основе полученных спектров молекул построены схемы электронных переходов к поглощению.

Амочаева Г.П., Сйсенбаева Г.С., Мусина Г.И.

Теміржол өткеліндегі тоқталған автотранспортты анықтау үшін видеоаналитикалық жүйені жобалау.

Жұмыста тоқталған автотранспортты анықтау мақсатымен теміржол өткелінде қолданылатын видеоаналитика үшін бағдарламалық қамтамасыз етумен және техникалық талаптарды өңдеудің сипаттамалары берілген. Жұмыста видеоаналитика жүйесінің, жұмыстық бақылау зоналарының сұлбалары сипатталған, видеоаналитика жүйесінің және оның құраушыларының графикалық иллюстрациялары келтірілген. Жұмыста сипатталған бағдарлама өткелдегі тоқтаған автотранспортты анықтап, локомотивті тоқтату үшін кедергі бағдарламға сигнал береді. Бағдалама кейбір кездері өңделмеген деректер беруді мүмкін. Бұл бағдарлама автотранспортты анықтайды, бірақ жалған іске қосулармен күрес қосымша техникалық құралдарды қолдануды талап етеді.

Амочаева Г.П., Сйсенбаева Г.С., Мусина Г.И.

Проектирование системы видеоаналитики для определения остановившегося автотранспорта на железнодорожном переезде.

В данной работе приводится описание разработки технических требования и программного обеспечения для видеоаналитики применяемой на железнодорожных переездах с целью определения остановившегося автотранспорта. В работе описаны описания схемы системы видеоаналитики, рабочих наблюдательных зон, приведены графические иллюстрации системы видеоаналитики и ее составляющих. Описываемая в работе программа определяет остановившейся автотранспорт на переезде и выдает сигнал на заградительные светофоры для остановки локомотива. Допускаются моменты, когда программа выдает недоработанные данные. Программа определяет автотранспорт, но борьба с ложными срабатываниями подразумевает использовать дополнительные технические средства.

Умирзаков А.Г., Мереке А.Л., Рақыметов Б.А., Бейсенов Р.Е., Муратов Д.А.

Қатты оксидті отын элементтерінде қолданыс үшін кеуекті никель анодын ыстық пресс және өңдеу әдістерімен алу.

Жұмыста жұқақабыршақты қатты оксидті отын элементтеріне арналған кеуекті никель анодын алудың қарапайым әдісі ұсынылған. Кеуекті никель анодын металл/кеуектүзгіштің ұнтақтарын әр түрлі қатынастарда араластыру әдісімен дайындалып, пресстеп және ары қарай термиялық өңдеулер нәтижесінде жасалынды. Кеуекті никель анодын никель және алюминий ұнтақтарын пресстеп алу процестері сипатталған. Алынған анодтың құрылымнан алюминийдің үлгілерін ерітуі мен өңделуі көрсетілген. Электролит қабаты импульсті лазерлік қондыру әдісімен алынады. Мақалада сканерлеуші электронды микроскоптың көмегімен алынған нәтижелері мен рентген спектроскопияның энергиялық дисперсияның талдауы көрсетілген.

Умирзаков А.Г., Мереке А.Л., Рақыметов Б.А., Бейсенов Р.Е., Муратов Д.А.

Получение пористого никелевого анода методами горячего прессования и травления для применения в твердооксидных топливных элементах.

Работа представляет собой способ получения пористого никелевого анода для тонкопленочных твердооксидных топливных элементов. Пористый никелевый анод изготавливается методом смешивания металл/порообразователь с различными соотношениями порошка, и с последующим прессованием и

термообработкой. Описан процесс получения пористого никелевого анода путем прессования никелевых и алюминиевых порошков. Показано дальнейшее спекание образцов и травление алюминия из полученной анодной структуры. Слой электролита получен импульсным лазерным осаждением. В статье приведены результаты, полученные с помощью сканирующего электронного микроскопа и анализа энергетической дисперсии рентгеновской спектроскопии.

Комилов О.С., Шарипов М.З., Тиллоев Л.И., Журабек А.М.

Күн жылыту жүйесінің автономды биогазды қондырғысы.

Күн жылыту негізінде тәжірибелі-өндірістік биогазды қондырғысы өңделіп, құрастырылған. Биогаздың және Күн энергиясының потенциалы болуы бойынша Өзбекістанның статистикалық мәліметтерінен биогаз қондырғысының параметрлерінің есептеу нәтижелері мен құрылымдық сұлбасы келтірілген. Қондырғының мезафильді жұмыс істеу режимі кезінде биогазды өндіруі бойынша эксперименттік зерттеулер нәтижелері келтірілген. Кіші тұтынушылық шаруашылықтар жағдайларында қайта жаңғырылатын көздері есебінен ашытылған биомассаның қызуымен биогаз қондырғыларды қолдану мүмкіндіктері қарастырылған.

Комилов О.С., Шарипов М.З., Тиллоев Л.И., Журабек А.М.

Автономная биогазовая установка с системой солнечного обогрева.

Разработана и построена опытно - производственная биогазовая установка на основе солнечного обогрева. Приведена её структурная схема и результаты расчетов параметров биогазовой установки исходя из статистических данных Узбекистана по наличию потенциала биогаза и солнечной энергии. Так, же приведены результаты экспериментальных исследований по выработке биогаза при мезофильном режиме работы установки. Рассмотрены возможности использования биогазовых установок с подогревом сбраживаемой биомассы за счет возобновляемых источников энергии в условиях малых потребительских хозяйств.

Исаханов М.Ж., Сақыпова Ш.Е., Әлібек Н., Дүйсенбаев Т.С.

Ауылшаруашылық құрылыстары үшін энергияны үнемдейтін желдету жүйесін өңдеп шығару.

Мақалада қой қораларының энергия үнемдейтін желдету жүйесінің өңдеу нәтижесі талқыланады. Қой қораларына арналған энергиялық тиімді эксперименттік желдету жүйесінің сұлбасы көрсетілген. Қойқорасының желдету жүйесі маңындағы топырақтың температуралық өріс сипаттау үшін жылуды тасымалдаудың дифференциалдық теңдеулері келтірілген. Берілген алғашқы және шекаралық шарттары кезіндегі өлшемсіз критерийлерінің есептеу мысалы келтірілген. Арнаның шығысында ауа температурасының мәндері және жылу ағынының мәні анықталды. Есептеулердің нәтижелері желдету жүйесінің жылу сипаттамаларын қашықтықтан тіркейтін ақпараттық-өлшеу жүйесі көмегімен алынған сынақ деректерімен сәйкес келеді.

Исаханов М.Ж., Сакипова Ш.Е., Алибек Н., Дюсенбаев Т.С.

Разработка энергоберегающей вентиляционной системы для сельскохозяйственных зданий.

В статье обсуждаются результаты разработки энергоэффективной системы вентиляции овечьих кошар. Показана схема экспериментальной энергоэффективной вентиляционной системы овечьей кошары. Приведены дифференциальные уравнения переноса тепла для описания температурного поля в почве около системы вентиляции овчарни. Приведен пример расчета безразмерных критериев при заданных начальных и граничных условиях. Определены значения температуры воздуха на выходе канала и значение теплового потока. Результаты расчетов согласуются с данными испытаний с использованием информационно-измерительной системы для дистанционной регистрации тепловых характеристик систем вентиляции.

Қазақбай Г.Б., Туралина Д.Е.

Түзу ағынды гидротурбинаның негізгі сипаттамаларын зерттеу.

Мақалада түзу ағынды гидротурбина қалақшаларының тиімді нұсқасын анықтау мақсатында жүргізілген зерттеу жұмыстарының нәтижелері келтірілген. Гидротурбинаның энергия тиімділігін жоғарылату қалақшаларының конфигурациясымен тікелей байланысты болып табылады. Зерттеу жұмысы сандық әдіспен COMSOL Multiphysics қолданбалы бағдарламалар пакетінде жүзеге асырылды. Су ағысының қозғалысын Навье-Стокс теңдеулері сипаттайды. Ағынның сандық зерттелуі Рейнольдс бойынша орташаланған Навье-Стокс (Reynolds Averaged Navier Stokes) әдісін қолдану арқылы жүзеге асырылады. Гидротурбина қалақшаларын итеруші су ағысының тиімді атқылау бұрышы анықталып, қалақшалардың тиімді орналасуы, қалақшалар арасымен ағып өтетін су жылдамдығының өзгерісі мен қысымдарының таралулары зерттелді. Қалақшаларға әсер ететін көтеруші және кедергі күштері, олардың коэффициенттері анықталды. Зерттеу нәтижелері негізінде жоғары энергия тиімділігіне ие гидротурбина қалақшаларының оптималды конфигурациялары анықталды.

Казакбай Г.Б., Туралина Д.Е.

Исследование основных характеристик прямоточной гидротурбины

В данной статье представлены результаты исследования, проведенного с целью определения эффективного варианта лопастей прямоточной гидротурбины. Повышение энергоэффективности гидротурбины напрямую связано с конфигурацией лопастей. Исследование выполняется в прикладной программе COMSOL Multiphysics с помощью численного метода. Уравнения Навье-Стокса описывают движение потока воды. Численное исследование потока осуществляется с использованием метода осреднения по Рейнольдсу уравнения Навье-Стокса (Reynolds Averaged Navier Stokes). Исследуются оптимальный угол атаки воды на лопасти гидротурбины, оптимальное расположение лопастей, изменение скорости и распределения давления воды через лопасти гидротурбины. Определяются подъемная сила и сила сопротивления, коэффициенты подъема и сопротивления, действующие на лопасти. На основании результатов исследования определяются оптимальные конфигурации лопастей гидротурбины с высокой энергоэффективностью.

Ибраев И.К., Ибраева О.Т., Сақытов К.Е.

Көмірлі флотациялық қалдықтардың жанбайтын агломерациясы.

Мақалада көмір-минералды брикеттің дамуы кезіндегі жоғары ылғалды көмірлі флотациялық қалдықтардың жанбайтын агломерациясы бойынша зерттеудің нәтижелері келтірілген. Технологияның мәні - жылу немесе салқындатқыштың сыртқы берілуінсіз және ылғалдандыру процесінің нәтижесі ретінде экзотермиялық реакция нәтижесінде сусыздандыру компонентті (араласқан әк - кальциленген әктің өндіріс қалдықты СаО кем дегенде 70%) есебінен шығарылатын жылу есебінен жүзеге асырылады. Химиялық құрғату үдерісі кезінде бөлінген жылудың салдарынан дайындалған көмір шырынының сапасы пайдаланылатын байланыстырғышты жылыту. Химиялық суспензия процестерін әктас материалдардан гидратациялаумен біріктіру, қоспаны орнықтыру процестерімен нығайту, металлургиялық өндіріс талаптарына жауап бермейтін агломерацияланбаған агломерациялық материалды алуға мүмкіндік береді. Процестің оңтайлы температурасы мен уақыт параметрлері және олардың жоғары беріктігіне жету кезінде көмірдің флотациялық қалдықтарының бастапқы ылғалдығы, пульверантталған әк, пропорциялық көмір флотациясының пропорционалды коэффициенті белгіленеді.

Ибраев И.К., Ибраева О.Т., Сакипов К.Е.

Безобжиговое окускование отходов флотации угля.

В статье приведены результаты исследования по безобжиговому окускованию высоковлажных отходов флотации угля с разработкой углеминерального брикета. Суть технологии заключается в том, что процесс удаления влаги проводят без внешнего подвода тепла или теплоносителя, а за счет тепла выделяемого при перемешивании с обезвоживающим компонентом (пылевидной извести - отход производства обожженной извести с СаО не менее 70 %) в результате протекания экзотермической реакции, а разогрев связующего, в качестве которого используют препарированную каменноугольную смолу за счет тепла, выделяемого при осуществлении процесса химического обезвоживания. Совмещение процессов химического обезвоживания гидратацией известь содержащими материалами, твердения смеси с процессами формования позволяют получать безобжиговый окускованный материал с прочностью, удовлетворяющей требованиям металлургического производства. Установлены оптимальные температурно-временные параметры процесса и долевые соотношения пылевидной извести, препарированной каменноугольной смолы и исходной влажности отходов флотации угля при достижении их высокой прочности.

**INFORMATION ABOUT
AUTHORS****АВТОРЛАР ТУРАЛЫ
МӘЛІМЕТТЕР****СВЕДЕНИЯ
ОБ АВТОРАХ**

Agelmenev, M.E. – Doctor of chem. sciences, Professor, Karaganda State University named after E.A. Buketov, Karaganda, Kazakhstan

Alibek, N.B. – PhD, Senior lecturer, Kazakh National Agrarian University, Almaty, Kazakhstan

Amochaeva, G.P. – Senior Lecturer, Department of Radiophysics and Electronics, Physical-Technical Faculty, Karaganda State University named after E.A. Buketov, Karaganda, Kazakhstan

Ashurov A. E. – PhD, Assistant professor, Space Technique and Technologies Department, L.N. Gumilyov Eurasian National University, Astana, Kazakhstan.

Astanov, S.X. – Doctor of phys.-math. sciences, Professor, Bukhara Engineering-Technologies Institute, Bukhara, Uzbekistan

Baktybekov, K.S. - Doctor of phys.-math.sciences, Professor, S. Seifullin Kazakh AgroTechnical University, Astana, Kazakhstan

Baktybekov, K.S. - Doctor of phys.-math.sciences, Professor, S.Seifullin Kazakh AgroTechnical University, Astana, Kazakhstan

Beisenov, R.E. - PhD, Associate professor, Head of EPR spectroscopy laboratory after Yu.V. Gorelkin, LLP "Institute of Physics and Technology", Head of the Department of Engineering Physics, Kazakh National Research Technical University named after K.I.Satpaev, Almaty, Kazakhstan

Bratukhin, S.M. – Candidate of chem. sciences, Head of the Department of Informatics and Chemical Technology, Central Kazakhstan Academy, Karaganda, Kazakhstan

Dyusenbaev, T.S. – Senior lecturer, Kazakh National Agrarian University, Almaty, Kazakhstan

Filippov, N.V. - PhD student, al-Farabi Kazakh National University, Almaty, Kazakhstan

Grevtseva, T.Yu. - Candidate of phys.-math.sciences, Assoc. Professor, al-Farabi Kazakh National University, IETP, Almaty, Kazakhstan

Guchenko, S.A. - Master of Physics, Junior Researcher, Karaganda State University named after E.A.Buketov, Karaganda, Kazakhstan

Ibraev, I.K. – Doctor of Technical Sciences, Professor, Department of the "Heat Power Engineering", L.N. Gumilyov Eurasian National University, Astana, Kazakhstan.

Ibraeva, O.T. - Candidate of Technical Sciences, Associate Professor, Department of the "Heat Power Engineering", L.N. Gumilyov Eurasian National University, Astana, Kazakhstan.

Ibrayev, N.Kh. - Doctor of phys.-math. sciences, Professor, Director of Institute of Molecular Nanophotonics, E.A. Buketov Karaganda State University, Karaganda, Kazakhstan

Ikramova, S.B. - Master of Technical Sciences, Lecturer, al-Farabi Kazakh National University, Almaty, Kazakhstan

Issakhanov M.Zh. – Doctor of phys.-math.sciences, Professor, Kazakh National Agrarian University, Almaty, Kazakhstan

Kambarova, Zh.T. – PhD, Docent, Physical-Technical faculty, Karaganda State University named after E.A. Buketov, Karaganda, Kazakhstan

Kasimova, G.K. – Researcher, Bukhara Engineering-Technologies Institute, Bukhara, Uzbekistan

Kasymov, S.S. - Candidate of phys.-math.sciences, Professor, Head of Scientific Research Center, Karaganda State University named after E.A.Buketov, Karaganda, Kazakhstan

Kazakbay, G.B. - Master student, Mechanics and Mathematics Faculty, al-Farabi Kazakh National University, Almaty, Kazakhstan

Komilov, O.S. - Candidate of Technical Sciences, Associate Professor, Bukhara Engineering-Technologies Institute, Bukhara, Uzbekistan

Kupchishin, A.I. - Doctor of phys.-math.sciences, Professor, Director of Physical-Technology center, Abay Kazakh National Pedagogical University, Almaty, Kazakhstan

Laurynas, V.Ch. - Candidate of phys.-math.sciences, Professor, Karaganda State University named after E.A.Buketov, Karaganda, Kazakhstan

Majidov, J.A. – Assistant, Bukhara Engineering-Technologies Institute, Bukhara, Uzbekistan

Mereke, A.L. - PhD student, Kazakh National Research Technical University named after K.I.Satpaev, Junior researcher of LLP "Institute of Physics and Technology", Amaty, Kazakhstan

Mirzhonova, N.N. – Assistant, Bukhara Engineering-Technologies Institute, Bukhara, Uzbekistan

Muratov, D.A. – Master, Junior researcher of LLP "Institute of Physics and Technology", Amaty, Kazakhstan

Musina, G.I. - Lecturer, Department of Radiophysics and Electronics, Physical-Technical Faculty, Karaganda State University named after E.A. Buketov, Karaganda, Kazakhstan

Polikarpov, V.V. - Master, Engineer, Head of the Department of Informatics and Chemical Technology, Central Kazakhstan Academy, Karaganda, Kazakhstan

Rakymetov, B. A. – Bachelor, Junior researcher of LLP "Institute of Physics and Technology";

Sakipov, K.E. - Candidate of Technical Sciences, Professor, Head of the «Heat Power Engineering» Department, L.N. Gumilyov Eurasian National University, Astana, Kazakhstan.

Sakipova Sh.E. - Candidate of phys.-math.sciences, Associate Professor, Kazakh National Agrarian University, Almaty, Kazakhstan

Saulebekov A.O. - Doctor of phys.-math. sciences, Professor, M.V. Lomonosov Moscow State University, Kazakhstan branch, Astana, Kazakhstan

Seisenbaeva, G.S. - Lecturer, Department of Radiophysics and Electronics, Physical-Technical Faculty, Karaganda State University named after E.A. Buketov, Karaganda, Kazakhstan

Serikov, T.M. – PhD, Senior lecturer, Department of Physics and Nanotechnology, Karaganda State University named after E.A. Buketov, Karaganda, Kazakhstan

Sharipov, M.Z. - Candidate of phys.-math.sciences, Docent, Bukhara Engineering-Technologies Institute, Bukhara, Uzbekistan

Tilloev, L.I. – Assistant, Bukhara Engineering-Technologies Institute, Bukhara, Uzbekistan

Tlebaev, K.B. - Doctor of phys.-math.sciences, Professor, Head of the Department, Abay Kazakh National Pedagogical University, Almaty, Kazakhstan

Turalina, D.E. - Candidate of phys.-math. sciences, Senior Lecturer, Faculty of Mechanics and Mathematics, al-Farabi Kazakh National University, Almaty, Kazakhstan

Umirzakov, A.G. - PhD student, Kazakh National Research Technical University named after K.I.Satpaev, Junior researcher of LLP "Institute of Physics and Technology", Amaty, Kazakhstan

Yurov, V.M. - Candidate of phys.-math.sciences, Professor, Head of Scientific Laboratoty, Karaganda State University named after E.A.Buketov, Karaganda, Kazakhstan

Zavatskaya, O.N. - Master of Physics, Junior Researcher, Karaganda State University named after E.A.Buketov, Karaganda, Kazakhstan

Zeinidenov, A.K. – PhD, Associate Professor, Head of the Department of Radiophysics and Electronics, Karaganda State University named after E.A. Buketov, Karaganda, Kazakhstan

Zhanabaev, Z.Zh. - Doctor of phys.-math. sciences, Professor, al-Farabi Kazakh National University, IETP, Almaty, Kazakhstan

Zhumaev, M.R. - Candidate of phys.-math.sciences, Professor, Bukhara Engineering-Technologies Institute, Bukhara, Uzbekistan

About «Eurasian Physical Technical Journal»

ISSN 1811-1165 Key title: Eurasian physical technical journal (Print)

Abbreviated key title: Eurasian phys. tech. j. (Print)

ISSN 2413-2179 Key title: Eurasian physical technical journal (Online)

Abbreviated key title: Eurasian phys. tech. j. (Online)

“Eurasian Physical Technical Journal” (Eurasian phys. tech. j.) is a peer-reviewed open access international scientific journal publishing original research results on actual problems of Physics, Technology and Engineering.

Since 2004 “Eurasian phys. tech. j.” is publishing in English. Periodicity is 2 issues per year.

The E.A. Buketov Karaganda State University is the main organizer and financial sponsor of EAPhTJ. The efforts of the international highly qualified Editorial Board consisting prominent physicists from 12 countries allow provide EAPhTJ international level.

Since 2004 more than 200 scientific papers written by physicists representing 23 countries were published. Among the authors there are full members and corresponding members of National Academies of Sciences of several countries and scientists with high H-index.

Since 2008 EAPhTJ has been included in the list of publications recommended by the Ministry of Science Education and Science of the Republic of Kazakhstan for the publication of the main results of the master's and PhD doctoral dissertations on the physical and mathematical sciences.

Publication Ethics and Malpractice Statement

Submission of an article to the Eurasian phys. tech. j. implies that the paper described has not been published previously, that it is not under consideration for publication elsewhere, that its publication is approved by all authors and tacitly or explicitly by the responsible authorities where the paper was carried out, and that, if accepted, it will not be published elsewhere in the same form, in English or in any other language, including electronically without the written consent of the copyright holder. In particular, translations into English of papers already published in another language are not accepted.

For information on Ethics in publishing and Ethical guidelines for journal publication see <http://www.elsevier.com/publishingethics> and <http://www.elsevier.com/journal-authors/ethics>.

The Eurasian phys. tech. j. follows the Code of Conduct of the Committee on Publication Ethics (COPE), and follows the COPE Flowcharts for Resolving Cases of Suspected Misconduct (http://publicationethics.org/files/u2/New_Code.pdf).

To verify originality, your article may be checked by the originality detection service Cross Check <http://www.elsevier.com/editors/plagdetect>.

Authors are responsible for the content of their publications. No other forms of scientific misconduct are allowed, such as plagiarism, falsification, fraudulent data, incorrect interpretation of other works, incorrect citations, etc. Authors are obliged to participate in peer review process and be ready to provide corrections, clarifications, retractions and apologies when needed. All authors of a paper should have significantly contributed to the research.

Reviewers should provide objective judgments and should point out relevant published works which are not yet cited. Reviewed articles should be treated confidentially. The reviewers will be chosen in such a way that there is no conflict of interests with respect to the research, the authors and/or the research funders.

Editors have complete responsibility and authority to reject or accept a paper, and they will only accept a paper when reasonably certain. They will preserve anonymity of reviewers and promote publication of corrections, clarifications, retractions and apologies when needed.

The acceptance of a paper automatically implies the copyright transfer to the Eurasian phys. tech. j. All submitted papers will be sent for reviewing to leading experts in the given area. The Editorial Board of the Eurasian phys. tech. j. will monitor and safeguard publishing ethics. The editors reserve the right to accept or reject manuscripts.

GUIDELINES FOR AUTHORS

Research articles, survey papers and short notes are accepted for exclusive publication in the «**Eurasian phys. tech. j.** » in English

The manuscripts and short notes must contain original results of investigation in the following scientific areas of Physics:

Non-linear Physics.

Modeling of the nonlinear physical - technical processes.

Energetics. Thermophysics. Hydrodynamics.

Material Sciences. Technologies for creating new materials.

Ecological Aspects of New Technologies.

Engineering. Devices and methods of experiment.

All publishing manuscripts and short notes must have been recommended by a member of the editor board or by the organization (University), where the work was performed. The author who submitted an article for publication will be considered as a corresponding author.

The paper, short note or review paper shall include an abstract of the contents, not exceeding 200 words and keywords (no more than 10). The abstract must not coincide with the introduction or conclusive part of the work and must not contain references, abbreviations and other unknown words.

All articles should have list of keywords or terms (3 to 10) for indexing purposes.

The text of a paper must not exceed 8-12 pages including tables, figures (no more than 6) and references. A short note must not exceed 4-5 pages including no more than 2 figures. A review paper must not be more than 20 pages (including no more than 10 figures).

The text should be divided on structural parts: **Introduction, Theoretical part, Experimental technique, Results and Discussion, Conclusion**, etc.

Printed copies shall be on good quality paper of International size A4. All texts must be printed in Microsoft Word. It is preferable to use the Times fonts. The text must be printed in 12 point letters, 1.5 intervals. There shall be a margin of 30 mm at the left-hand edge, of 15 mm at the fore edge, of 30 mm at the head of the page and of 30 mm at the tail. All pages must be numbered.

Acknowledgments may be shown at the end of the article text, before **REFERENCES**.

All references must be numbered in the text (for example, [1], [2-4]) and listed in numerical order.

Equations in your paper have to be written using the Microsoft Equation Editor or the MathType (<http://www.mathtype.com>) for (Insert | Object | Create New | Microsoft Equation or MathType Equation).

Tables must be inserted into the text.

Figures should be prepared in a digital form suitable for direct reproduction. Figures shall be submitted on the separate sheets and not included into the text.

The following files must be submitted via e-mail:

- Article text (*.doc);
- Figures (fig1.jpg, fig2.pcx);
- Figure captions (*.txt, *.doc).

